OPTICAL PHENOMENA IN OXIDE SEMICONDUCTORS

By

CHRISTOPHER PAUL PANSEGRAU

A dissertation submitted in partial fulfillment of
the requirements for the degree of

DOCTOR OF PHILOSOPHY

WASHINGTON STATE UNIVERSITY
Department of Physics and Astronomy

JUNE 2022

To the Faculty of Washington State University:

The members of the Committee appointed to examine the dissertation of CHRISTOPHER PAUL PANSEGRAU find it satisfactory and recommend that it be accepted.

Matthew D. McCluskey, Ph.D., Chair

Yi Gu, Ph.D.

Gary S. Collins, Ph.D.

ACKNOWLEDGEMENTS

Many people made it possible for me to complete this work, personally:

My friends and family, particularly my wife, dad, and mom.

The members of Augustana Lutheran Church in Moscow, ID. +VDMA+

Professionally,

The members, past and present, of the McCluskey lab, particularly Violet Poole and Jesse Huso, who taught me the laboratory skills I needed to complete this process.

The McCloy lab, particularly Jani Jesenovec, for growing the gallium oxide crystals used in major portions of this work.

Finally, Dr McCluskey, whose patience and instruction is appreciated more than I could ever adequately express.

Gallium oxide research was supported by the U.S. Department of Energy, Office of Basic Energy Sciences, Division of Materials Science and Engineering under Award DE-FG02-07ER46386.

Barium titanate research was supported by the National Science Foundation (NSF) under Grand No. DMR-2109334.

OPTICAL PHENOMENA IN OXIDE SEMICONDUCTORS

Abstract

By Christopher Paul Pansegrau, Ph.D.
Washington State University
June 2022

Chair: Matthew D. McCluskey

Acceptor doping of β-Ga_2O_3 has been driven by its potential as a semi-insulating material to serve as a substrate high-voltage/high-power devices. Strengthening this use-case is the ability to grow large, high-quality single crystals quickly and inexpensively. In this work, infrared and UV/Visible spectroscopy measurements were performed on β-Ga_2O_3 doped with zinc or copper. β-Ga_2O_3:Zn had significant hydrogen incorporation in the as-grown state, with a corresponding O-H mode in the infrared at 3486.7 cm^{-1}. This assignment was confirmed by annealing in deuterium and observing the corresponding O-D mode at 2582.9 cm^{-1}. A prominent peak at 5147.6 cm^{-1} has been attributed to an Ir^{4+} electronic transition and the sideband field implies the existence of tetrahedrally-coordinated zinc. Oxygen annealing increased the electrical resistance to more than 1 TΩ. β-Ga_2O_3:Cu exhibited room-temperature persistent photochromism upon exposure to sub-bandgap light. The photochromism was accompanied by the appearance of O-H modes in the infrared and a decrease in the Ir^{4+} peak intensity. It is proposed that light of sufficient energy releases the hydrogen from Cu_{Ga}-H_O complexes, which then forms the O-H bonds that were observed.

When annealed under a flowing gas atmosphere of hydrogen and humid argon, single crystals of $BaTiO_3$ exhibit persistent photoconductivity (PPC) at room temperature upon exposure to sub-bandgap light. The PPC is characterized by a broad infrared absorption peak at 5000 cm^{-1} and is accompanied by a factor of two decrease in electrical resistance. Larger gas flows were observed to correspond with larger infrared absorption. The photon energy threshold for PPC is similar to that observed in $SrTiO_3$ at 2.9 eV. Due to the similarities in behavior to PPC in $SrTiO_3$, an analogous model for the case of $BaTiO_3$ is proposed.

TABLE OF CONTENTS

Page

APPENDIX

LIST OF TABLES

LIST OF FIGURES

Dedication

To Christy.

CHAPTER ONE: INTRODUCTION

The wheel. Writing. Metallurgy. The steam engine. Electricity. Each of these inventions or discoveries should bring to mind a vivid picture of radical change thrust upon human life. This list is certainly not exhaustive, there are countless other, potentially even more notable inventions and discoveries that could be listed. There is one more that can be named, which motivates an entire subset of physics, in and of itself: the transistor.[1]

Semiconductor research had been occurring for more than a century prior to the invention of its arguably most earth-shattering application. Famous scientists like Seebeck, Faraday, and Hall laid the foundations for the work of others such as Schottky and Shockley.[2,3] While this work has a focus on characterization, rather than device making, this line of reasoning brings clarity to the motivation of any scientific work involving semiconductors. Research in the fundamental science of understanding material properties is a necessary prerequisite to practical application.

This work is structured thusly: Chapter 1 builds, at an introductory level, the mathematical tools of solid state physics and semiconductors and introduces a brief research and application history of the two focus materials, β-Ga_2O_3 and $BaTiO_3$. Chapter 2 discusses the instrumentation and experimental methods that were utilized. Chapter 3 is an overview of important crystal growth techniques, both bulk crystals and thin films. Chapter 4 will present the results of work performed on β-Ga_2O_3, which includes contributions to publications on gallium vacancy formation, the zinc acceptor, and persistent photochromism in β-Ga_2O_3:Cu. Finally, chapter 5 will present persistent photoconductivity in $BaTiO_3$.

1.1: Physics of the solid state and semiconductors

1.1.1: Plane-wave ansatz

The *plane-wave ansatz* is a mathematical tool that enables the approximation of the properties of solids and more specifically, semiconductors. 'Ansatz' is a German word that can be translated as 'approach'.[4] In order to determine the motion of atoms and behavior of electrons in a solid, the approach will be to assume solutions with the form $e^{i(kx-\omega t)}$ (plane waves). Two important problems, the diatomic linear chain and the electron in a periodic potential, form the basis of semiconductor physics and are underpinned by this solution method.

1.1.1.a: Phonons and dispersion curves

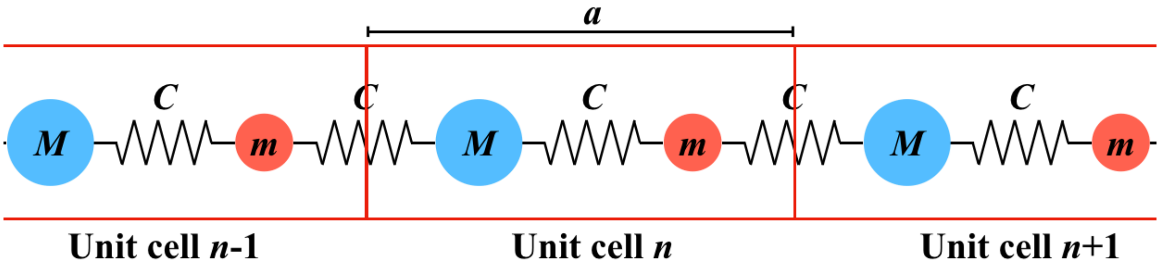

Figure 1.1. Linear diatomic chain. The unit cell is outlined in red and has length a. Masses M and m are labeled accordingly as well as springs with force constant C.

A common way to describe atomic motion in a crystal is through modeling a crystal as an array of masses (atoms) and springs (bonds). This method is so common it is frequently used as an early homework problem in solid-state physics classes. The simplest version of this problem assumes an infinite linear chain of atoms of alternating mass M and m connected by springs of spring constant C (figure 1.1). Traditionally the letter ‘k’ is used for spring constants in the core physics curriculum. However, this can be a source of confusion in the context of solid state physics where ‘k’ is commonly used to denote wavevectors or wavenumbers. Thus, the letter ‘c’ is used here to avoid the potential for this confusion and is differentiated from the speed of light by capitalization.

Simplifying assumptions for a common version of this problem are as follows:

1. Atomic interactions are modeled entirely by the mass-spring relationship
2. Atomic motion occurs only in the longitudinal direction
3. Atomic interactions are restricted to nearest neighbors only

While a monatomic linear chain may be an even simpler problem to solve, it will become apparent later that the monatomic solution can be extracted by setting $M = m$ with little additional effort.

The initial set-up requires describing the combination of forces on each of the two different masses. By displacing the mass M in unit cell n, an initial differential equation can be formed:

$$M\frac{d^2}{dt^2}x_{M,n} = -2Cx_{M,n} \tag{1.1}$$

However this is not the complete equation, as the displacements of M’s neighbor atoms also need to be considered. Adding these, and collecting all terms to the left hand side gives:

$$M\frac{d^2}{dt^2}x_{M,n} + C(2x_{M,n} - x_{m,n-1} - x_{m,n}) = 0 \tag{1.2}$$

Likewise, for atom m_n:

$$m\frac{d^2}{dt^2}x_{m,n} + C(2x_{m,n} - x_{M,n} - x_{M,n+1}) = 0 \tag{1.3}$$

As a result of the assumed plane-wave form, the initial assumption of infinite periodicity, and the behavior of time derivatives of exponential functions, the following substitutions are possible:

$$x_{m,n-1} = x_{m,n}e^{-ika} \tag{1.4}$$

$$x_{M,n+1} = x_{M,n}e^{+ika} \tag{1.5}$$

$$\frac{d^2}{dt^2}x = -\omega^2 x \tag{1.6}$$

Inserting these appropriately into 1.2 and 1.3, the result is a pair of equations that can be solved algebraically:

$$(2C - \omega^2 M)x_{M,n} - C(1 + e^{-ika})x_{m,n} = 0 \tag{1.7}$$

$$-C(1 + e^{ika})x_{M,n} + (2C - \omega^2 m)x_{M,n} = 0 \tag{1.8}$$

By creating a matrix from the coefficients in 1.7 and 1.8, setting the determinant equal to zero, and applying the quadratic equation to solve for ω^2, the final result is:

$$\omega^2 = C(\frac{1}{M} + \frac{1}{m}) \pm C\sqrt{(\frac{1}{M} + \frac{1}{m})^2 - \frac{2}{Mm}(1 - \cos(ka))} \tag{1.9}$$

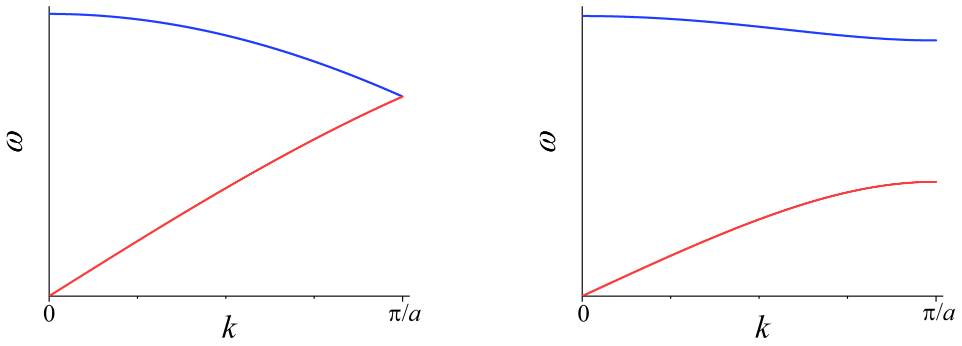

Figure 1.2. Plots of 1.9 for $M = m$ (left) and $M = 5m$ (right). The optical branches are blue and the acoustic branches red. Notice for $M = m$ that the branches meet at $k = \pi/a$. As M increases with respect to m, the optical branch flattens and the acoustic branch begins to bend.

Equation 1.9 is a *dispersion relation*, and the result of plotting ω versus k is shown in figure 1.2. Two cases are presented; $M = m$ (the monatomic linear chain) and $M = 5m$. The upper and lower branches are the result of the addition or subtraction in 1.9, respectively. The two branches are physically significant, and not just a mathematical artifact. The lower branch (red in figure 1.2) is referred to as the *acoustic branch*, and is predictably sound-like in behavior. The upper branch is referred to as the *optical branch* (blue in figure 1.2), and is correspondingly light-like in behavior. In more specific terms, the acoustic branch is so named because it corresponds to the propagation of sound waves in a crystal. Likewise the optical branch, under the right conditions, strongly absorbs light energy. This is particularly true in ionic compounds, where the modes associated with the optical branch create changing dipole moments between the atoms in the crystal. A more comprehensive discussion of these phenomena is available in chapter four of Ibach and Lüth.[5]

All this information comes from a relatively simple problem with strongly limiting assumptions. The solution was straightforward to derive; however, this implies more sophisticated models can be constructed by altering the problem's base assumptions and allowing for the following:

1. Transverse atomic oscillation
2. Alternating coupling constants
3. Atomic occupation of sites in the second and/or third spatial dimensions
4. Consideration of atomic interaction beyond nearest neighbors

As the problem gets more complex it may become necessary to utilize numerical methods to find the solutions. As a matter of fact, significant work in computational physics is devoted to the study of molecular dynamics problems.[6,7]

With the main result derived and possible improvements to the model presented, one keyword remains to be introduced: *phonons*. It is a curious habit in solid-state physics to treat the lattice vibrations that have been examined here as particles. Treating things that are very obviously waves as particles doesn't seem right at first, but it's not so different conceptually from photons. Particles of light, after all, may seem equally ridiculous. However, in the same way a photon is useful in describing a light wave that carries energy through space, a phonon carries momentum (and a small amount of energy) through a crystal.

1.1.1.b: Electrons and band structure

With atomic motion quantified, it is time to discuss how electrons behave in a solid. The derivation is similar, since plane-waves will again be the assumed solution. Rather than a classical approximation, electrons require a quantum mechanical approach.

The simplest version of this problem treats the coulombic potentials around atomic nuclei as a square well with infinitely tall walls. This problem should be very familiar to students who have completed a wave mechanics unit in a quantum mechanics class. The starting point is the time-independent Schrödinger equation with $V = 0$ (i.e., in the region where ψ is nonzero):

$$\frac{-\hbar^2}{2m}\frac{\partial^2}{\partial x^2}\psi = E\psi \tag{1.10}$$

A plane-wave solution is assumed with the time-dependence from earlier omitted:

$$\psi = e^{\pm ikx} \tag{1.11}$$

Taking the derivative twice and dividing the residual ψ out of the equation gives a well-known result:

$$E = \frac{\hbar^2 k^2}{2m} \tag{1.12}$$

For the environment an isolated potential well creates, the E versus k relationship is a simple parabola. In order to reach a quantitative solution, perturbation theory must be applied. This requires altering the potential used from a single square well to a periodic series of wells with potentials that dip strongly negative in the vicinity of the atomic nuclei. An appropriately motivated rigorous solution is presented in chapter seven of Ibach and Lüth.[5] The commonly applied qualitative argument is summarized as follows:

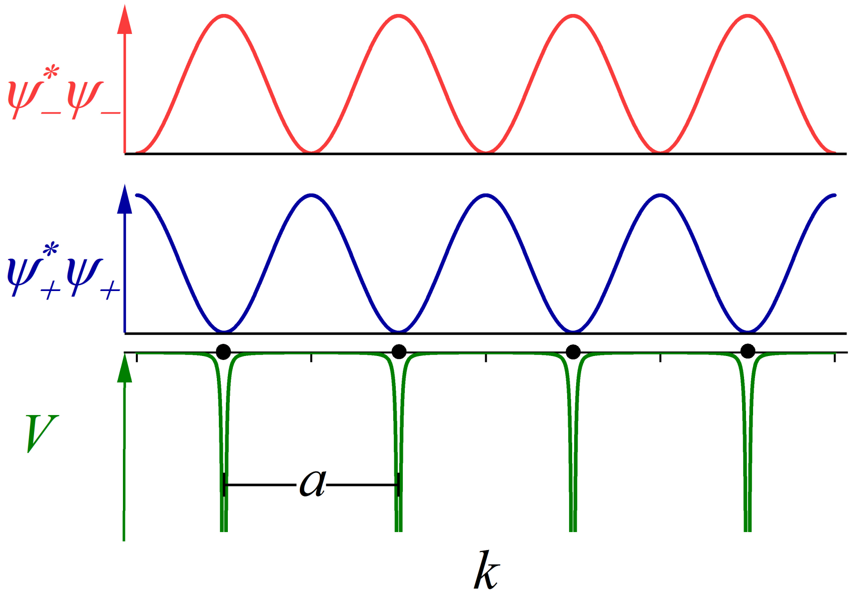

Figure 1.3. Probability densities of the bonding (middle, blue) and antibonding (top, red) wavefunctions. The potential due to the atomic centers (black dots) are periodic with separation *a*.

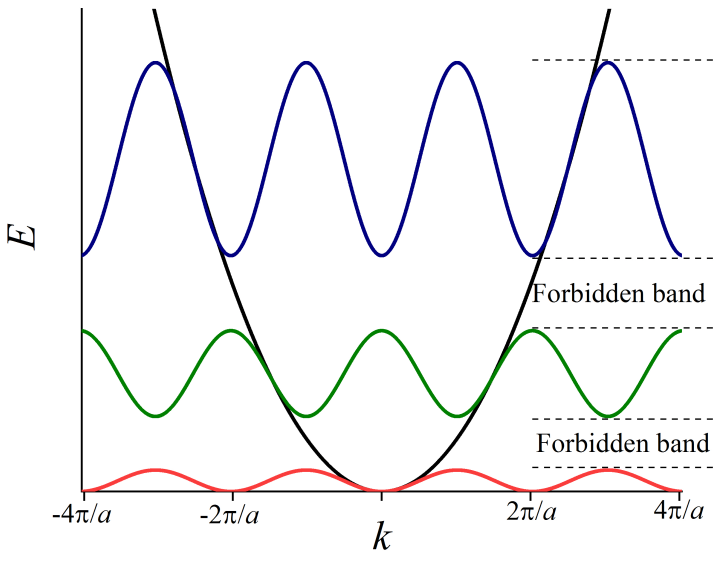

Figure 1.4. Energy bands created by a one-dimensional periodic lattice (red, green, blue), superimposed on the free-electron energy parabola (black). Certain energy regions, labeled as forbidden bands, no longer contain states for electrons to occupy.

Using the assumed solution form (1.11), two equal-energy wavefunctions can be defined:

$$\psi_+ = e^{ikx} + e^{-ikx} \tag{1.13}$$

$$\psi_- = e^{ikx} - e^{-ikx} \tag{1.14}$$

Calculating the probability densities of each of these wavefunctions shows that electrons described by one wavefunction are more likely to be located near the nuclei (ψ_-, referred to as antibonding), and electrons described by the other are more likely to be located between the nuclei (ψ_+, referred to as bonding) as shown in figure 1.3. By virtue of the large coulombic potential well at the site of the nuclei, the electrons described by an antibonding wavefunction have energies lower than the predicted parabolic value given in equation 1.12. The opposite is true of bonding wavefunction electrons, as they will have energies slightly larger than the predicted parabolic value. The result is at points where the parabolae would intersect, they instead bend and create levels with definite gaps between. These forbidden bands are called *bandgaps* (figure 1.4), energy regions where there exist no states for an electron to occupy. They are a semiconductor's defining feature, from where semiconductors derive their useful and interesting properties. These will be discussed in the following sections.

Since the solutions were assumed to be plane-waves, this derivation is called the *nearly-free electron approximation*. As with the derivation of phonon behavior in the previous section, the approximation can be made incrementally better by using more accurate models. A commonly discussed improvement over the nearly-free electron approximation is the *tight-binding approximation*, which accounts for the fact that core-level electrons are decidedly **not** free. From there, interactions between multiple charge carriers can be considered and improvements made to the location and shape of potentials used in the calculations. Again, sophisticated efforts in this area require numerical techniques, and are the subject of efforts among computational physics research groups.[6,8–10]

1.1.2: Defects and dopants

While the properties of pure semiconductors are intrinsic, they can be adjusted quite finely by careful introduction of defects and dopants. Base-level theory and calculations like to assume an ideal crystal, but no real material is ever so perfect. Thermodynamics demands every real system must fall victim to entropy in some way:

the manifestation may be a missing atom here, an extra one there, or even the occasional foreign atom. The term *defect* encompasses any and all errors in the crystal structure, and it is critical that their impact on the properties of the rest of the crystal structure be measured, quantified, and understood. Defects are classified as *native* when only atoms named in the chemical formula of the host crystal are involved in the defect or *extrinsic* when a foreign atom is involved. *Point defects* have a dimensionality of approximately one atom and do not interrupt the long-range order of the lattice.

To the chagrin of chemists the world over, the introduction of certain defects is oftentimes deliberate. When one particular type of atom is purposefully replaced with a different type of atom, the replacement atom is called a *dopant*. This process is not so different in principle or objective from adding carbon to iron to make steel or combining tin and lead to make solder. In the cases where it is done, some favorable change in the material properties occurs and the material emerges more useful as a result. The difference comes as a matter of degree. Solder is usually some alloy combination on the order of 60 wt% tin and 40 wt% lead. Steel contains at most ~2 wt% carbon, and anything more is reclassified as cast iron or iron carbide. As a general rule, 0.25 at.% is considered heavily doped in semiconductors and anything in excess of 1% is referred to as an alloy.

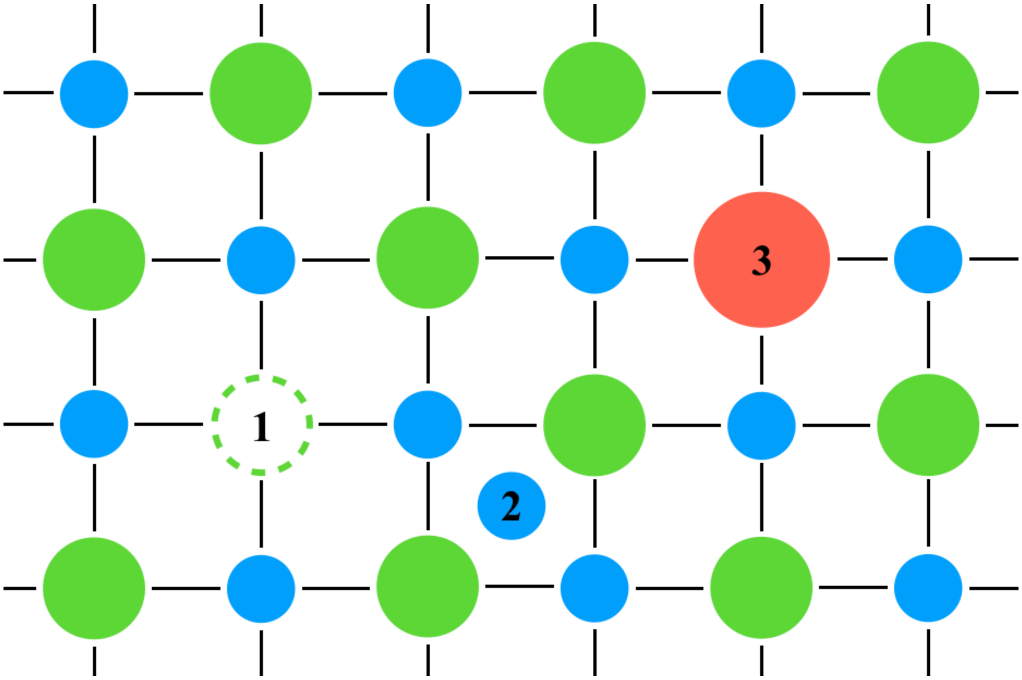

Figure 1.5. A 2D crystal structure abstraction which contains examples of (1) a vacancy, (2) an interstitial, and (3) a substitution.

Three types of defect are particularly useful to note for this work; the *vacancy*, *interstitial*, and *substitution* (figure 1.5). Vacancies are simply atoms missing from the crystal structure and are denoted as V_x, where x is replaced with the chemical symbol for the missing species. Interstitial atoms, denoted as X_i, exist in the space between defined lattice positions, and as a result tend to be small atoms like hydrogen. Substitutions are replacements of one atom with another and are denoted as X_Z, where X is the defect atom that is occupying a site that would rightly contain a Z atom. The effects defects have on the properties of the host material will be discussed in the following sections.

1.1.3: Vibrational and optical properties

Special modes arise when a markedly lighter or heavier atom is introduced as a defect in the diatomic linear chain calculation from section 1.1.1.a. The calculation is best performed numerically, but interesting results arise. In the case of a light defect atom, high-frequency (above the optical branch) high-amplitude oscillations called *local vibrational modes* (LVM) are the result. These modes are local because the light defect atom doesn't transmit its momentum past its heavier neighbors very well, so disruption to the modes of the rest of the lattice is minimal. In the case of a heavy defect atom, the result is a *gap mode*. Like LVMs, the amplitude of oscillation is large. Unlike LVMs the frequency is low (typically occurring between the acoustic and optical branches) and the mode is not as localized. The heavy atom projects its motion across the lattice to a greater degree on account of its greater momentum.

Before proceeding further, it is useful to identify a quantity that is commonly used in vibrational spectroscopies. *Wavenumbers* are defined as:

$$\frac{1}{\lambda} = \frac{\omega}{2\pi c} \tag{1.15}$$

Traditionally, the units of wavenumbers are cm^{-1}, where *c* is the speed of light and the rest are the usual suspects according to convention. From the form of equation 1.15, it is easy to see that wavenumbers are analogous to frequency.

The principal measurement technique utilized for this work is infrared spectroscopy. The technique will be discussed in detail in a later chapter, but some brief comments are in order here. Infrared measurement techniques are ideal for studying vibrational phenomena due to the fact that infrared light, heat energy, and vibrational energy are all closely related. Infrared photons are capable of exciting lattice vibrations as discussed at the end of section 1.1.1.a. This is quantified in the Beer-Lambert law, which defines *absorption* through a sample:

$$I = I_0 e^{-\alpha x} \tag{1.16}$$

where the absorption coefficient α has units of cm^{-1}. I_0 is the incident intensity, I is the transmitted intensity, and x is sample thickness. Vibrational modes that absorb infrared light will appear on an infrared spectrum as an intensity dip (despite facing downward, it is often called a peak). The strength of the absorption is related to number of opportunities the photons have to be absorbed. This can be achieved with large or defect-dense samples.

Related to absorption, *absorbance* is a calculated quantity:

$$Absorbance = \log_{10} \frac{I_0}{I} \tag{1.17}$$

I_0 denotes the reference spectrum, which is often a blank. Absorbance has many useful behaviors that stem from the properties of logarithms. These will be presented in appendix C. A peak in absorbance can be integrated and its area correlated to the number of absorbing defects according to:

$$IntegratedAbsorbance = \frac{A \bullet d}{\ln(10)} N \tag{1.18}$$

where A is an experimentally determined calibration factor, d is the sample thickness, and N is the number density of the defects (cm^{-3}).

1.1.4: Electronic properties

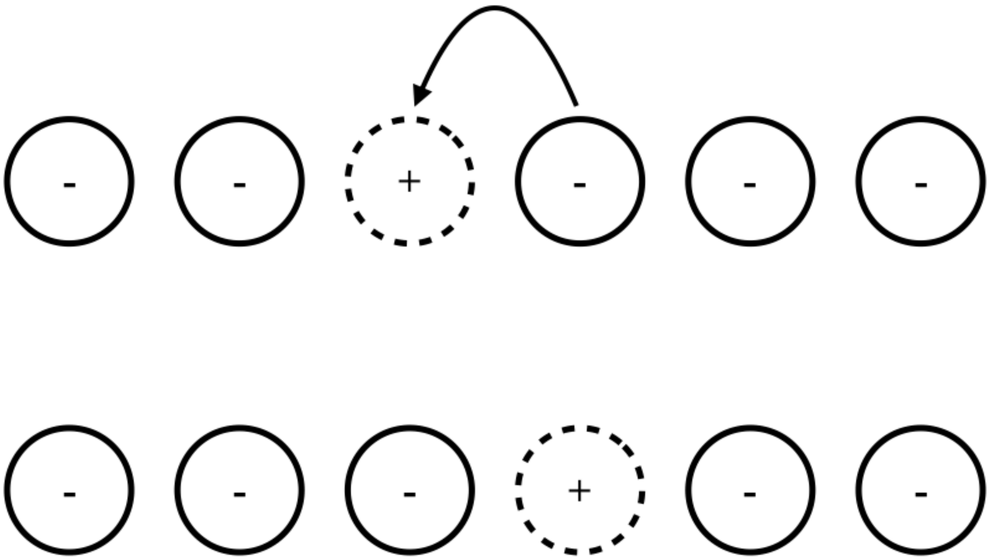

Figure 1.6. Demonstration of hole behavior. The motion of an electron in one direction can also be described as the motion of the hole in the other.

The absence of an electron can be treated as a positively charged particle called a *hole*. Electrons and holes together are referred to as *charge carriers*, since their motion transports charge from one place to another. Charge transport is described at the introductory level by the Drude model, and is discussed thoroughly in textbooks such as Yu and Cardona, Ibach and Lüth, and McCluskey and Haller.[5,11,12]

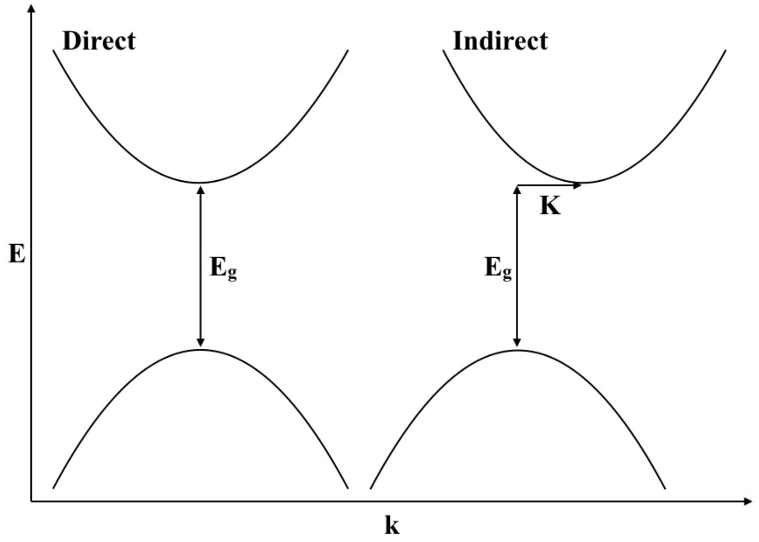

Figure 1.7. Direct (left) and indirect (right) bandgaps. Band-to-band transitions in an indirect bandgap either require energy in excess of E_g or interactions with additional momentum-carrying particles (phonons).

The idealized bandgap derivation generates *direct* bandgaps where the *valence band maximum* and *conduction band minimum* are superimposed at the same location in k-space (figure 1.7). This is not true for all materials. Some of the most common semiconductors, such as silicon and germanium, have *indirect* bandgaps where the VBM and CBM have a lateral (k-space) separation. Additionally, the nearly-free electron approximation generates a series of many bands with increasing energy. While this may be physically true, it is not practical. As shown in figure 1.8, the region considered is usually restricted to the region near the Fermi energy that contains the upper bound of the *valence band* and the lower bound of the *conduction band*. Charge carriers in the valence band occupy valence states of their host atoms and are relatively bound in space. Charge carriers that have been promoted to the conduction band have enough energy to be free of their host atom and conduct electricity as a result.

Electrons occupy states within the allowed bands starting with the lowest energy states (innermost orbitals) according to the Fermi-Dirac distribution:

$$f(E) = \frac{1}{e^{(E-E_F)/k_B T} + 1} \tag{1.19}$$

At $T = 0$, all states up to the Fermi energy (E_F) are filled, but none above. E_F usually lies somewhere within the band gap, relegating electrons to states available in the valence band. As T grows, the number of electrons permitted above E_f increases. At sufficient temperature, some electrons gain enough thermal energy (in excess of the gap energy E_g) to leave their host atoms and promote to the conduction band and move freely. This is why, directly opposing the behavior of metals, semiconductors demonstrate decreased electrical resistance with increasing temperature (metals increase resistance on account of thermal scattering processes). The energy for promotion to the conduction band doesn't have to be solely thermal, however. Photons are capable of promoting electrons to the conduction band as well.

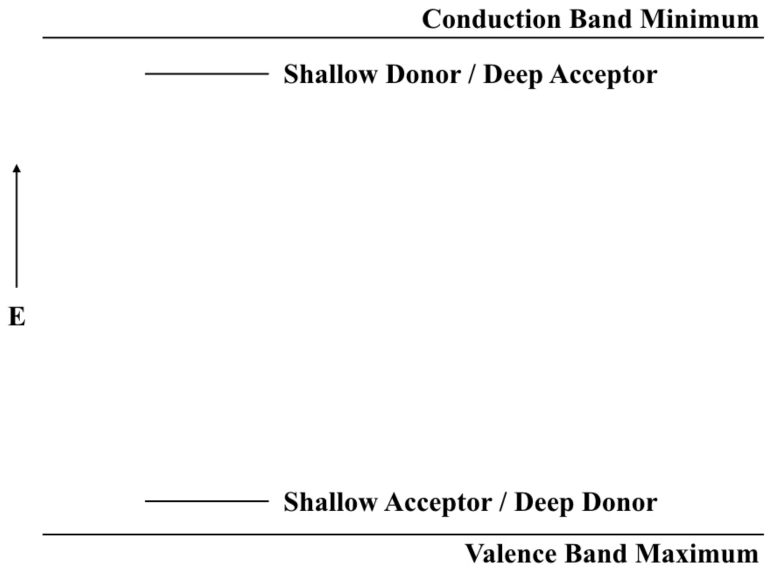

Figure 1.8. Simplified band diagram. The distance from the valence band maximum to the conduction band minimum is the bandgap. Relative locations of shallow/deep donor/acceptor levels within the bandgap are shown. The areas above and below the conduction band minimum and valence band maximum, respectively, can be treated as continua.

In an ideal semiconductor, the bandgap is devoid of states. Semiconductors that have been doped are no longer ideal. Dopants that have the same valence number as the atoms they replace are *isoelectronic*. They don't introduce states into the bandgap but will alter vibrational properties by way of differing masses, as discussed in the previous section. Defects that are electron deficient with respect to the replaced atom (lower valence number) are called *acceptors*, since an atomic bond is now missing an electron. This hole can now be filled by an electron from somewhere else in the crystal with sufficient energy. Thus a new state appears inside the band gap (figure 1.8). Defects that have a surplus of electrons (larger valence number) with respect to the correct arrangement are called *donors*, since they introduce extra electrons to the crystal. Donor and acceptor states are called deep or shallow based on their distance from either the valence band maximum or conduction band minimum. Donors measure distance to the conduction band and acceptors measure distance to the valence band. Small distances are *shallow* and large distances are *deep*.

In the case that both donors and acceptors are present in one material, the donor electrons will occupy acceptor holes until one or the other is depleted. This process is called *compensation*. In the event the net result is a surplus of holes (electrons), the material is called *p-type* (*n-type*), where *p* and *n* stand for positive and negative and correspond to the charge on the carrier. Hydrogen is a unique (and often inadvertent) dopant that can act as either donor or acceptor, since it is able to accept an electron to fill its valence states or donate its sole electron to empty them. *Passivation* occurs when hydrogen compensates a defect by forming a complex with that defect.

1.1.5: Further reading

This has been only a brief overview of solid-state and semiconductor physics. More rigorous and comprehensive treatments can be found in the following recommended texts:

* *Solid-state physics* by Ibach and Lüth.[5] This general-purpose graduate-level solid state text does not neglect the experimental aspects of science. It is an excellent resource for questions such as “how does that measurement technique work?” and “how is that quantity measured?”.

* *Dopants and defects in semiconductors* by McCluskey and Haller.[12] An excellent comprehensive overview of semiconductor science that describes everything from fundamental theory to growth techniques without getting bogged down in any one place for too long. The citations at the end of each chapter cover additional material.

1.2: Gallium oxide

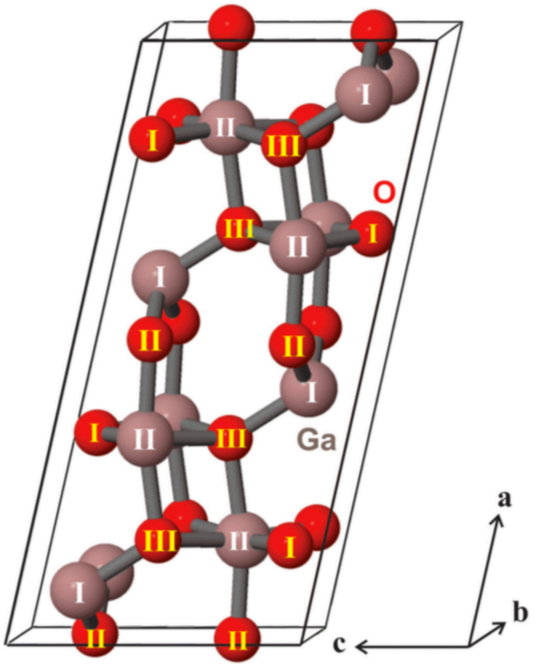

Figure 1.9. Chemical structure of β-Ga_2O_3. Image from McCluskey.[13] Gallium (brown) has tetrahedral (labeled I) and octahedral (labeled II) sites that are 4- and 6-coordinated with oxygen, respectively. Oxygen (red) has three sites labeled as I-III.

Gallium oxide is a transparent oxide semiconductor with an ultrawide bandgap of 4.5 - 4.8 eV.[13] It has five polymorphs, but only the monoclinic β phase, shown in figure 1.9, is stable at ambient conditions.[14] Growth of thin film and bulk material can be performed by a variety of techniques. Successful thin film methods include sputtering, metal-organic chemical vapor deposition, and molecular beam epitaxy.[15–18] Popular bulk growth methods include Czochralski (CZ), edge-defined film-fed, and floating zone.[19–22] Growth techniques will be discussed in detail in chapter 3. The bulk single crystal β-Ga_2O_3 samples used in this work were grown by the McCloy group at WSU using the Czochralski technique.[23]

β-Ga_2O_3 has a variety of intriguing properties. To start, the bandgap is polarization-dependent. The lower bound of 4.5 eV corresponds to polarization along the **c** axis and the upper bound of 4.8 eV to polarization along the **b** axis.[13] Electron mobilities of up to 200 cm^2/V s have been observed and as a result of this and its large bandgap, it has an impressive breakdown field (~8 MV/cm).[13,20,22,24] Unfortunately, doping the material to achieve p-type conductivity is not a trivial problem due to self-trapped holes or hole polaron formation.[25–27]

This combination of properties lends itself well to several applications. Acceptor doping (such as Fe, Mg, or Zn) yields semi-insulating material that can be used as substrate material.[28–31] Zirconium and hafnium doping have been shown to yield a very conducting material.[32,33] Device possibilities include transparent conductive films, thin-film transistors, and photodetectors.[34] Due to the large electron mobilities and breakdown field, high-energy applications have been also been gaining attention.[28]

In this work, the effect of doping with zinc and copper acceptors was analyzed. Zinc was found to yield similar behavior to previous work done with magnesium, and its interaction with hydrogen and iridium was characterized.[30] Doping with copper was found to induce persistent photochromism. Experimental details will be presented in chapter 4.

1.3: Barium titanate

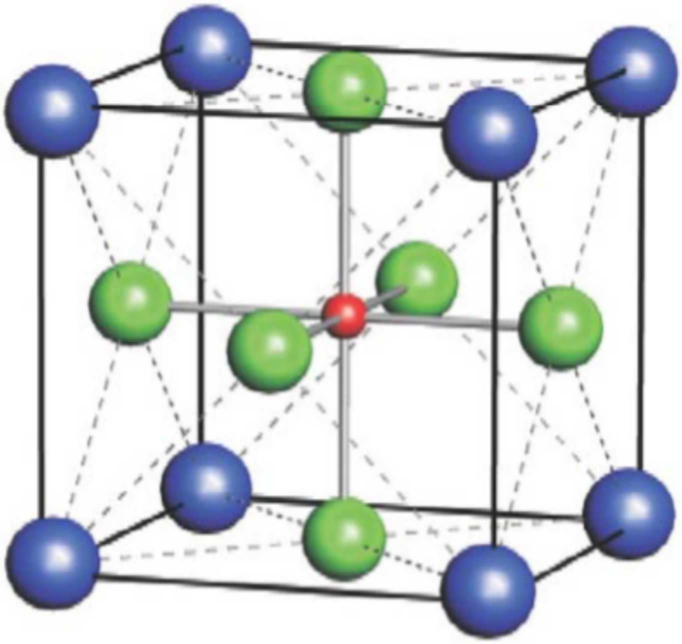

Figure 1.10. Chemical structure of barium titanate. Image from Vijatović *et al*.[35] Barium atoms occupy the corners (blue), titanium the center (red), and oxygen the faces (green).

Barium titanate ($BaTiO_3$, BTO) is a transparent perovskite oxide (figure 1.10) which has a band gap of 3.22 eV.[35,36] BTO has multiple phase transitions across a wide temperature range. From high to low temperature, the crystal structure of BTO can be hexagonal, cubic, tetragonal, orthorhombic, and finally rhombohedral. The transition temperatures between these phases are 1460, 120, 5, and -90ºC, respectively.[35] A variety of synthesis methods have been innovated for powder material, an overview of which is presented in Vijatović *et al*[35] and high-quality single crystals can be grown using Czochralski-like techniques[37].

Barium titanate has three notable scientific applications. First and foremost, it is ferroelectric and piezoelectric, properties that arise from displacement of the central titanium atom along the *c*-axis.[35] Naturally, BTO has seen use in applications that make use of these properties, such as transducers. Above the Curie temperature of 120ºC, the crystal structure is cubic and the titanium atom is stable in the "correct" position at the center of the unit cell and will not maintain a spontaneous polarization as a result. Second, BTO has a dielectric constant in excess of 1500, giving it applications in capacitors.[38] Third, BTO is photorefractive, giving it a range of applications in nonlinear optics.[39] This combination of properties gives a rich array of potential physics and device possibilities for study.

In order to properly motivate the experiments performed with BTO, an analogous material must be mentioned: strontium titanate. Strontium titanate ($SrTiO_3$, STO) shares the perovskite structure with BTO, but trades the barium atom for strontium. The bandgap of STO is slightly larger than that of BTO at 3.25 eV.[40] STO has applications in optics, as a photocatalyst, and has a wide range of electrical properties.[41,42] Interestingly, STO is not ferroelectric.[43] The relevant property for this work is STO's room-temperature, large, persistent photoconductivity, and that is what will be explored in BTO. Due to the chemical and structural commonalities between the two materials, BTO is an excellent candidate for persistent photoconductivity.

Persistent photoconductivity (PPC) is characterized by a long-lived reduction in resistivity that is induced by exposure to light.[44] PPC in strontium titanate was discovered by Tarun *et al.*[40] in 2013 and is notable for its existence at room temperature, magnitude of change (up to several orders of magnitude), and long lifetime (the effect was empirically fitted to a sum of exponentials with time constants of 17 days and 800 years)[45]. The effect is induced by sub-bandgap light (2.9 eV). Warming (~400ºC) can erase some changes caused by light exposure. Initial samples were prepared by sealing bulk STO crystal and SrO powder in an evacuated silica ampoule and annealed at 1200ºC for 1 hr.[40] It was later shown that the SrO powder used in the previous experiments was contaminated with $Sr(OH)_2$, which led to a series of experiments involving various annealing conditions. It was determined that oxygen and hydrogen, both elemental and as water, were the critical components to inducing PPC in STO.[45] Based the findings of the various annealing processes, Poole *et al*[45] proposed the following processes to describe the PPC:

Hydrogen excess preparation:

$$\mathrm{H}_{\mathrm{O}}^{+} + (V_{\mathrm{Sr}} - \mathrm{H})^{-} \rightarrow V_{\mathrm{O}}^{2+} + (V_{\mathrm{Sr}} - 2\mathrm{H})^{0} + 2e^{-} \tag{1.20}$$

Hydrogen deficient preparation:

$$\frac{1}{2}V_{\mathrm{O}}^{2+} + \mathrm{H}_{\mathrm{O}}^{+} + V_{\mathrm{Sr}}^{2-} \rightarrow \frac{3}{2}V_{\mathrm{O}}^{2+} + (V_{\mathrm{Sr}} - \mathrm{H})^{-} + 2e^{-} \tag{1.21}$$

In both cases, a hydrogen atom occupying an oxygen vacancy moves to an interstitial site next to a strontium vacancy, promoting an electron to the conduction band in the process. Though this model was proposed specifically for STO, it could apply to oxides in general. By preparing BTO in a flowing atmosphere of humid argon and hydrogen, it was the objective of this work to demonstrate that PPC is not unique to STO. Experimental details will be discussed in chapter 5.

CHAPTER TWO: EXPERIMENTAL TECHNIQUES

2.1: FTIR spectroscopy

Infrared light can be used to probe atomic vibrations in a crystal. As discussed in sections 1.1.1a and 1.1.3, certain atomic vibrations can be excited by the absorption of light energy. The amount of energy involved in these vibrations corresponds to that present in infrared photons, below ~1.6 eV. In order to study the infrared absorption of crystals, a spectrometer that uses infrared light is used.

Traditional spectrometers pass light from an appropriate source through a wavelength selector to scan each wavelength in the desired spectral range one at a time. The intensity is recorded as a function of wavelength directly. This type of technique is used in UV/Visible spectroscopy as well as some infrared spectrometers. With regard to infrared spectroscopy, a technique that utilizes the Fourier transform has been developed.

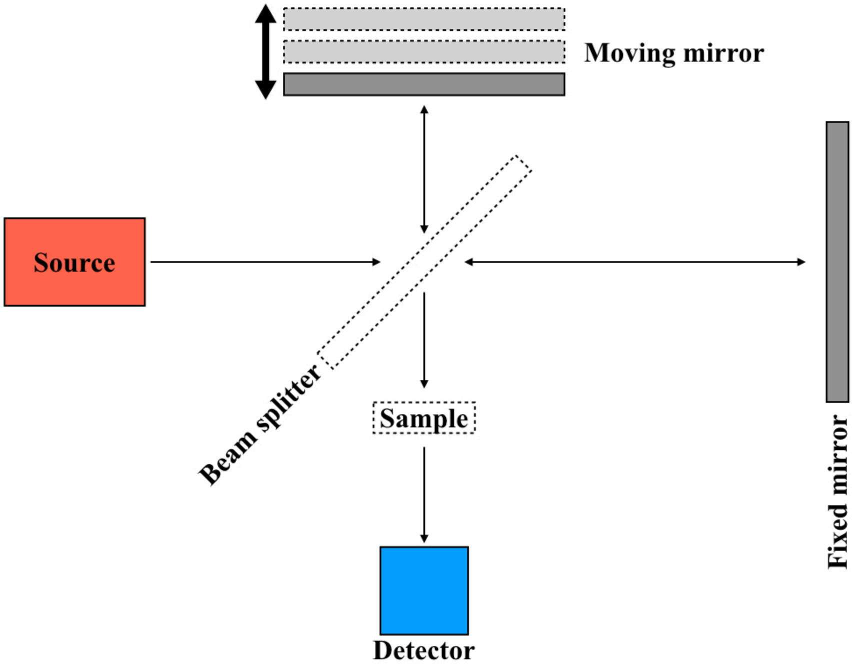

Figure 2.1. Simplified diagram of an FTIR spectrometer. The sample geometry presented is for transmission measurements, but reflection measurements are also possible.

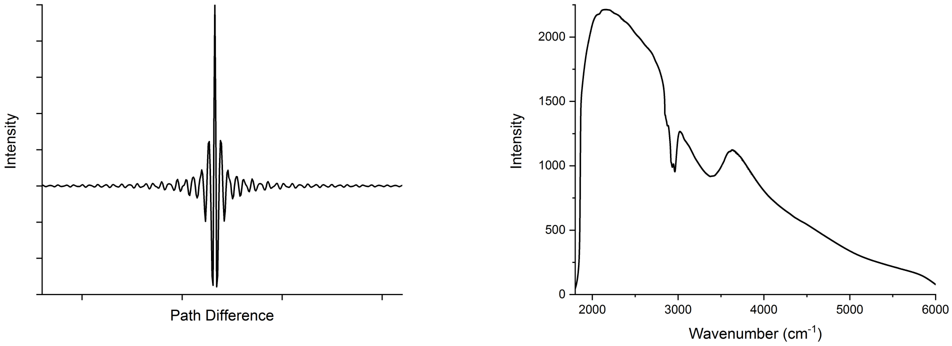

Figure 2.2. FTIR interferogram (left) and spectrum (right). Each contain the same information, but the spectrum is easier to read. The spectrum is the Fourier transform of the interferogram.

Fourier transform infrared (FTIR) spectroscopy is a powerful technique and the chief measurement method in this work. The technique uses a Michelson-style interferometer (figure 2.1). The four arms of the interferometer contain the infrared source, a fixed mirror, a moving mirror, and the sample and detector. The difference in path length between the mirror arms introduced by the moving mirror causes the light in the spectrometer to interfere with itself. The signal created by the interfering light is measured at the detector and recorded as a function of the moving mirror's position. The recorded signal is called an *interferogram* (figure 2.2). Fourier transforming the interferogram gives the intensity spectrum in a more readable format as a function of frequency (traditionally wavenumbers are the preferred units). Many interferograms can be collected by sweeping the moving mirror through its range of motion multiple times. The interferograms can then be averaged and transformed in order to reduce noise. Section 9.4 of McCluskey and Haller[12] and Panel XII of Ibach and Lüth[5] contain examinations of the mathematics behind the operation of Fourier transform spectrometers.

The system used for this work was a Bomem DA8 (DA stands for dynamic alignment). The source used for this work was a SiC rod known as a GloBar, but other sources like mercury or quartz lamps can be used depending on the wavelength range desired. A liquid nitrogen cooled InSb detector was used for its wide range and good sensitivity, but like the source, other options are available depending on the desired measurement window. Due to strong absorption by both air and water vapor, the interior of the instrument is evacuated and measurements are performed under vacuum.

Measurements can be performed at temperatures as low as 10 K by using a Janis closed-cycle helium cryostat or at ambient temperature in a separate sample compartment.

2.2: UV/Visible spectroscopy

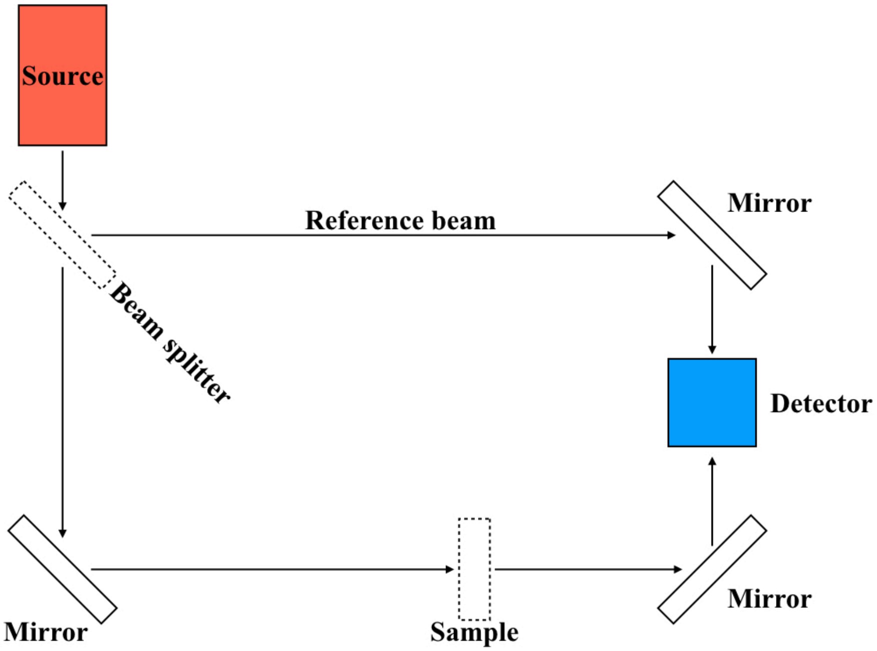

Figure 2.3. Simplified diagram of a UV/Visible spectrometer.

UV/Visible (UV/Vis) spectroscopy is a relatively simple measurement method. A simplified diagram of a typical UV/Vis spectrometer is shown in figure 2.3. Lamps with strong visible and UV emission are used in conjunction with monochromators. Intensity is measured directly as a function of wavelength, with a typical resolution of about 1 nm. Typically the ratio of intensity between a reference and sample beam are taken, giving a spectrum result in units of percent transmission as a function of wavelength in nanometers.

The UV/Vis range is important for studying defect states present in the bandgaps of semiconductors. Electrons present in the sample will absorb photons of specific energies to transition between the bands and defect levels. Such absorptions will be visible in the spectrum as a decrease in the transmission at the wavelengths of sufficient energy. Transmission will go to zero at wavelengths corresponding to and exceeding the bandgap energy.

The instrument used in this work was a Perkin Elmer Lambda 900 UV/Vis/NIR spectrometer, which is capable of performing measurements from 200-3300 nm. The UV source (200-320 nm) is a deuterium lamp and the Visible/Near-IR source is a tungsten filament lamp (320-3300 nm). A photomultiplier tube (200-850 nm) and PbS detector (850-3300 nm) serve as the collection devices. Measurements were performed under ambient conditions. As a general rule, this instrument's NIR capability is not utilized, since that range is better covered by the spectrometer discussed in the previous section.

2.3: Positron annihilation spectroscopy

Positron annihilation spectroscopy (PAS) is particularly suited for measuring negatively charged vacancies, but is near-surface sensitive. Positrons are the electron's antiparticle, and are positively charged as a result. When a positron encounters an electron, the pair is annihilated, giving off an energy burst that is detectable as gamma rays (511 keV). The momentum of the annihilated electron determines the amount of broadening in the energy distribution around the 511 keV peak, quantified as the center (S) and wing (W) parameters. Core electrons have more momentum than valence electrons, so annihilation of them gives a broader distribution (smaller S with respect to W). A narrow distribution (larger S relative to W) indicates annihilation occurred in a vacancy, since the positron is more likely to encounter valence electrons in those. Positrons can be trapped only by neutral or negative vacancies, since they will be electrostatically repelled by positively charged vacancies. PAS is only surface-sensitive since the probability of the positron becoming trapped and annihilated increases as a function of depth of penetration in the sample material, with typical penetration depths measured in µm.

PAS measurements presented or referenced in this work were performed by Marc Weber in the McCloy research group's facilities at Washington State University.

2.4: Hall effect

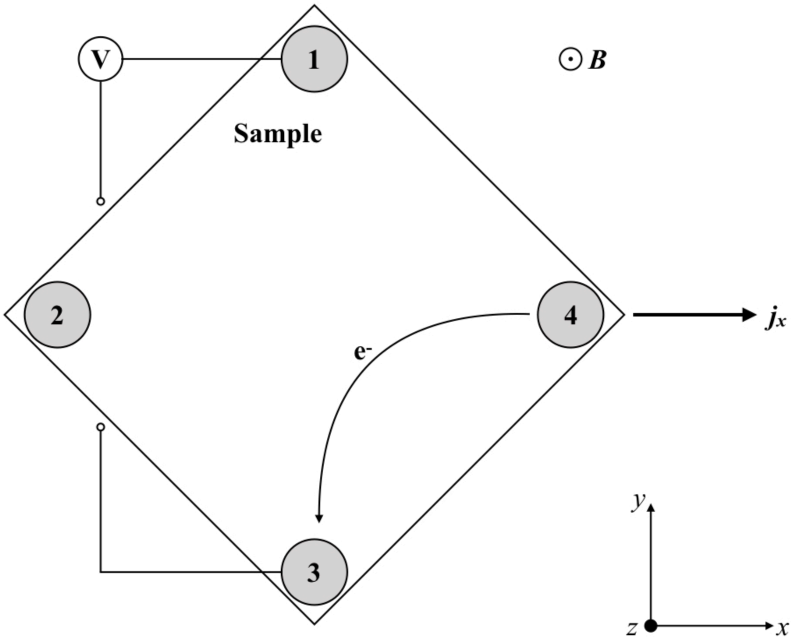

Figure 2.4. Hall effect measurement geometry. In the presence of a magnetic field, charge carrier motion deflects according to the Lorentz force. Once a steady-state is reached, the voltage across the sample is measured.

When considering only one charge carrier, the Hall effect can be analyzed simply with the Lorentz force. In the presence of an external magnetic field, the charge carriers deflect and build up on the edges of the sample (figure 2.4). This results in a quantity known as the Hall voltage that can be measured. The magnetic field and current are defined parameters in the experiment. Using them and the measured Hall voltage, it is possible to calculate quantities such as the charge carrier densities, mobilities, and resistivity of the sample. A full examination of the Hall Effect is available in section 8.3 of McCluskey and Haller.[12]

2.5: Other techniques

There are a host of other classification techniques, and the remainder listed here are not meant to constitute an exhaustive list.

2.5.1: Electron paramagnetic resonance

Electron paramagnetic resonance is used to characterize electrically active defects. Zeeman splitting occurs when the spin of an electron interacts with an external magnetic field. After the electronic spin degeneracy has been lifted by the application of a magnetic field, microwave photons can excite electrons to the higher-energy spin states. This is observed as an absorption pattern as the magnetic field is varied.

2.5.2: Raman spectroscopy

Raman spectroscopy is a complimentary technique to the FTIR spectroscopy discussed in section 2.1. Vibrational modes that are not visible in one are frequently visible in the other. Raman spectroscopy works by scattering high-energy photons (relative to FTIR) off the atoms in a sample. Some of the energy of the incident photons will excite lattice vibrations. The vibrations are determined by measuring the difference in energy between the incident and scattered photons.

2.5.3: Photoluminescence and photoluminescence emission

Photoluminescence and photoluminescence emission operate on an opposite principle from transmission spectroscopies. Rather than shining light through the sample and measuring drops in the received intensity, the sample is excited with high-energy light in order to promote electrons higher in the bandgap or conduction band. What is measured is the photons that are emitted by the sample as the electrons settle back to their ground states. In photoluminescence, the excitation energy is fixed and the spectrum of emitted light is swept by the detector. In photoluminescence emission, a range of excitations are swept and the intensity of a single emission energy is monitored.

2.5.4: X-ray diffraction

X-ray diffraction is a measurement technique that is used to give structural information about a sample. Since X-rays have wavelengths that are comparable to typical lattice constants in solids, they can be diffracted from the atoms in a lattice. Reflected intensity is measured as a function of incident angle on the surface of the sample, and peaks occur when the Bragg condition is met. The location of peak intensities can be used to calculate the distances between layers of atoms in the crystal, and the structure computed as a result.

2.5.5: Secondary ion mass spectrometry

Secondary ion mass spectrometry is a measurement technique that is used to determine the composition of a sample. A beam of ions is used to ablate the surface of a material, and the types of atoms that are ejected are determined with a mass spectrometer.

Since the constituent atoms are physically ejected from the sample surface, this method only gives information on the sample surface and not the bulk. It is very sensitive, however, and can detect very low concentrations of dopant atoms.

2.6: Anneals

Annealing is the process of baking a material in a particular way in order to alter its properties. In the context of semiconductors, annealing is performed to either introduce or remove specific defects in a controlled way. For example, annealing an oxide semiconductor under an evacuated environment will result in some of the oxygen atoms in the structure leaving as elemental or molecular oxygen, creating oxygen vacancies in the process. The opposite is also possible. Annealing under an atmosphere of oxygen gas will drive oxygen into the material and reduce the amount of oxygen vacancies as a result.

2.6.1: Sealed ampoules

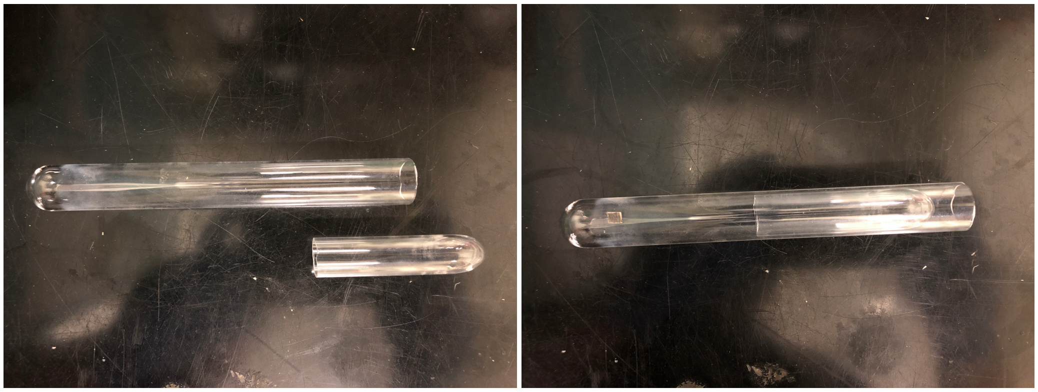

Figure 2.5. Ampoule and cap parts (left), and assembled for sealing with sample inside (right). From here, the ampoule would be sealed using an oxygen-hydrogen torch to melt the two pieces of silica together.

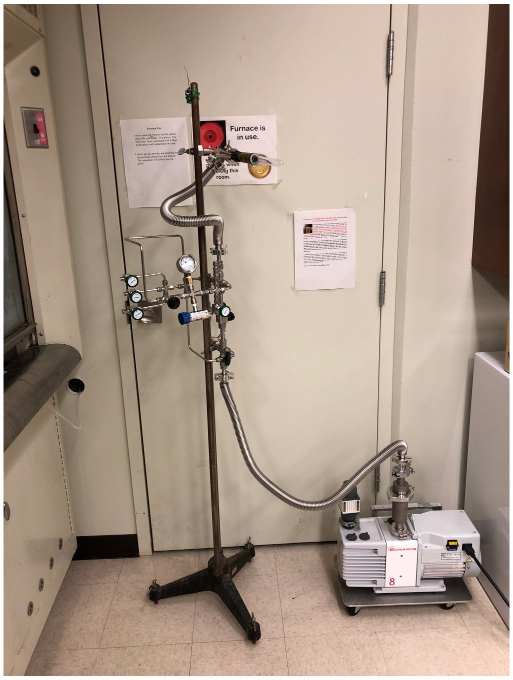

Figure 2.6. Ampoule sealing stand. The gas input manifold is on the left and the vacuum adaptor that accepts the ampoules is on the top. Various gauges and valves are used to monitor and control gas pressure in the ampoule.

Anneals performed on β-Ga_2O_3 samples were almost universally performed in sealed quartz ampoules. These allow the ambient gases and total pressure to be carefully controlled. The ampoules are two-part and consist of the main ampoule body and a cap that is inserted into the open end of the body. Once the silica parts are fused together with a torch, the ampoule has been sealed.

The ampoule is prepared first by washing the body and cap with acetone, isopropanol, and water so an airtight bond can be formed. Dust or other debris can interfere with the quality of the seal. The sample to be annealed is placed in the end of the ampoule and the cap after. The ampoule is then inserted into a vacuum adapter.

Using an oxygen-hydrogen torch, the cap is welded into place by melting the silica together in one place. Doing this prevents the cap from moving when vacuum is pulled on the system or when gas is introduced. The ampoule can be evacuated simply by using the attached pump. If an anneal under vacuum is desired, the ampoule can be sealed once the appropriate pressure is reached. If an anneal under a specific atmosphere is desired, the gas can be introduced by attaching a cylinder to the manifold. The system can be flushed by repeatedly filling and evacuating the gas to reduce atmospheric contamination. This process was performed from three to ten times, depending on the atmosphere desired. Gas was added up to 0.5 atmospheres of pressure, then the ampoule was sealed. The most common atmosphere used was hydrogen or deuterium, but oxygen was also used.

2.6.2: Flowing gas

Figure 2.7. Furnace with flowing gas tube.

Anneals performed on barium titanate were almost universally performed under a flowing atmosphere. This annealing method is referred to as a *flowing gas anneal*. The source gases were contained in cylinders and flow rates were controlled with a mass-flow controller or combined needle valves and flow meters. While only two gases were ever used in this apparatus, it would be possible to use up to four separate cylinders simultaneously with the limiting factor being the number of storage spaces in the room containing the furnace.

The flowing environment was created by placing a silica tube into a horizontal furnace fitted with Swagelok tube adaptors at either end. The sample to be annealed was placed inside the tube, then the adaptors attached. The gas sources were ultra-high purity (UHP) argon and 98% argon + 2% hydrogen. The 2% hydrogen gas flow was controlled with the mass-flow controller, which has a range of up to 5 standard liters per minute (sl/m). The UHP argon flow was controlled with a needle valve and measured with a flow meter. The UHP argon was passed through a bubbler containing high-performance liquid chromatography (HPLC)-grade water. Following the bubbler, the gas lines were combined and the relative humidity measured. High-quality plastic tube (polyethylene) was used to connect the components. The gas was vented to atmosphere inside a fume hood.

The target humidity for the preparation of persistent photoconductivity in BTO samples was 40%. The flow rate of the 2% hydrogen component gas was selected in the range of 1-8 standard cubic feet per hour (scf/h), and the UHP argon component was set to give the 40% relative humidity result.

CHAPTER THREE: CRYSTAL GROWTH

In the study of semiconductors, access to high-quality material is of paramount importance. As alluded to in chapter 1, high-quality does not necessarily translate to purity. Since semiconductors are frequently doped intentionally to favorably change their properties. Therefore, purity is not as much of a consideration compared to homogeneity. In the context of semiconductors, 'high-quality' therefore refers to the uniform distribution of desired defects and dopants throughout a single-crystal host material.

The process of making crystalline semiconductors is referred to as *growth*. When it comes to the final product, the result of a growth process is either a *bulk crystal* or a *thin film*. With respect to the size of any given constituent atom, a bulk crystal is infinitely large in all directions whereas a thin film has a definite length in one spatial dimension. Traditionally, the thickness range of a thin film extends from an atomic monolayer (approximately 1 nanometer) to the order of tens of micrometers. Thin films are not mechanically stable on their own and are grown on the surface of a separate material called a *substrate*. For the purpose of making useful devices such as diodes, transistors, or even solid-state lasers, many different films can be grown one on top of the other to create the electronic structures necessary.

The growth process for bulk versus thin film material is very different by necessity. Bulk methods generally require that large quantities of raw material be melted by resistive or inductive heating into the liquid phase and carefully recrystallized around a sacrificial crystal of known orientation called a *seed*. For thermodynamic reasons, the crystallographic orientation of the grown crystal is the same as the seed that is introduced to the melt. Due to the fine degree of control required, thin film growth methods are generally more complicated conceptually than their bulk counterparts. All thin film growth methods rely on carrying controlled amounts of the growth material from a source to the substrate.

The growth methods relevant to this work all generate bulk crystals, and so are more thoroughly emphasized in the following sections. Thin film deposition methods are so important to the field that a brief overview is obligatory. This examination of growth methods is not intended to be exhaustive, since thorough treatments of the subject can be found in textbooks such as McCluskey and Haller[12], Ibach and Lüth[5], and Yu and Cardona[11].

3.1: Bulk crystal growth

3.1.1: Czochralski method

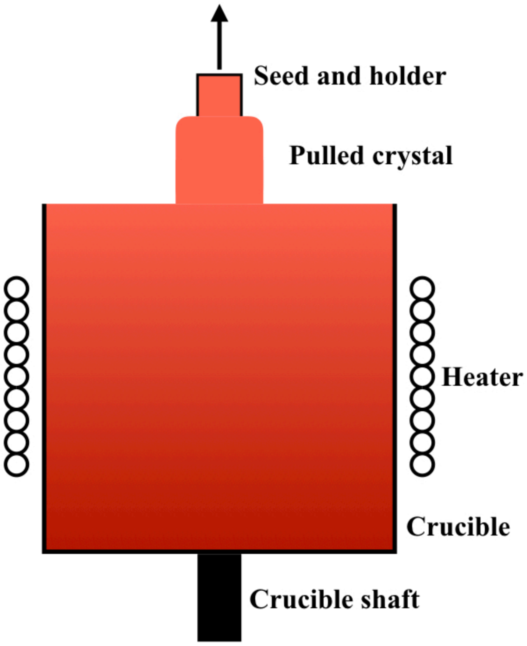

Figure 3.1. Schematic of the interior of a Czochralski crystal growth furnace.

The Czochralski process (abbreviated CZ, named for Polish scientist Jan Czochralski, figure 3.1) and its derivatives are widely used to grow bulk crystals on account of their flexibility and simplicity. The β-Ga_2O_3 samples used in this work were grown by Jani Jesenovec of the McCloy research group at the Institute for Materials Research at Washington State University using this method.

Czochralski growth is performed by first melting raw material in a crucible. The raw material, called a charge, can be a pre-prepared mass of polycrystalline solid or powder stock. Once the charge has melted, a solid seed crystal is introduced to the melt. By carefully controlling the temperature profile inside the furnace, the melt will solidify around the seed crystal. As this occurs, the seed and newly solidified crystal are slowly drawn from the melt as new material freezes in its place. Both the seed crystal and crucible are mounted to shafts that can be counterrotated to ensure uniform and symmetric growth.

The primary strengths of Czochralski growth are threefold: first the ability to rapidly grow large quantities of very high-quality crystal, second large silicon wafers for industrial use are routinely grown using this method and, third lattice defects are reduced by the constant contact of the melt and crystal.

Czochralski growth has very manageable weaknesses. While it is inevitable that the melt will become contaminated to at least some degree by the crucible material, this can be mitigated by careful selection of the crucible material and growth temperature. For this reason, crucibles are normally made from inert materials with correspondingly high melting points such as the noble metals, silica, and alumina. Materials with low melting points resist contamination more readily since impurity mobilities increase with temperature. Light doping can also be a challenge, due to the ratio of material volume involved in semiconductor growth, but can be accomplished by preparing a pure charge, and introducing a small amount of heavily doped material. Finally, while the method is conceptually simple, construction of a CZ furnace can be costly.

3.1.2: Czochralski-derived processes

There are three common alterations made to the Czochralski process, described above, based on material demands or a desired crystal geometry:

Liquid encapsulated Czochralski (LEC) is used to grow materials that have large vapor pressures in the liquid phase. A layer of flux is placed atop the melt to prevent evaporation by separating the melt from the furnace environment. This method is particularly important for the growth of arsenides and phosphides.

If a non-cylindrical crystal geometry is desired, the crystal can be pulled through a die placed on the melt surface. This geometry is edge-defined film-fed growth. Due to the solidifying front's contact with material other than the melt and final crystal (i.e. the top surface of the die), crystal quality can be impacted. The advantage gained is that shapes defined by the die surface can be grown, rather than just a cylindrical single crystal.[34]

In some cases, it may not be possible to grow a crystal directly from its own stoichiometric melt. This can be due to material properties such as an unfavorable phase change near the melting point or an unstable liquid phase. In these cases top-seeded solution growth (TSSG) can be used. In TSSG, the melt is stabilized by dissolving the material to be grown in a solvent or flux. This slows growth by requiring the crystal material to precipitate from the solution prior to solidification, but eases or allows growth of otherwise difficult or impossible materials. Barium titanate is grown with this method to avoid an unfavorable hexagonal to cubic phase change.

3.1.3: Verneuil

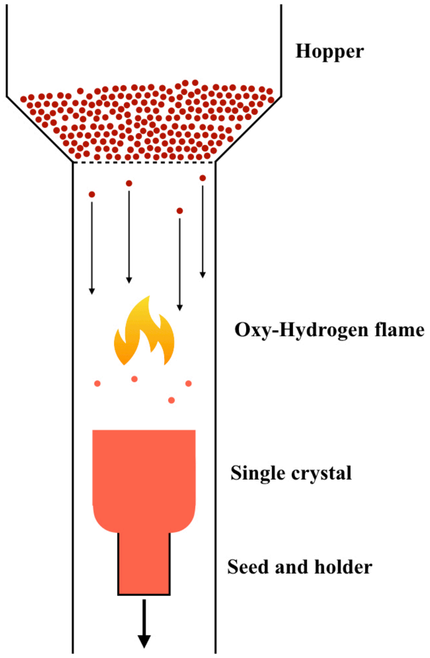

Figure 3.2. Verneuil crystal growth apparatus.

The Verneuil process, also known as flame fusion, was pioneered by Auguste Verneuil. Oxides such as alumina and $SrTiO_3$ are commonly grown using this method. As shown in figure 3.2, powdered material is held in a hopper and sifted at a controlled rate into a column with a hot zone (usually an oxy-hydrogen flame). As the molten material collects on the seed crystal at the bottom of the column, it solidifies. The seed is rotated to facilitate symmetric growth and the grown crystal is lowered as material accumulates to maintain an even liquid film on the surface near the flame.

Flame fusion is a relatively inexpensive process that is suitable for growing crystals with high melting points. It also eliminates a contamination source by forgoing the use of a crucible. Unfortunately, lattice faults are common in the final product due to the way molten material is added to the crystal. Macroscopic defects in the form of air bubbles are possible, and the diameter of the crystal product is limited.

3.1.4: Floating zone

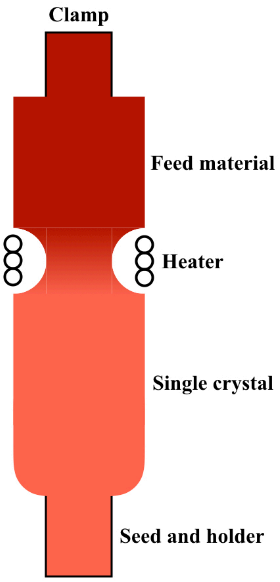

Figure 3.3. Floating zone crystal growth apparatus.

The floating zone method has similarities to CZ but does not use a crucible. Solid material, usually in the form of a polycrystalline rod, is passed through a hot zone, usually a radio frequency induction heater (figure 3.3). The feed material remains solid until it is passed through the molten zone. As with the previous methods, solidifying the molten material on a seed crystal yields a continuous growth of single crystal material.

The feed and seed ends of the crystal can be counterrotated, as with CZ growth, to ensure uniform growth. Widespread use of floating zone growth is largely restricted to silicon, but attempts with other materials are being explored.[46]

The lack of a crucible is the primary advantage of this method. As a result, there are few external impurity sources, especially when the process is performed under vacuum. Since only a portion of the material is molten at any given time, the floating zone method can also be used to purify existing single crystals by making use of dopant segregation effects at the solid-liquid interface.

The primary limitation of floating zone crystal growth is the growth radius, which is determined by the behavior of the liquid phase of the material, not the growth apparatus. The material being processed must also be stable in the liquid phase, since accommodations like liquid encapsulated Czochralski or top seeded solution growth are not possible when only a portion of the working material is melted at a time.

3.2: Thin films

As a general rule, methods that generate new atomic layers quickly do so at the cost of crystal quality and vice versa. There are three general methodologies for thin film growth:

3.2.1: Liquid phase epitaxy

To perform liquid phase epitaxy (LPE), a substrate is submerged in a solvent saturated with the film compound. Upon lowering the temperature of the growth apparatus, the solution becomes supersaturated and the film begins to deposit on the substrate. LPE is an inexpensive growth method due to low complexity (drastically less reliant on moving parts) and low temperature. The primary material processed with this method is GaAs. The generated layers are pure, but control over film parameters like thickness and flatness is lower than more sophisticated methods.

3.2.2: Chemical vapor deposition

Chemical vapor deposition (CVD) delivers film material to the substrate using a flowing carrier gas. A chemical reaction adsorbs the film components in the gas to the substrate and the excess products are expelled as exhaust. Growth rate can be precisely controlled by the amount of gas flow and multiple layers are made easily by appropriately changing the composition of the gas stream. The chief disadvantage of CVD methods is the use of dangerous gases like silane, phosphine, and arsine.

3.2.3: Physical vapor deposition

Physical vapor deposition (PVD) methods are similar to CVD methods in that the material to be deposited is delivered via the gas phase. They do not rely on chemical reactions though, as the atoms of the material being deposited are physically ejected in some way from a source and exist as a vapor in pure form.

The most sophisticated PVD method is molecular beam epitaxy (MBE). Performed under ultrahigh vacuum, MBE uses a series of ovens containing the growth materials to vaporize the desired film components. The streams of vapor phase atoms travel towards the substrate, where the growth process is monitored by methods such as mass spectrometry (measures growth stoichiometry) and electron diffraction (measures film growth). MBE is a very precise growth method and can be used to grow complex layers of multi-component films, but the apparatus to do so are expensive and growth is somewhat slow and not suited to large-scale film production.

CHAPTER FOUR: GALLIUM OXIDE

These papers are the result of the work presented in this chapter:

- Gallium vacancy formation in oxygen annealed β-Ga_2O_3

  J. Jesenovec, M.H. Weber, C. Pansegrau, M.D. McCluskey, K.G. Lynn, and J.S. McCloy, Journal of Applied Physics **129**, 245701 (2021).[47]
- Zinc-hydrogen and zinc-iridium pairs in β-Ga_2O_3

  C. Pansegrau, J. Jesenovec, J.S. McCloy, and M.D. McCluskey, Appl. Phys. Lett. **119**, 102104 (2021).[30]
- Persistent Room-Temperature Photodarkening in Cu-Doped β-Ga_2O_3

  J. Jesenovec, C. Pansegrau, M.D. McCluskey, J.S. McCloy, T.D. Gustafson, L.E. Halliburton, and J.B. Varley, Phys. Rev. Lett. **128**, 077402 (2022).[48]

4.1: Sample preparation

β-Ga_2O_3 crystals were grown by the McCloy research group (Institute for Materials Research, Washington State University) using the Czochralski method discussed in chapter 3. Crystals from three separate growth preparations were used, but growth technique was generally similar.[20,32,33,49,50] High purity (99.999%) gallium oxide powder is mixed with an additive (99.9% ZnO powder, 99% Cu_2O powder, both to 0.25 at.%) for doping, where appropriate. Mixing is achieved by ball milling for 18 hours. Two charges are prepared from the powder mixture in an isostatic press, then calcined at 1500ºC for 15 hours. The two charges are melted sequentially in an iridium crucible. Crystal growth occurs at 1830ºC with typical pull and rotation rates of ~2 mm/hour and ~2 rpm, respectively (CZ). The remainder of the melt is cooled at ~2ºC/min to produce a vertical gradient freeze (VGF) crystal. Samples are prepared from the crystal by cleaving along the (100) plane and cutting with a wire saw. Samples used in this work were typically ~5×5×1 mm. Specific sample dimensions, where relevant, will be listed. Unless otherwise specified, light in optical measurements was incident perpendicular to the (100) surface.

4.2: Gallium vacancy

Nominally undoped samples were prepared as described in section 4.1. The samples were analyzed by Jani Jesenovec and Marc Weber using depth-resolved positron annihilation spectroscopy and electrical measurements. Hall measurements were not possible due to high resistivity ($> 10^7$ Ω cm), therefore resistivity was estimated using I-V measurements in a two-point geometry. Full experimental details can be found in Jesenovec *et al*.[47]

V_{Ga} density was measured as a function of annealing temperature in O_2, with distinct behavior observed in four temperature ranges; 25-730ºC, 730-1200ºC, 1200-1400ºC, and > 1400ºC. Low temperature (~10 K) FTIR measurements were performed on samples annealed in the first three of these ranges (no anneal, 1010ºC, and 1400ºC) using the instrumental configureation described in section 4.3.1. O_2 anneals were performed by Jani Jesenovec in a flowing atmosphere for 15 hours. Subsequent H_2 anneals were performed in sealed ampoules (0.5 atm, as described in section 2.6.1) at 860ºC for 3.5 hours.

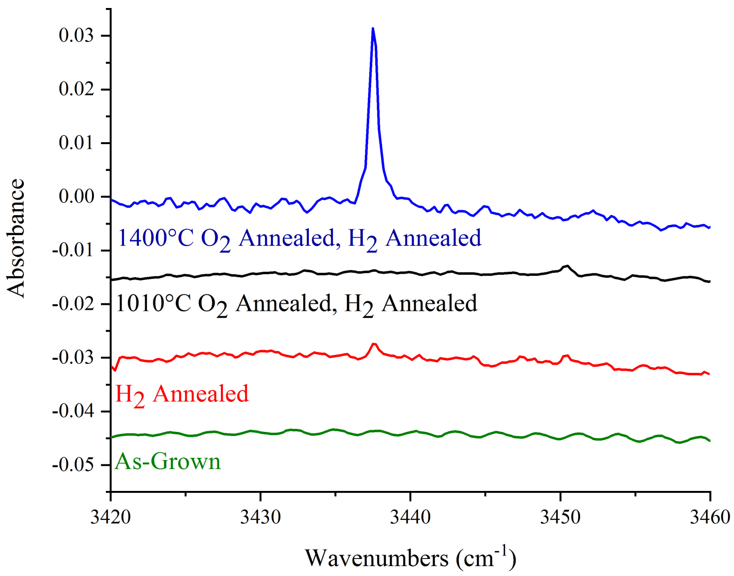

Figure 4.1. Low-temperature IR absorption spectra of unintentionally doped β-Ga_2O_3, annealed under the listed conditions. The reference was a constant. Spectra have been distributed vertically for clarity. The sinusoidal fringes in the as-grown spectrum (green) are the result of interference between β-Ga_2O_3's layer structure. These data were published in Jesenovec *et al.*[47]

V_{Ga} isn't IR-active until it complexes with H to form V_{Ga}-2H, thus necessitating the treatment in H_2. This is evident in figure 4.1 with the appearance of the 3438 cm^{-1} absorption peak following an anneal in hydrogen (green and red spectra, respectively), which has been assigned to the V_{Ga}-2H defect.[51] A second small absorption peak is present at 3450 cm^{-1} in the hydrogen-only and 1000ºC O_2 anneal (red and black spectra, respectively) spectra. This peak has been assigned to an IrH complex, and varies in intensity based on Ir concentration.[31] Its absence in the 1400ºC O_2 annealed spectrum (blue) is likely explained by the sample being cut from a portion of the crystal that was far from the iridium parts in the furnace (most notably, the crucible and seed holder), and being relatively Ir-poor as a result.

Sample	**Thickness (cm)**	**Integrated Absorbance**	**Defect Density (cm^{-3})**
1400ºC O_2, H_2 annealed	0.070	0.0187788	6.2×10^{15}
1010ºC, H_2 annealed	0.060	-	-
H_2 annealed	0.094	0.0013300	3.3×10^{14}

Table 4.1. V_{Ga}-2H densities calculated from peak areas in Figure 4.1. Integrated absorbances were obtained using the GRAMS32 tool included in the FTIR instrument software.

The density of V_{Ga}-2H can be estimated using equation 1.18 (table 4.1). Using $A = 10^{16}$ cm^{-1} as an estimate of the calibration factor for the defect gives an order-of-magnitude result.[52] This result should be considered a lower bound, since it is likely that not all of the V_{Ga} was able to form V_{Ga}-2H in the anneal process. No value was calculated for the 1010ºC O_2 annealed sample since no obvious peak was present.

It is apparent that V_{Ga} formation occurs when annealed under O_2 at 1400ºC and above. Reasons for the disappearance of V_{Ga} following the 1010ºC O_2 anneal are not clear, but potential explanations include interactions with other defects such as O_i and V_O or defect geometries that prevent the formation of IR-active V_{Ga}-2H.[53,54] This implies that V_{Ga} may be present but not observable when annealed under O_2 at ~1000ºC when using a hydrogenation technique. PAS results indicate a decreasing diffusion length L, in this temperature range, which indicates an increase in the density of positron-trapping defects near the sample surface. It may be possible that the defects detected by PAS need to be diffused into the sample at higher annealing temperatures in order for them to be detected by a bulk-sensitive measurement like transmission FTIR.

4.3: Zn acceptor in β-Ga_2O_3

4.3.1: Experimental details

β-Ga_2O_3:Zn doped to 0.25 at.% was prepared according to the method described in section 4.1. Infrared measurements were performed using a Bomem DA8 vacuum Fourier transform infrared (FTIR) spectrometer equipped with a SiC source, KBr beamsplitter, and InSb detector. Infrared spectra were collected at ~10 K with a resolution of 0.5 cm^{-1}. Low temperature measurements were obtained using a Janis closed-cycle helium cryostat. UV/Visible transmission spectra were collected using a Perkin Elmer Lambda 900 Series UV/Vis/NIR spectrometer under ambient conditions. Samples used were 2.05 and 2.12 mm thick. The 2.05 mm sample was used in the following as-grown and oxygen annealed measurements. The 2.12 mm sample was annealed in deuterium. Both samples originated from the CZ (pulled crystal) portion of the growth. A Keithley 6487 picoammeter was used to perform electrical measurements using pressed indium contacts in a two-point geometry. Hall measurements were not performed due to the large resistances measured (~TΩ).

4.3.2: ZnH complex

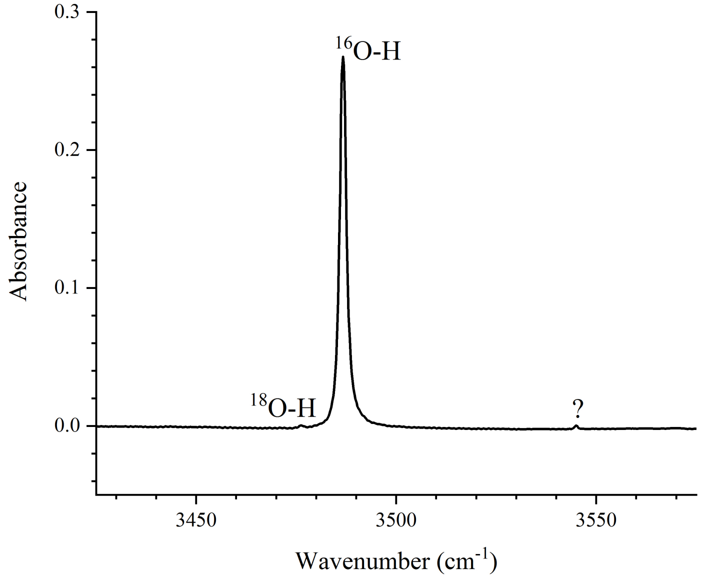

Figure 4.2. Low-temperature IR absorption spectrum of the O-H region in β-Ga_2O_3:Zn. The reference spectrum was a blank. The ^{16}O-H and ^{18}O-H peak assignments are labeled accordingly and the unidentified peak is labeled with a '?'. These data were published in Pansegrau *et al.*[30]

FTIR measurements revealed hydrogen incorporation was significant in the as-grown samples. Because of this, a dedicated hydrogen treatment was not necessary to introduce the O-H modes. Three peaks (3476.1, 3486.7, and 3545.0 cm^{-1}) are visible in the region where O-H modes are expected (figure 4.2). The largest absorption peak that occurs at 3486.7 cm^{-1} has been assigned as the ZnH complex associated with Zn occupation of the Ga(II) site. The small peak at 3476.1 cm^{-1} has been assigned to the same complex, but involves a heavier ^{18}O atom. This is corroborated by both the frequency shift and relative peak areas. Studies of O-H complexes in GaAs agree with the frequency ratio 3486.7/3476.1 = 1.0030 observed here.[55] The ratio of integrated absorbances (~0.003) is close to the natural relative abundance of ^{18}O (0.002).

The third peak at 3545.0 cm^{-1} was also observed in β-Ga_2O_3:Mg.[29] Its intensity was observed to vary across samples (and was absent in one of the samples used in this work). This peak's presence in Zn- and Mg-doped samples implies it is independent of both dopants, so the culprit is likely an undetermined acceptor-H complex.

4.3.3: Iridium electronic transition and sidebands

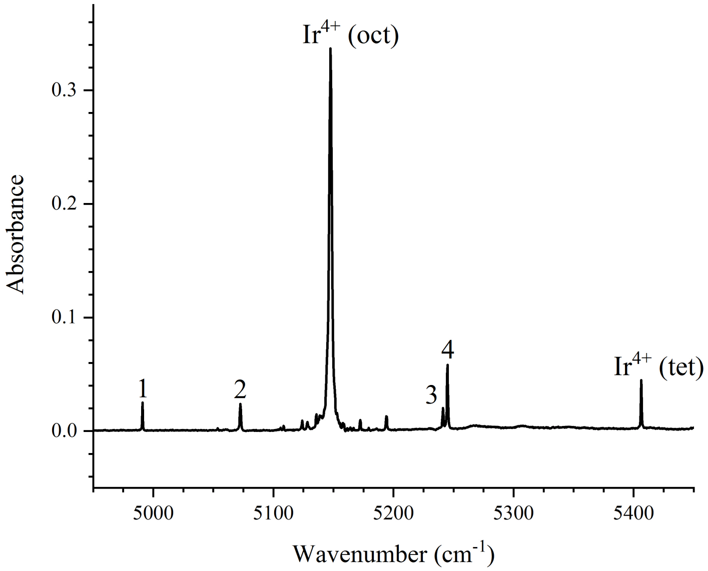

Figure 4.3. Low-temperature IR absorption spectrum of the Ir^{4+} main peak and sideband field in β-Ga_2O_3:Zn. The reference spectrum was a blank. The known isolated Ir^{4+} peaks are labeled (oct) and (tet) according to iridium occupation of the Ga(II) or Ga(I) sites, respectively. These data were published in Pansegrau *et al.*[30]

Ir^{4+} peak positions (cm^{-1})	Relative Height (Mg)	Relative Height (Zn)
4991.0		0.073
5053.8		0.006
5072.5		0.069
5092.4	0.015	
5106.0	0.054	0.007
5108.6		0.012
5124.6 (5124.0)	0.005	0.026
5128.0 (5128.4)	0.001	0.022
5129.7		0.010
5133.5 (5133.3)	0.021	0.008
5135.8		0.042
5138.7		0.039
5139.6	0.112	0.039
5147.6 (primary)	1.000	1.000
5152.6 (5152.9)	0.020	0.045
5154.4 (5154.0)	0.034	0.028
5155.4		0.021
5157.2 (5157.9)	0.018	0.019
5158.8 (5158.9)	0.060	0.016
5161.4		0.005
5163.4 (5163.5)	0.040	0.005
5164.3		0.007
5166.7		0.006
5170.3	0.008	
5172.4		0.027
5173.2	0.010	
5179.4	0.053	0.007

Ir^{4+} peak positions (cm^{-1})	Relative Height (Mg)	Relative Height (Zn)
5185.2	0.018	
5186.2		0.005
5194.3		0.037
5241.2		0.058
5245.0		0.171
5406.3		0.131

Table 4.2. Peak locations for Ir^{4+} sidebands in β-Ga_2O_3:Mg and β-Ga_2O_3:Zn. Data for the Mg-doped case were taken from Ritter *et al.*[31] Wavenumbers listed in parentheses correspond to the Mg-doped case where the difference in peak location was less than 1 cm^{-1}. A blank entry indicates there is no peak present at that location. A portion of these data were published in the supplementary information for Pansegrau *et al.*[30]

A large field of absorption peaks is present from 5000-5400 cm^{-1} (figure 4.3, table 4.2). The peak at 5147.6 cm^{-1} has been assigned to an internal electronic d-orbital transition in the Ir^{4+} atom on the octahedrally-coordinated Ga(II) site.[29,31,56–58] The corresponding peak for a tetrahedrally-coordinated Ir^{4+} is observed at 5406.3 cm^{-1}. The other peaks in the field are attributed to ZnIr pairs. These are formed when a nearby Zn atom perturbs the energy of the Ir^{4+} electronic transition based on the locations of the metal atoms relative to each other. The peaks labeled 1-4 in figure 4.3 correspond to 4991.0, 5072.5, 5241.2, and 5245.0 cm^{-1}, respectively. Due to their prominence here, absence in Mg-doped crystals, and the known Ga(II) site preference of Mg, these peaks are proposed to correspond to a ZnIr pair with Zn occupation of the tetrahedral Ga(I) site.[59,60]

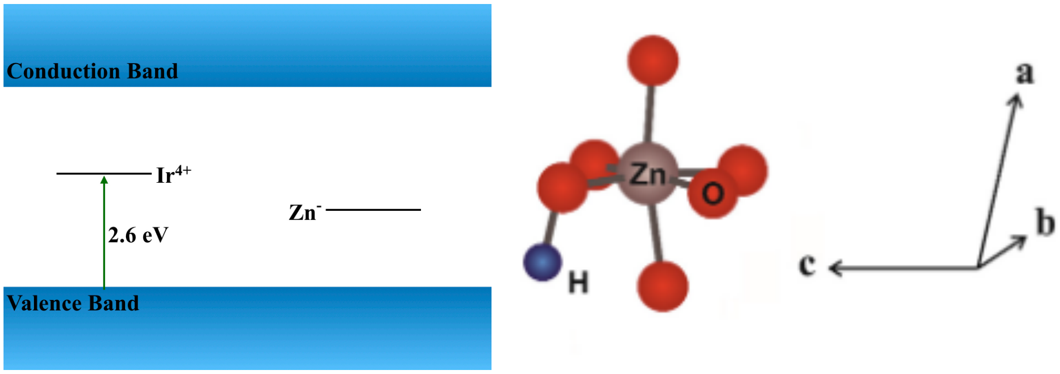

Figure 4.4. Band diagram of the Ir^{4+} and Zn^{-} defect levels (left) and proposed ZnH structure (right) as presented in Pansegrau *et al.*[30]

The presence of Ir in these crystals is a consequence of the use of an iridium crucible in the growth process.[34] At the growth temperature (1830ºC), some diffusion of the crucible material into the melt is inevitable. In undoped samples, Ir is present in the IR-inactive 3+ charge state, and not visible.[29] Since Ir^{3+} is a donor, doping with an acceptor transfers an electron from the Ir to the acceptor, changing the charge to Ir^{4+}. This is the charge state that is visible as the 5147.6 and 5406.3 cm^{-1} peaks, depending on the location of the Ir atom. Passivation of the acceptors, like that shown in Ritter *et al.*[29,31], reverses that charge transfer, which causes the iridium to return to the IR-inactive 3+ charge state.

4.3.4: Polarized infrared measurements

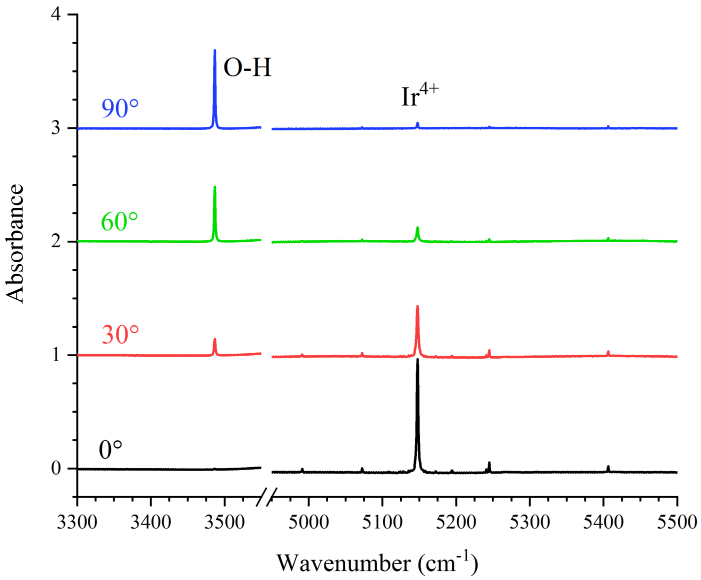

Figure 4.5. Low-temperature IR absorption spectra of β-Ga_2O_3:Zn taken with a linear polarizer. The reference was a blank (taken without the polarizer). The angles listed are measured with respect to the **b**-axis (0º indicates parallel, 90º indicates perpendicular). These data were published in Pansegrau *et al.*[30]

The polarization behavior of the sample was checked by inserting a ThorLabs wire grid linear polarizer into the beamline in front of the sample (figure 4.5). The behavior matches that observed in Mg-doped samples.[29,31] The Ir^{4+} peak and sidebands are maximized when **E**//**b** and the ZnH peak is maximized when **E**//**c**. This indicates the O-H bond of the ZnH complex lies in the *a*-*c* plane (figure 4.4, right).

4.3.5: Deuterium anneal

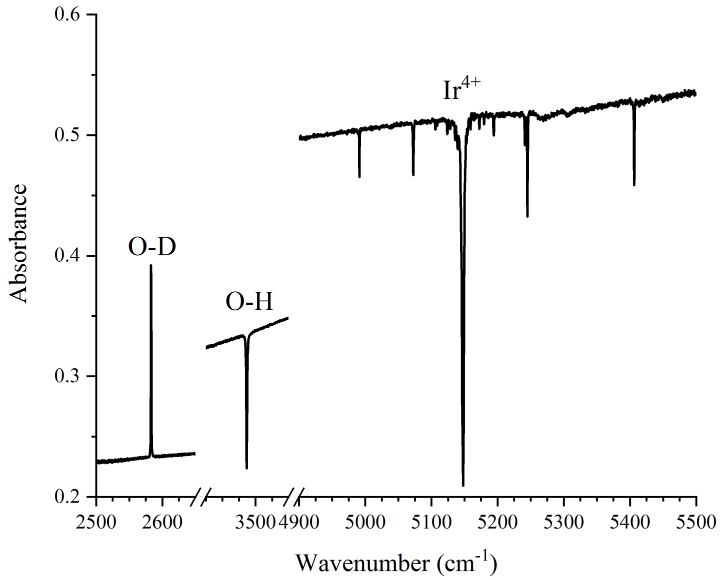

Figure 4.6. Low-temperature IR absorption spectrum of deuterium-annealed β-Ga_2O_3:Zn. The reference spectrum was the as-grown state. These data were published in Pansegrau *et al.*[30]

In addition to polarization, the O-H assignment can also be checked by replacing the hydrogen with deuterium and observing the frequency shift. A sample was deuterated by sealing it in an ampoule with 0.5 atm of D_2 at room temperature, then annealing for 3.5 hours at 860ºC. At the conclusion of the anneal, the ampoule was removed from the furnace and quenched in water. Prior to annealing, two-point resistance measurements were 0.3-0.6 TΩ. Following the anneal, this value dropped to ~0.045 TΩ. In addition, the sample turned from a slight yellow to grey.

A new peak at 2582.9 cm^{-1} was observed (labeled O-D in figure 4.6), giving the expected isotopic shift ratio of ~1.35, as seen in other experiments.[29,52,61,62] The ^{18}O-H and unidentified peaks either did not generate deuterium analogs, or the analogs were not visible. The features observed in the as-grown state (labeled O-H and Ir^{4+} in figure 4.6) are visible in the absorbance as dips, rather than peaks, which indicates a relative intensity reduction as a result of the D_2 anneal.

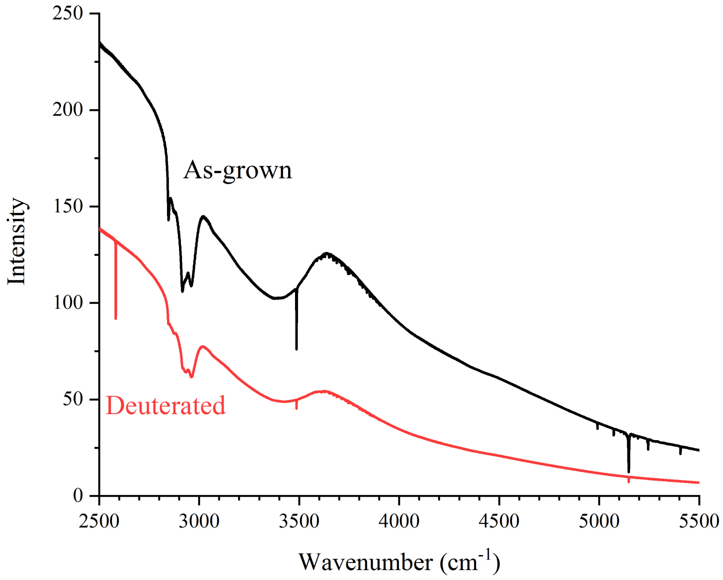

Figure 4.7. Low-temperature IR intensity spectra of β-Ga_2O_3:Zn in the as-grown (black) and D_2-annealed (red) states. These spectra were used to calculate the absorbance presented in figure 4.6. Features at 2800-3000 cm^{-1} are organic contaminants in the system.

Examination of the transmission intensity plots (figure 4.7) clarifies changes caused by deuteration. The 2582.9 cm^{-1} peak, as expected, is totally absent from the as-grown spectrum. The 3486.7 cm^{-1} and 5147.6 cm^{-1} peaks are greatly reduced in intensity from the as-grown to the deuterated spectrum, but are not totally gone. The D_2 annealing atmosphere causes hydrogen to leave the sample, reducing the intensity of 3486.7 cm^{-1} peak. The deuteration also causes the reduction of the 5147.6 cm^{-1} peak by passivating zinc acceptors (described at the end of section 4.3.3). Figure 4.8 highlights the effect of deuteration on the Ir^{4+} peak and siebands. The sidebands are gone following the anneal, indicating separation of the ZnIr pairs.

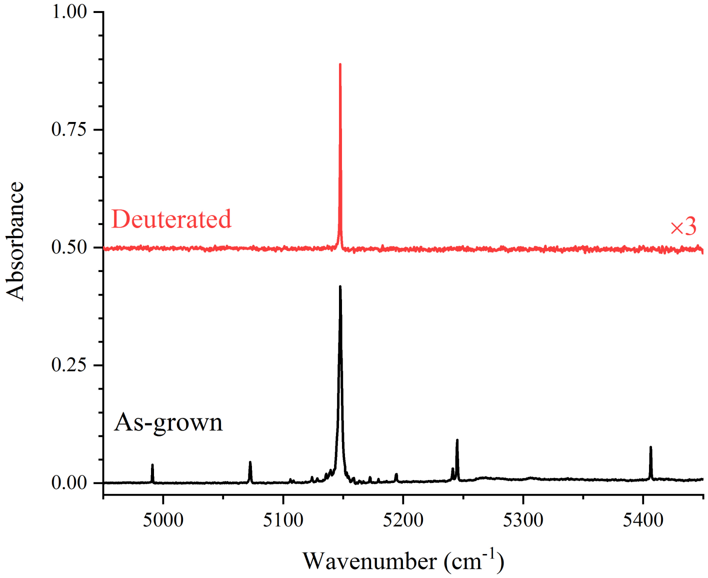

Figure 4.8. Low-temperature IR absorption spectra of the Ir^{4+} and sideband region in β-Ga_2O_3:Zn for the as-grown and deuterium-annealed states. The reference spectrum was a blank. The deuterated spectrum was shifted vertically for clarity, then multiplied to normalize the height of the Ir^{4+} peak.

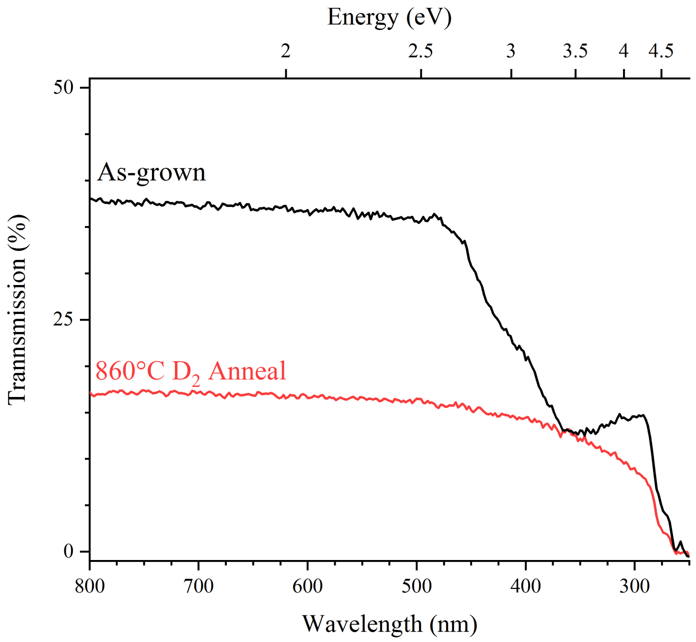

Figure 4.9. UV/Visible transmission spectra of β-Ga_2O_3:Zn in the as-grown and deuterated states. These data were published in Pansegrau *et al.*[30]

A 2.6 eV (~480 nm) absorption threshold is observed in as-grown β-Ga_2O_3:Zn (figure 4.9). An identical feature is present in β-Ga_2O_3:Mg and is due to the excitation of a valence band electron to the Ir^{4+} defect level (figure 4.4, left). Passivating the Zn (Mg) with the D_2 (H_2) anneal suppresses the 2.6 eV absorption by filling the Ir^{4+} level, returning the Ir to the 3+ charge state (see section 4.3.3). Band edge absorption is observed beginning at 4.5 eV (~275 nm) in both spectra.

4.3.6: Oxygen anneal

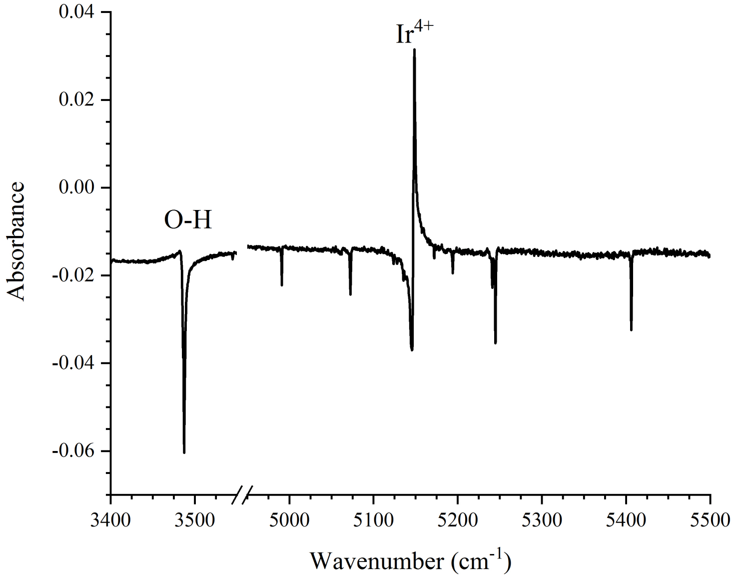

Figure 4.10. Low-temperature IR absorption spectrum of oxygen-annealed β-Ga_2O_3:Zn. The reference spectrum was the as-grown state. These data were published in Pansegrau *et al.*[30]

A sample was annealed in 0.5 atm of O_2 twice. Each anneal was performed in a sealed silica ampoule for 15 hours. The first anneal was performed at 1000ºC and the second at 1200ºC. The ampoules were quenched in water at the conclusion of each anneal. Two-point electrical resistance increased from 0.3-0.6 TΩ (as-grown) to 1.3-1.6 TΩ (1000ºC anneal) and 1.9-2.1 TΩ (1200ºC anneal). Optical results were not significantly different, so figure 4.10 shows the result of only the 1200ºC anneal. Infrared absorbance using the as-grown sample as a reference shows the ZnH peak as well the Ir^{4+} sidebands decreased slightly and the isolated Ir^{4+} (oct) peak increased (figure

4.10). The increase in electrical resistance and decrease of the ZnH peak together indicate that annealing in an O_2 atmosphere activates the Zn acceptors by driving H out of the sample. A decrease in the Ir^{4+} sidebands indicates separation of ZnIr pairs, as discussed in the previous section. A previously unnoticed sideband at ~5145 cm^{-1}, due to its proximity to the large main peak, is now visible as a dip.

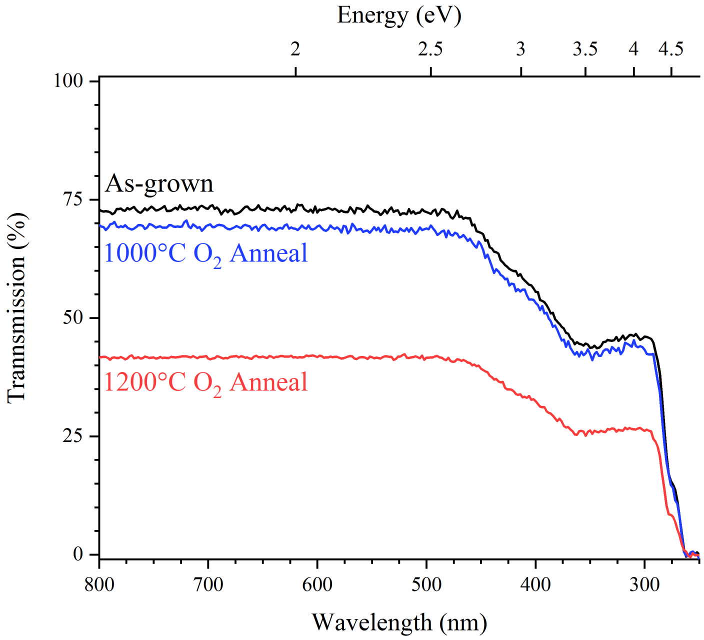

Figure 4.11. UV/Visible transmission spectra of β-Ga_2O_3:Zn in the as-grown and oxygen-annealed states. The large offset of the 1200°C spectrum is the result of a difference in mounting procedure between experimental runs, not a change in the material.

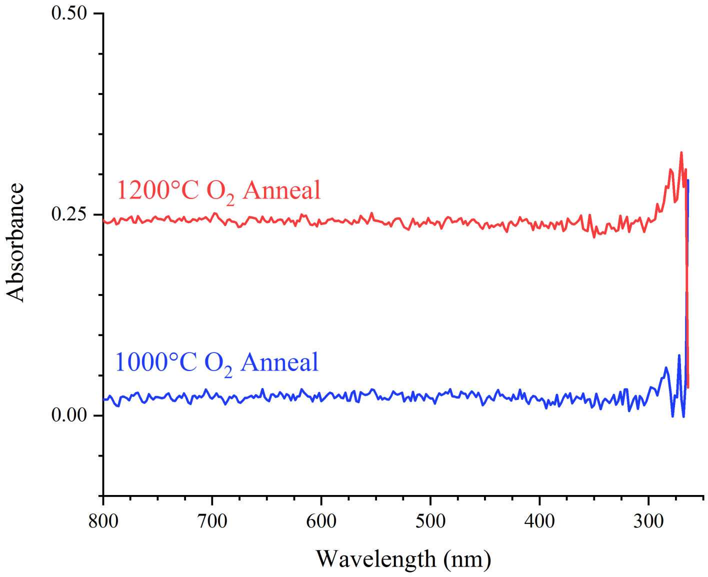

Figure 4.12. Absorbances computed from the transmission spectra in figure 4.11. The reference spectrum was the as-grown transmission. Since the results are constant values, the spectra are simple multiplications of each other.

Whether the 1200ºC O_2 anneal changed the character of the UV/Vis spectrum in figure 4.11 can be checked by comparing the spectra as an absorbance. Using the as-grown spectrum as the reference, it can be seen that both the 1000ºC and 1200ºC anneals result in flat lines (within noise) until the transmission spectra approach zero near the 350 nm mark. Due to the behavior of logarithms near zero, the absorbances in the UV region (>300 nm) of figure 4.12 should not be taken to indicate a change as a result of the anneal.

4.3.7: Low-temperature light exposure

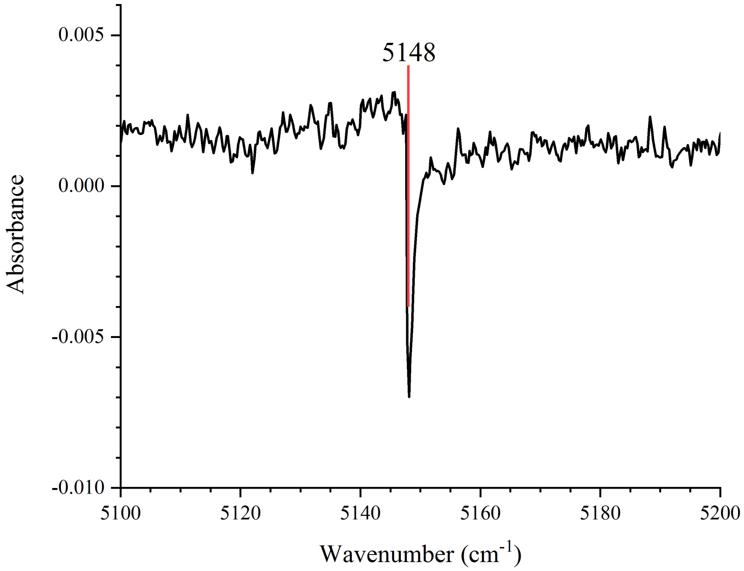

Figure 4.13. Low-temperature IR absorption spectrum of as-grown β-Ga_2O_3:Zn after exposure to a 375nm LED. The reference spectrum was the same sample prior to illumination. Notice the y-axis scale is small.

A replication of the LED exposure experiment presented in figure 8 or Ritter *et al*[31] was attempted. The sample holder in the FTIR cryostat was rotated so that the sample's (100) surface made a 45° angle with the infrared beam. This was done to allow an external LED to illuminate the sample at the same time as the FTIR measurement was performed. Figure 4.13 shows the result of illuminating the sample. Only the 5147.6 cm^{-1} peak is visible as a dip, indicating light energy from the LED promoted some valence band electrons to the Ir^{4+} defect level (figure 4.4, left). The distinct decrease in the sidebands, as seen in Ritter *et al*[31], was not observed.

4.3.8: Discussion and conclusions

Sample	Thickness (cm)	Peak	Integrated Absorbance	Defect Density ($\times 10^{16}$ cm^{-3})
X3-5	0.205	O-H as-grown	0.65	7.3
X3-5	0.205	O-H oxygenated	0.53	6.0
X3-6	0.212	O-H as-grown	0.24	2.6
X3-6	0.212	O-H deuterated	0.044	0.48
X3-6	0.212	O-D deuterated	0.13	1.4

Table 4.3. O-H densities calculated from the peak areas presented in previous sections. Integrated absorbances were obtained using the GRAMS32 tool included in the FTIR instrument software.

The density of the ZnH complexes can be estimated with the same method used in section 4.2, again using $A = 10^{16}$ cm^{-1} and the other parameters listed in table 4.3. Behavior of the β-Ga_2O_3:Zn samples matches generally with that observed in β-Ga_2O_3:Mg. A single large peak attributed to an acceptor-H complex was observed as well as a large Ir^{4+} peak and sideband field. Deuteration generated an isotopic frequency shift of ~1.35, and no intermediate peaks were observed, indicating the complex involves only a single H-atom. The ZnH and ZnD line-widths are narrower than their MgH and MgD counterparts; 1.4 and 0.6 cm^{-1} versus 2.5 and 1.5 cm^{-1}, respectively. This is potentially due to longer vibrational lifetimes, caused by a lesser degree of coupling with lower-frequency vibrational modes. In β-Ga_2O_3:Zn, the Ir^{4+} sidebands are stronger, more numerous, and spread over a wider spectral range than those observed in Mg-doped crystals. The prominence of several new sideband peaks (table 4.2) is taken as evidence of $Zn_{Ga(I)}$. Polarization behavior of Zn- and Mg-doped crystals was identical, with the Ir^{4+} peak maximized when **E**//**b** and the O-H bond was determined to line in the *a-c* plane, perpendicular to the **b**-axis (figure 4.5).

Despite evidence of $Zn_{Ga(I)}$ in both the Ir^{4+} sideband field and electron paramagnetic resonance (EPR) results[60], a second ZnH peak corresponding to Zn occupation of the tetrahedral Ga(I) site was not observed. EPR indicated ~5-10% of Zn occupied the Ga(I) site. This can be explained if the Ga(I) site does not bind H as strongly as the Ga(II) site and/or the EPR signature was not due to isolated Zn, but rather ZnIr pairs. The ZnIr pair model proposed here would be consistent with the observed Ir^{4+} sideband field (figure 4.3 And table 4.2).

Alternative explanations of the resistance increase when oxygen annealed could include filling V_O or forming V_{Ga}. The results presented in section 4.2 imply that more dramatic changes could be observed if higher annealing temperatures (~1400ºC) were used. A significant decrease in the ZnH peak and/or the appearance of the V_{Ga}-2H peak would narrow these potential explanations. Regardless, the large increase in electrical resistance observed following the O_2 anneals is promising for device fabrication applications that require semi-insulating substrate material.[19,28,29,59,63]

4.4: Persistent photochromism in β-Ga_2O_3:Cu

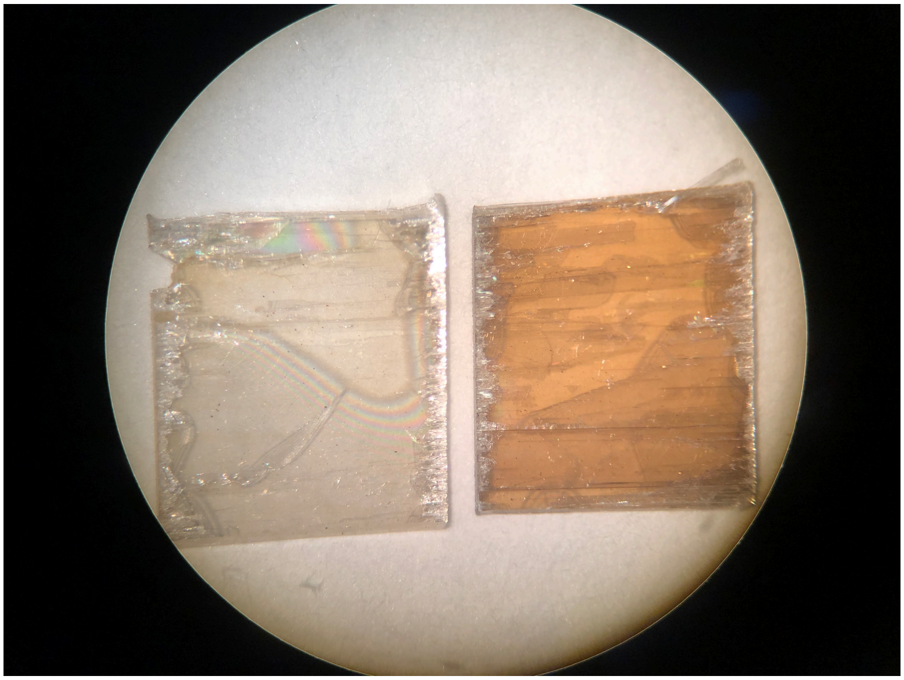

Figure 4.14. Image of β-Ga_2O_3:Cu samples with their coloration as-grown (left) and photodarkened (right). Notice Newton's rings interference (faint rainbow patterns), particularly in the left sample, which indicates delamination between layers.

Exposure to sub-bandgap light (275 nm, ~4.5 eV) for a short period of time (~60 seconds) causes β-Ga_2O_3:Cu to change color (figure 4.14). This color change was observed to persist in time for approximately one month. UV/Visible measurements reveal the color change is a result of a significantly increased absorption in the green-blue region of the visible spectrum. As a result, this effect is not so much a color *change* as it is an intensification of the crystals' intrinsic color. Therefore, this phenomenon will be referred to as *photodarkening*, since the effect is induced by light and results in the crystal taking on a darker color. This effect was observed to persist for approximately one month if left undisturbed, or it could be erased by annealing on a hot plate at 400ºC for ~5 minutes in air.

4.4.1: Experimental details

β-Ga_2O_3:Cu doped to 0.25at.% was prepared according to the method described in section 4.1. FTIR and UV/Vis instrumentation was used in the same configuration as described in section 4.3.1. Photodarkening was achieved using UV LEDs sourced from ThorLabs that were mounted to metal-core printed circuit boards. Erasing was performed in air on a hot plate set to 400ºC. Unless otherwise specified, samples used in this work were sourced from the VGF (remaining melt, not the pulled portion of the crystal) portion of the crystal due to more pronounced darkening. Interference fringes in FTIR spectra were mitigated as much as possible by using the ZAP function in the GRAMS32 software, but the interior lamella had a tendency to separate (figure 4.14, left sample) and cause strong internal reflections of the IR light. For this reason, many of the IR absorption presented in the following sections were computed using a constant as the reference, rather than another "genuine" spectrum. This serves the dual purpose of being able to work in traditional absorbance units and reduce the presence of interference fringing in the spectra. This was done according to equation 1.17 by setting $I_0 = 1$, effectively defining the absorbance as the negative logarithm of intensity.

4.4.2: Photodarkening UV/Visible measurements

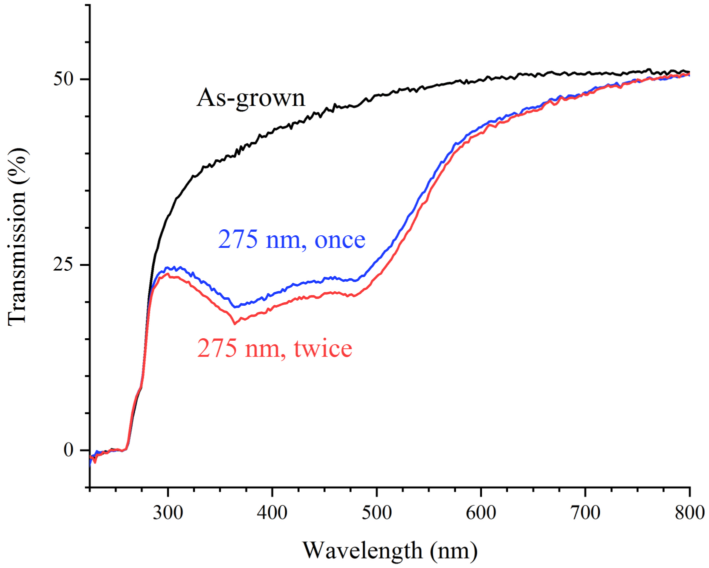

Figure 4.15. UV/Visible transmission spectra of β-Ga_2O_3:Cu in the as-grown and photo-darkened states. The sample was darkened two times in a row (labeled once and twice, respectively) to measure how sensitive the samples were to LED exposure as a function of time.

As shown in figure 4.15, a UV/Visible spectrum was collected of the crystal in the as-grown state (figure 4.15, as-grown). Then the crystal was darkened by exposing it to light from a 275 nm LED for 30 seconds per side and a new spectrum was acquired (labeled as 275 nm, once in figure 4.15). Without further treatment, the sample was immediately subjected to the same darkening procedure a second time (labeled 275 nm, twice in figure 4.15) to test the amount of time required to fully darken the samples. Transmission decreased by a few more percentage points at the minima, but 30 seconds per side (a total of 60 seconds) was deemed adequate for darkening experiments. Unless otherwise specified, this scheme (275 nm LED exposure for 30s per side) was used to darken the samples.

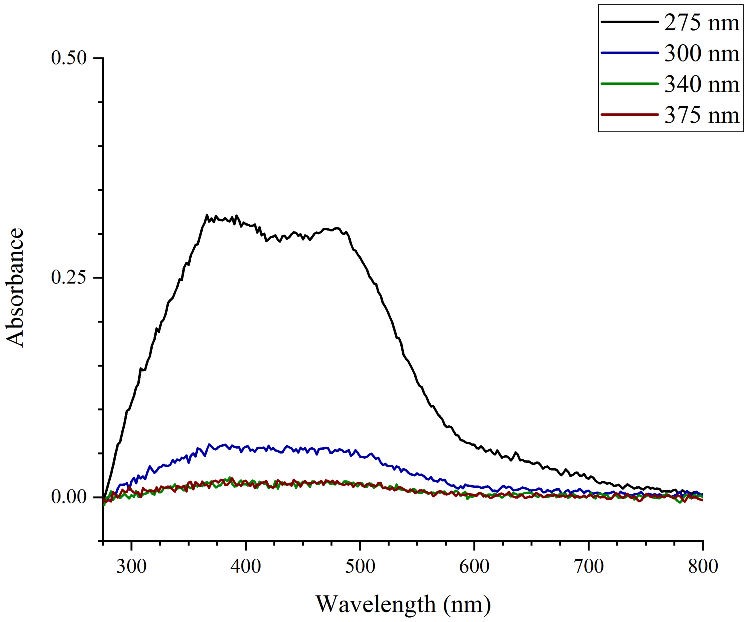

Figure 4.16. UV/Visible absorbance spectra of β-Ga_2O_3:Cu after exposure to a series of UV LEDs. Each spectrum was obtained with a separate sample (375 and 275 nm spectra share a common sample that was thoroughly erased between experimental runs), and the reference spectrum for each was an undarkened transmission spectrum. These data were published in Jesenovec *et al.*[48]

Jani Jesenovec determined that 275 nm light was sufficient to darken samples, but a lower bound to the threshold was not known. In order to determine the threshold wavelength, 375, 340, and 300 nm LEDs were used to illuminate separate samples, and absorbances were computed using transmission spectra according to equation 1.17. The as-grown transmission spectrum of each sample was used as the reference against the sample's darkened states. The results are presented in figure 4.16. The 375 and 340 nm LEDs did not darken the samples, and the 300 nm LED darkened the sample somewhat. The 275 nm LED had the greatest effect. This experiment was performed completely in the dark to reduce the impact of extraneous light, though the results indicate that interior lighting would not have altered the outcome. The 375 and 275 nm spectra utilized the same sample. The 375 nm experiment was carried out first, since that LED was expected to have little or no photodarkening effect. This sample was then erased for a longer period (~30 minutes) to eliminate any traces of photodarkening prior to performing the 275 nm exposure experiment.

Wavelength (nm)	**Voltage (V)**	**Current (mA)**	**Optical Power (mW) at 250 mA**	**Photon Energy (eV)**
375	3.2	250	87.3	3.3
340	4.3	250	17.0	3.6
300	5.9	250	0.505	4.1
275	12.1	250	0.532	4.5

Table 4.4. Measured optical power of the LEDs used for the experiment in figure 4.15.

In order to check that the photodarkening was truly dependent on photon energy, the power output of the LEDs was checked using a ThorLabs optical power meter (table 4.4). The LEDs were operated at the maximum working current of the 275 nm LED (250 mA). The LED with the highest power (375 nm, 87.3 mW) had no measurable effect on darkening the samples, and the two LEDs that measurably darkened the samples (300, 275 nm) had similar optical power outputs (within ~5% of each other). Given the drastic difference in the visible absorbance, it is safe to attribute the photodarkening effect to the energy of the photons coming from the LEDs, not the total optical power.

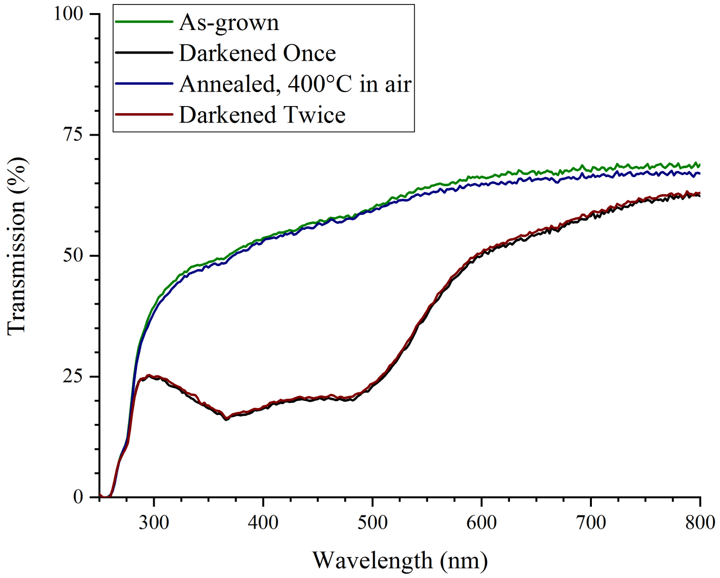

Figure 4.17. UV/Visible transmission spectra of β-Ga_2O_3:Cu that was darkened, erased, and darkened a second time.

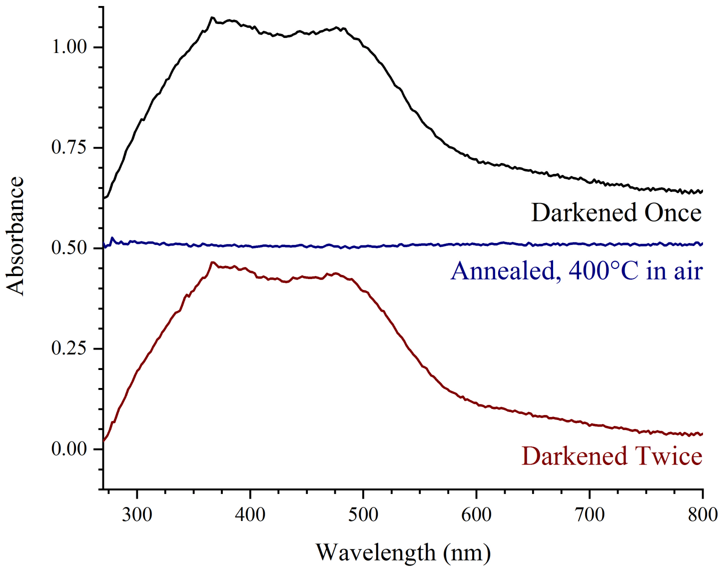

Figure 4.18. UV/Visible absorbance spectra of β-Ga_2O_3:Cu that was darkened, erased, and darkened a second time. The reference for the absorbances was the as-grown transmission spectrum (figure 4.17, green). The spectra have been offset for clarity.

The repeatability and quality of erasing the photodarkened samples was checked by repeatedly darkening and erasing a sample and taking UV/Vis spectra at each step (figure 4.17). A UV/Vis spectrum of an as-grown sample was taken, then the sample was darkened using the 275 nm LED and a new spectrum was taken. The sample was erased by annealing on a hot plate at 400ºC in air for 5 minutes, then the process was repeated. The absorbance calculated using the as-grown and annealed spectra is a flat line, indicating the 5 minute anneal completely erased the photodarkening (figure 4.18, blue). The second darkening was a near-perfect duplicate of the first as well. The photodarkening and erasing effects were shown to be complete and repeatable over the course of the experiments performed.

4.4.3: Photodarkening infrared results

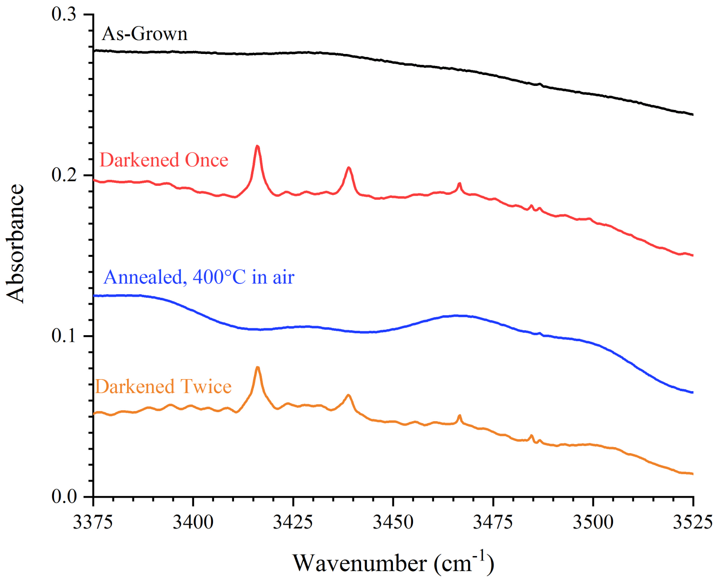

Figure 4.19. Low-temperature IR absorption spectra of the O-H modes in β-Ga_2O_3:Cu in a series of darkened and erased states. The reference for all spectra was a constant. These data were published in Jesenovec *et al.*[48]

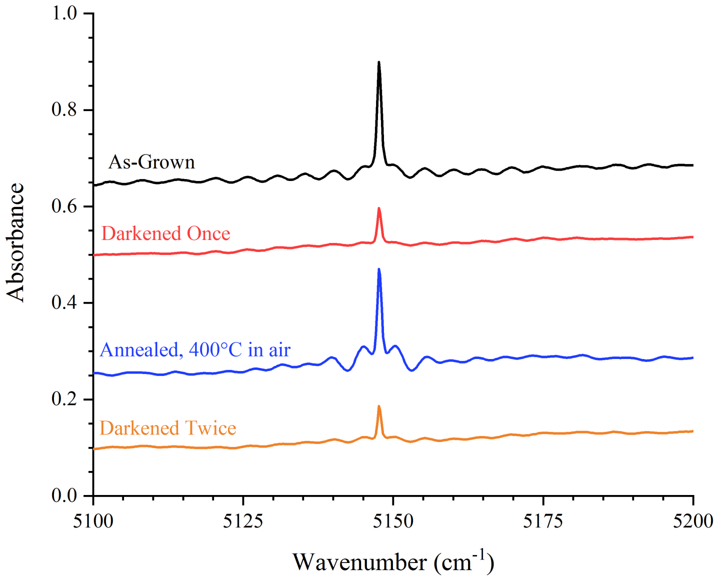

Figure 4.20. Low-temperature IR absorption spectra of the Ir^{4+} peak β-Ga_2O_3:Cu in a series of darkened and erased states. The reference for all spectra was a constant. The sinusoidal fringes are the result of the layer delamination described in section 4.4.1 (figure 4.14). These data were published in Jesenovec *et al*.[48]

In the as-grown state, no O-H modes are visible (figure 4.19, black spectrum), but the isolated Ir^{4+} peak at 5147.6 cm^{-1} is prominent (figure 4.20, black spectrum). Following exposure to a 275 nm LED for a short period of time (~60 seconds), the Ir^{4+} peak is decreased (figure 4.20, red spectrum) and O-H modes become visible as absorbance peaks at 3416.1, 3438.9, 3466.6, and 3484.6 cm^{-1} (figure 4.19, red spectrum). These peaks are attributed to CuH complexes. A small peak at 3487.6 cm^{-1} is also observed, but this is present in all spectra regardless of darkening and is attributed to Zn impurities in the Cu_2O powder used for the growth (see section 4.3.2).[30] Aside from the five O-H modes and the Ir^{4+} (oct) peak, no other peaks were observed.

EPR results indicate a charge state change from Cu^{2+} to Cu^{3+} occurs when the samples are photodarkened.[64] As a result, Jesenovec *et al.* propose the following two-step process for photodarkening:[48]

$$(\mathrm{Cu}_{\mathrm{Ga(II)}} - \mathrm{H}_{\mathrm{O(I)}})^0 \rightarrow (\mathrm{Cu}_{\mathrm{Ga(II)}} - \mathrm{H}_{\mathrm{O(I)}})^+ + e^- \qquad (4.1)$$

$$(\mathrm{Cu}_{\mathrm{Ga(II)}} - \mathrm{H}_{\mathrm{O(I)}})^+ \rightarrow (\mathrm{Cu}_{\mathrm{Ga(II)}} - V_{\mathrm{O}} - \mathrm{H}_i)^+ \qquad (4.2)$$

In equation 4.1, the proposed $Cu_{Ga(II)}$-$H_{O(I)}$ complex would be IR-inactive "hidden hydrogen"[62], consistent with the absence of CuH modes in the as-grown state. The calculated threshold energy required to photoexcite an electron from this complex to the conduction band is 3.82 eV (~325 nm), consistent with the results in figure 4.16. Once the $Cu_{Ga(II)}$-$H_{O(I)}$ is ionized, both the proton and electron become mobile. If the electron becomes trapped by an Ir^{4+} atom, the 5147.6 cm^{-1} peak will be decreased, as observed in figure 4.20. The mobile proton is also free to form new complexes, such as the CuH seen in figure 4.19.

4.4.4: Photodarkening time relaxation

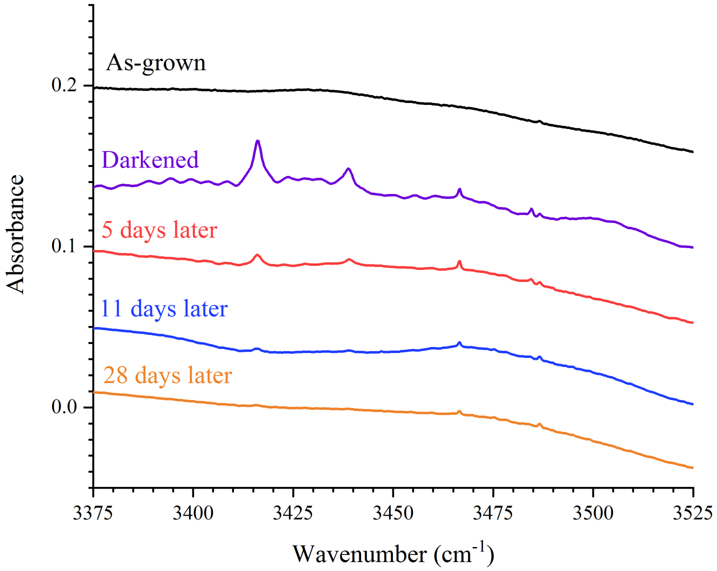

Figure 4.21. Low-temperature IR absorption spectra of the O-H modes in β-Ga_2O_3:Cu beginning in the as-grown state and progressing in time to 28 days after the initial darkening. The reference was a constant

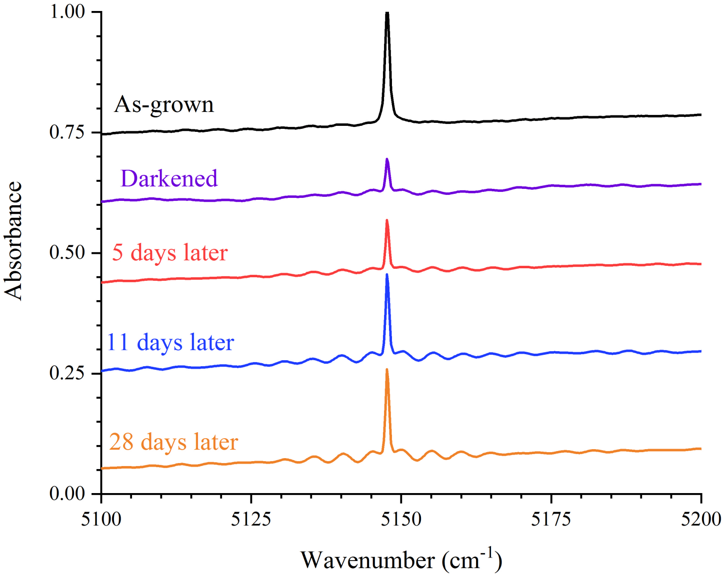

Figure 4.22. Low-temperature IR absorption spectra of the Ir^{4+} β-Ga_2O_3:Cu beginning in the as-grown state and progressing in time to 28 days after the initial darkening. The reference was a constant

Figure 4.23. Image of the sample that was allowed to lighten naturally (upper left) and a sample that had not yet been darkened (bottom). This image was taken immediately prior to obtaining the "28 days later" spectra from figure 4.19. The sample appears to still maintain some of the darkened coloration.

A sample was darkened and allowed to lighten naturally over the course of ~1 month. IR spectra were collected periodically to monitor the CuH and Ir^{4+} peak heights. The CuH peaks gradually disappeared while the Ir^{4+} peak grew to its original height (figures 4.21, 4.22). The CuH peaks did not decrease uniformly, with the 3466.6 and 3484.6 cm^{-1} peaks persisting longer than the 3416.1 and 3438.9 cm^{-1} peaks. This may imply that not all of the observed O-H modes correspond to CuH or are not directly related to the photodarkening process. Particularly, since the 3416.1 and 3438.9 cm^{-1}

peaks have vanished while the sample is still somewhat dark (figure 4.23), they may correspond to a process parallel to the photodarkening.

4.4.5: Polarized infrared measurements

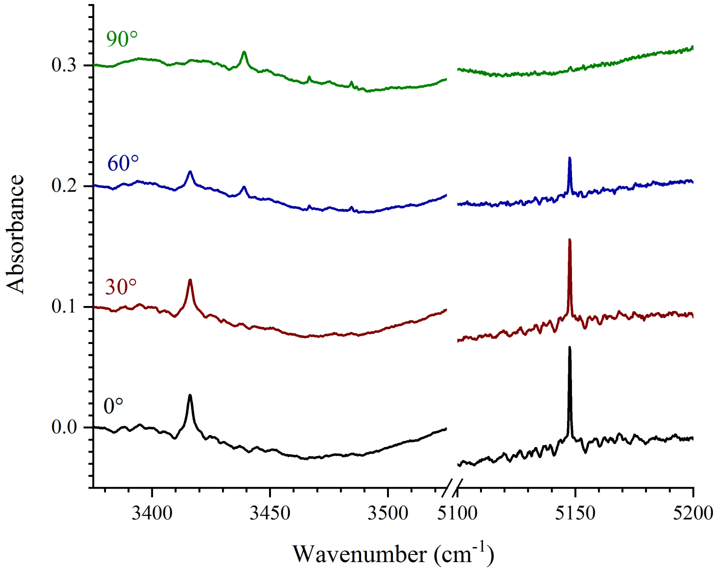

Figure 4.24. Low-temperature polarized IR absorption spectra of β-Ga_2O_3:Cu. The reference was a constant. The angles listed are with respect to the **b**-axis.

Polarization behavior was checked by inserting a ThorLabs wire grid linear polarizer into the beam path in front of the sample (4.24). The 3416.1 cm^{-1} peak displays surprising behavior, tracking in intensity with the Ir^{4+} transition, which is maximized when **E**//**b**. This is the first O-H mode observed (confirmed in the following section) to lie in the *b*-*c* plane. The other three O-H modes behave as expected, and are maximized when **E**//**c**.[29,30]

4.4.6: Deuterium anneal

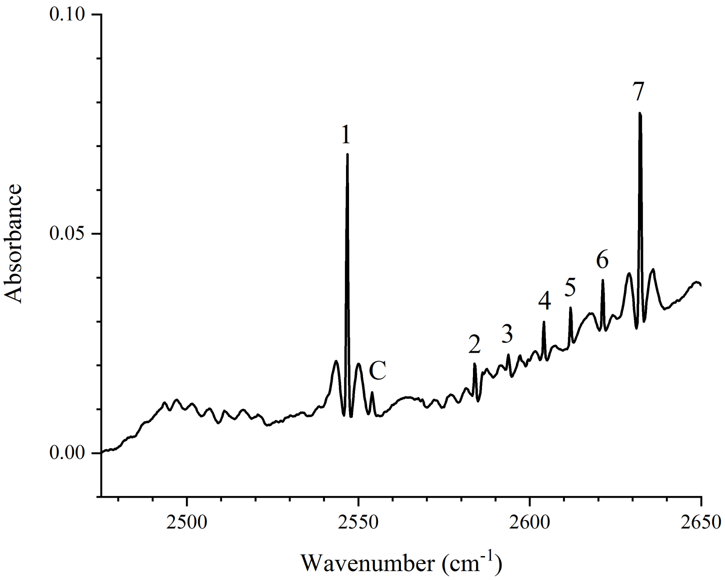

Figure 4.25. Low-temperature IR absorption spectrum of β-Ga_2O_3:Cu annealed in deuterium. The reference was a constant. The two "peaks" flanking the peaks labeled 1 and 7 are likely residual interference fringes.

Confirmation of the O-H mode assignments was carried out in the usual way.[29,30] A sample was sealed in a silica ampoule with 0.5 atm of D_2, then annealed at 860ºC for 3.5 hours. The result is shown in figure 4.25. Other than a small peak at 2554.1 cm^{-1}, the most prominent peaks are labeled 1-7 and were proposed to correspond to undetermined V_{Ga}-nD complexes by Qin *et al.*[62] Peaks labeled A-F were not reported in Qin *et al* (only C is visible in 4.25).

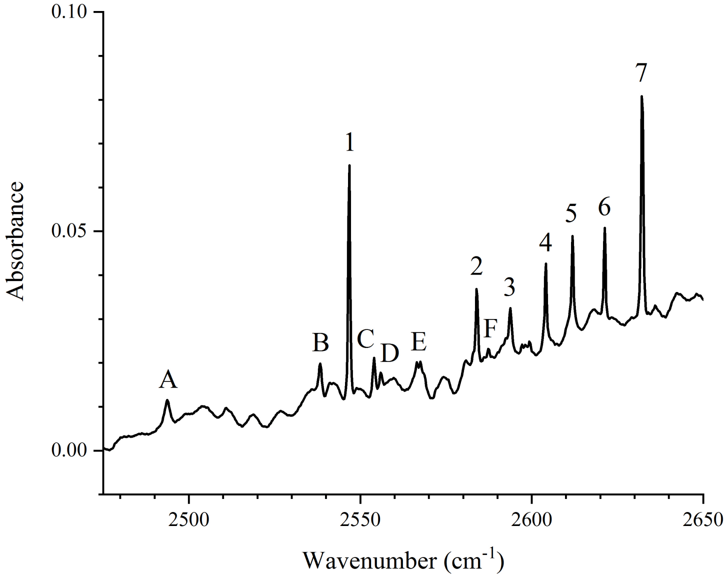

Figure 4.26. Low-temperature IR absorption spectrum of darkened, deuterium annealed β-Ga_2O_3:Cu. The reference was a constant.

Label (figures 4.20, 4.21)	Copper-doped, deuterated, darkened	Copper-doped, deuterated	Undoped, deuterated	Assignment or Corresponding O-H mode
A	2493.6			
B	2538.4			3416.1 (ratio 1.346)
1	2546.9	2546.9	2546.4	V_{Ga}-2D
C	2554.1	2554.1		3438.9 (ratio 1.346)
D	2556.0			
E	2566.5			3466.6 (ratio 1.351)
E	2567.6			3466.6 (ratio 1.350)
2	2584.2	2584.2	2583.7	V_{Ga}-nD *
F	2587.5			3484.6 (ratio 1.347)
3	2593.8	2593.8	2592.9	V_{Ga}-nD *
4	2604.0	2604.0	2603.1	V_{Ga}-nD *
5	2611.9	2611.9	2611.7	V_{Ga}-nD *
6	2621.4	2621.4	2620.1	V_{Ga}-nD *
7	2632.2	2632.2	2632.6	V_{Ga}-nD *

Table 4.5. List of peaks observed in deuterium annealed β-Ga_2O_3:Cu. Peak locations listed in the Undoped, deuterated column come from Qin *et al*.[62] Peaks 2-7 were not given firm assignments, but are thought to correspond to various V_{Ga}-D geometries.

The deuterated sample was photodarkened and a new FTIR spectrum was taken. New peaks were observed (figure 4.26) and listed in table 4.5. Peak assignments in common with Qin *et al*[62] do not match exactly, likely due to strain within the crystal lattice caused by the more defective nature of the crystals, but differences are restricted to a maximum of ~1 cm^{-1}. The measured isotopic frequency shift, if the peak assignments in table 4.5 are correct, also works out to be slightly less than expected at ~1.347 rather than ~1.35 as previously observed.[29,30] More peaks were observed than were originally present in the O-H region. Peaks A and D were not matched to an O-H mode. Peak E is used twice because there are two small, but resolvable, peaks close together. Peak C was also present prior to darkening, unlike its O-H analog.

4.4.7: Conclusions

Persistent photochromism was observed in β-Ga_2O_3:Cu. This photodarkening occurred upon exposure to 275 nm light and persisted for approximately 1 month. O-H modes attributed to CuH complexes appeared in the IR upon darkening, accompanied by a reduction in the intensity of the 5147.6 cm^{-1} Ir^{4+} electronic transition, signaling a reduction of the Ir atoms to the IR-inactive Ir^{3+} charge state. EPR also indicated that photodarkening was accompanied by oxidation of Cu^{2+} to Cu^{3+}. It is proposed that photoionization of an IR-inactive $Cu_{Ga(II)}$-$H_{O(I)}$ complex promotes an electron to the conduction band and causes the proton to dissociate. The IR results are explained by Ir^{4+} capture of the free electron and the mobile proton forming a new IR-active CuH complex.

4.5: Future work

A few of the peaks that have been observed still need to be assigned to a defect. The 3545 cm^{-1} peak is likely an acceptor-H complex, but its appearance is not consistent. More than likely, it will be determined when a growth with the acceptor is performed. A dedicated H_2 anneal was never performed on the Cu-doped growth in case the process eliminated the samples' ability to photodarken. Performing H_2 and D_2 anneals should on CZ crystals from this growth could shed light on the nature of the CuH peaks as well as the additional unidentified peaks observed in the photodarkened, deuterated experiments. More work regarding the structure related to the 3416.1 cm^{-1} peak is needed in particular, since its behavior under polarized FTIR was unexpected.

There are also a large number of potential defects that remain to be studied. Work is actively being done on Al and Ni. Several doping and alloying ratios are being investigated with Al to examine the similarities between β-Ga_2O_3 and Al_2O_3. Ni may also display photodarkening properties, which could confirm the proposed models for β-Ga_2O_3:Cu presented in this work.

CHAPTER FIVE: PERSISTENT PHOTOCONDUCTIVITY IN BARIUM TITANATE

This paper is the result of the work presented in this chapter:

- Persistent photoconductivity in barium titanate
  C. Pansegrau and M.D. McCluskey, Journal of Applied Physics **131**, 095701 (2022).

Section 5.1 is a complete reproduction of the above journal article. Section 5.2 presents supplementary information submitted with the main article.

5.1: Persistent photoconductivity in barium titanate

Christopher Pansegrau*, Matthew D. McCluskey*

**Department of Physics and Astronomy, Washington State University, Pullman, Washington 99164-2814, USA*

5.1.1: Abstract

Annealed bulk crystals of barium titantate ($BaTiO_3$) exhibit persistent photoconductivity (PPC) at room temperature. Samples were annealed in a flowing gas of humid argon and hydrogen, with a higher flow rate corresponding to larger PPC. When exposed to sub-bandgap light, a broad infrared (IR) absorption peak appears at 5000 cm^{-1} (2 μm), attributed to polaronic or free-carrier absorption from electrons in the conduction band. Along with the increased IR absorption, electrical resistance is reduced by a factor of approximately two. The threshold photon energy for PPC is 2.9 eV, similar to the case of $SrTiO_3$. This similarity suggests that the mechanisms are similar: an electron in substitutional hydrogen (H_O) is photoexcited into the conduction band, causing the proton to leave the oxygen vacancy and attach to a host oxygen atom. The barrier to recover to the ground state is large such that PPC persists at room temperature.

5.1.2: Introduction

After annealing in a hydrogen-containing atmosphere, strontium titanate ($SrTiO_3$, STO) exhibits large persistent photoconductivity (PPC) at room temperature.[40,65,66] PPC is characterized by dramatic increase, up to several orders of magnitude, in electrical conductivity that can last for weeks or longer.[65] Infrared (IR) measurements show an accompanying increase in free carrier absorption.[65] Poole *et al.*[66] showed it is possible to selectively induce PPC in defined areas of a crystal, creating the possibility for rewritable optically-written circuitry, holographic data storage,[67,68] and other applications in photolithography. The proposed mechanism behind PPC involves the electronic excitation of substitutional hydrogen (H_O).[69,70] An electron in H_O is photoexcited into the conduction band, causing the proton to leave the oxygen vacancy and attach to a host oxygen atom. The barrier to recover to the ground state is large such that the effect persists at room temperature.

To our knowledge, this effect has only been reported in STO. To address whether room-temperature PPC may exist in other semiconductors, we performed experiments on barium titanate ($BaTiO_3$, BTO), a promising candidate for PPC due to its chemical and structural similarity to STO. Like STO, the oxygen vacancy in BTO is predicted to be a shallow double donor.[70,71] BTO is a transparent perovskite oxide semiconductor with a band gap of 3.22 eV[36] and applications in transducers, capacitors,[72] and nonlinear optics. It has both ferroelectric and piezoelectric properties that arise from discplacement of the titanium atom along the c axis in the tetragonal cell, with a Curie temperature of 120ºC.[35,73]

In the present work, changes in charge carrier density were measured via IR absorption. Prior work on BTO has shown that carriers result in a broad IR peak around 2 μm (~0.6 eV, or 5000 cm^{-1}).[74] This has been attributed to a superposition of electronic excitations from impurity states 0.2-0.3 eV below the conduction-band minimum and free carrier absorption; however, the proposed defect has not been identified.[39,74–76] Although small polaron models of charge transport in oxide perovskites are frequently invoked, electrical measurements indicate mobilities that are higher than those predicted by purely polaronic models.[77–80] Regardless of the exact physical model, an increased absorption in the mid-IR enables a nondestructive measure of changes in charge-carrier density.[40] For the purposes of this work, we refer to the charge carriers as free electrons.

5.1.3: Experimental methods

Single crystal BTO substrates, grown via the top-seeded solution method, 10×10×0.5 mm, (100) oriented with 1 side polished, were obtained from MTI. The samples had multiple visible ferroelectric domains present (i.e., they were not single-domain crystals). The ferroelectric domains were not observed to change throughout the experiments (see sections 5.2.2 and 5.2.3). Samples were annealed in a horizontal tube furnace under a flowing gas mixture of humid argon and a 2% hydrogen, 98% argon mixture. Humid argon was produced by bubbling ultra-high purity argon through high-performance liquid chromatography (HPLC) grade water. The two gas sources were combined after the bubbler and the relative humidity was recorded during the annealing process.

Samples were sealed in the furnace and gas flow was established for a minimum of 0.5 hr prior to powering the furnace. Two gas flow values were used for the hydrogen-argon mixture, 1.0 and 4.0 standard cubic feet per hour (scf/h). The flow of humid argon in each case was adjusted during the annealing process to achieve a combined relative humidity of 40%, which resulted in an average flow of 1.0 and 3.0 scf/h, respectively. At the end of the purge process, the furnace was powered on and the sample annealed for 1 hr at 1200°C with a temperature ramp rate of 550°C/h. Upon completion of the anneal, the entire gas tube assembly was moved so that the portion containing the sample was outside of the furnace for a rapid cool-down. The gas flow was maintained for 1 h after the anneals were finished.

IR spectra were collected using a Bomem DA8 Fourier transform infrared (FTIR) spectrometer. Spectra were taken at ambient temperature with a SiC source, InSb detector, and CaF_2 beamsplitter. A light emitting diode (LED) was placed in the sample chamber so that the samples could be illuminated during spectrum acquisition. Spectra were collected in an alternating pattern with the LED on or off, with LEDs used in order of increasing photon energy (red to violet). Light intensity from the LEDs was regulated by fixing the current supplied at 800 mA for all LEDs used. Absorbance spectra were computed as

$$\text{Absorbance} = \log_{10}(I_0/I),$$

where I_0 is first transmission spectrum of the series, taken with the LED off, as the reference. LEDs with various photon energies were used up to a maximum of 3.06 eV. Two-point electrical measurements were performed using pressed indium contacts and a Fluke 117 digital multimeter.

5.1.4: Results

In the following sections, IR and electrical measurements are discussed. Sections 5.1.4.a and 5.1.4.b present results from the two hydrogen-argon flow rates. We denote the rates as low (1 scf/h) and high (4 scf/h). Untreated samples did not show PPC (see section 5.2.1). These sections are followed by results from experiments that measured the persistence of the enhanced conductivity.

5.1.4.a: Low hydrogen-argon flow rate

LEDs ranging from 1.98 to 3.06 eV (625-405 nm) were used in sequence, separated by spectra taken in the dark. The “dark” spectra were baselined against the initial spectrum acquired prior to any light exposure to compute the absorbance spectra seen in figure 5.1. Light with energy below 2.92 eV did not have a marked effect, as absorbance across all wavenumbers is at or near zero. Shining light of energy 2.92 and 3.06 eV, however, caused a broad and significant absorbance increase centered near 5000 cm^{-1}. We attribute this effect to an increase in free-carrier density caused by exposure to photons of energy >2.9 eV. From the published absorbance and carrier density data (Last[73]), we estimate electron concentrations of 1.0×10^{18} and 1.2×10^{18} cm^{-3} for the annealed and light-exposed states, respectively.

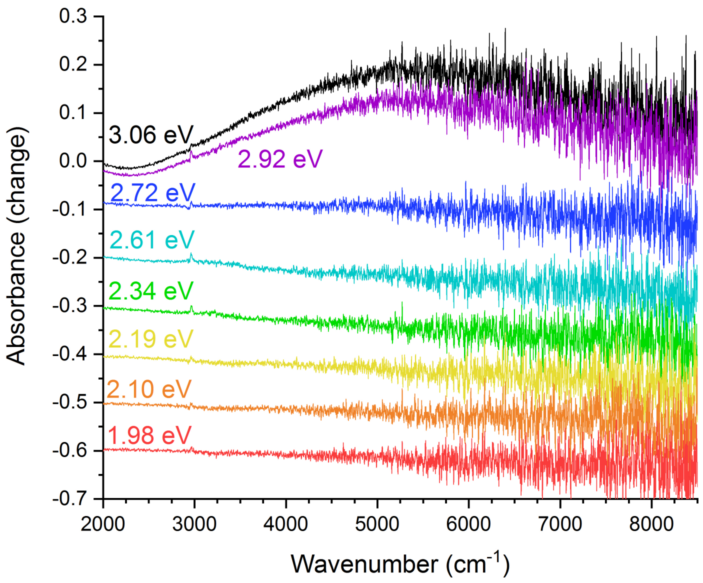

Figure 5.1. Room temperature absorbance spectra of a sample annealed in 1 scf/h 2% H_2, taken in order of increasing energy. The baseline used was the first spectrum taken after annealing, before exposure to light (not shown). This experiment was performed over several days, and some baseline drift occurred for the 2.61 and 2.72 eV spectra. Spectra labeled 1.98 eV through 2.61 eV were shifted vertically downward for clarity.

5.1.4.b: High hydrogen-argon flow rate

As with the previous experiment (section 5.1.4.a), LEDs up to 3.06 eV were used in order of increasing energy and absorbances were calculated using a baseline spectrum acquired prior to any light exposure. The 2.72 eV LED (section 5.1.4.a) was substituted by a 2.80 eV LED in this experiment, and a very low-level increase in absorbance over the base-level pattern can be seen (figure 5.2). Thus, 2.80 eV appears to be on the very edge of the threshold of this phenomenon. Compared to the low flow rate experiment, the total change in absorbance introduced by exposure to light is approximately three times larger at the peak. Estimated carrier densities[73] were 2.2×10^{18} and 2.8×10^{18} cm^{-3} for the annealed and light-exposed states, respectively. This is consistent with a higher concentration of H_O introduced by the higher hydrogen-argon flow rate.

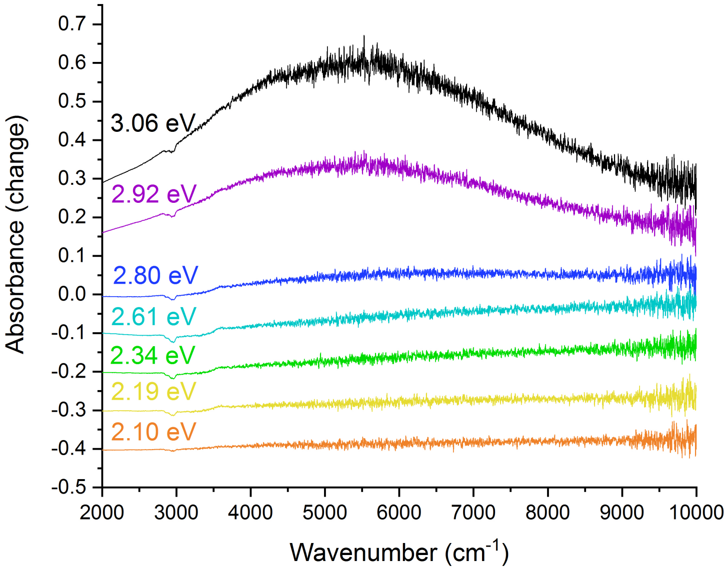

Figure 5.2. Room temperature absorbance spectra of a sample annealed in 4 scf/h 2% H_2, taken in order of increasing energy. The baseline used was the first spectrum taken after annealing, before exposure to light (not shown). Spectra labeled 2.10 eV through 2.61 eV were shifted vertically downward for clarity

5.1.4.c: Persistence measurements

To test the persistence of the increased IR absorption, a sample was annealed with a high hydrogen-argon flow rate (4 scf/h). The sample was exposed to 3.06 eV light and monitored over a period of three days. During that time the sample was kept in the spectrometer and was shielded from visible/UV light. As with the prior experiments (sections 5.1.4.a and 5.1.4.b), these spectra were baselined against the first spectrum taken prior to any light exposure. As shown in figure 5.3, the induced IR absorption is very persistent. In the initial 48-h period, slight decreases in the absorbance peak were observed, with little to no further change at later times.

Two-point electrical measurements were performed simultaneously with the post-exposure lifetime experiment. The initial resistance, prior to light exposure, was measured to be 5200 Ω. Following exposure to 3.06 eV light, the measured resistance dropped to 2975 Ω. This value rose to 3050 Ω in the following 24 hours and did not change further at later times (figure 5.4, points 3-5).

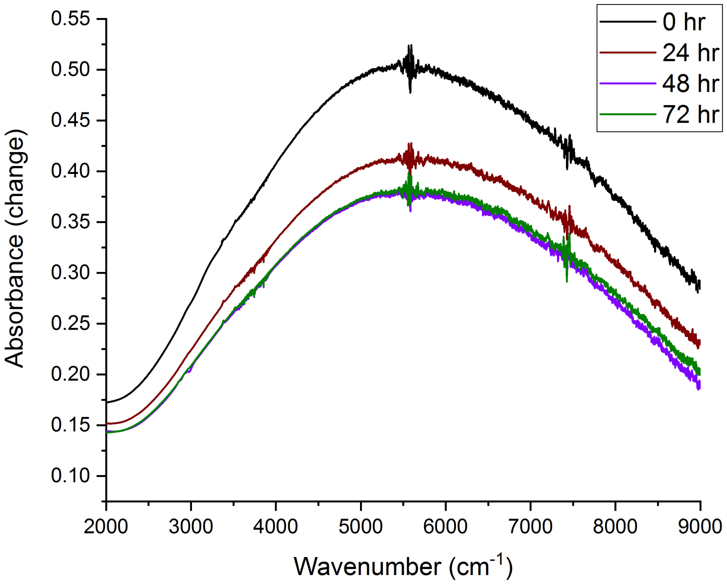

Figure 5.3. Absorbance spectra of a sample after exposure to 3.06 eV light. The sample was kept in the IR spectrometer during the measurements, which protected it from visible/UV light. Features near 5500 and 7500 cm^{-1} are experimental artifacts.

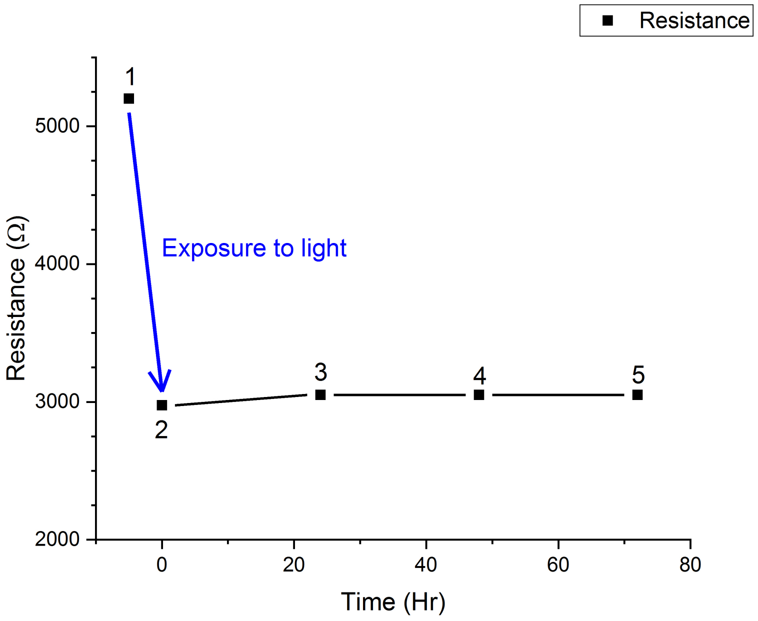

Figure 5.4. Electrical measurements for the sample shown in figure 5.3. Point 1 shows the resistance as-annealed. Point 2 shows the resistance following exposure to a 3.06 eV LED. The resistance increased a little bit in the following 24 hours (point 3) but did not change further (points 4 and 5).

5.1.5: Discussion

Our experimental results show that BTO annealed in a hydrogen-containing atmosphere exhibits PPC at room temperature, as predicted by the theoretical work of Zhang and Janotti.[70] Earlier calculations indicated that hydrogen can occupy a substitutional oxygen site and the oxygen vacancy is a shallow double donor.[81,82] These conditions are required for the type of PPC observed here, where photons cause hydrogen to leave an oxygen vacancy. Since the oxygen vacancy is a shallow donor, it contributes electrons to the conduction band, resulting in enhanced conductivity. In principle, any semiconductor for which oxygen vacancies are shallow donors could show PPC.

The proposed model for PPC in STO is that upon exposure to light hydrogen occupying an oxygen vacancy moves to an interstitial site near a Sr vacancy.[69,70] We propose the same mechanism is at work in BTO (substituting Ba for Sr). The magnitude of PPC depends strongly on the hydrogen-argon flow rate, consistent with the role of hydrogen in this process. The samples analyzed here were too absorbing to observe hydrogen-related peaks[83] in the annealed state. However, thinner samples may be suitable for such a study. In addition, attempts were made to erase PPC by annealing an exposed sample in air at 200-300ºC. Unlike STO, the absorbance did not follow a clear trend with annealing temperature and the annealed sample did not exhibit PPC. This behavior may be due to the ferroelectric properties of BTO as compared to paraelectric STO.

The optical and electrical behavior matches generally with observations of PPC in STO. The effect observed here is less dramatic, only a factor of 2 reduction in electrical resistance and a total change of ~0.6 in absorbance as opposed to STO, which shows several orders of magnitude change in electrical resistance and several absorbance units.[40,65,66,84] This could be due in part to the lower starting resistance observed in BTO. STO samples began in the MΩ region and were reduced to kΩ whereas the BTO samples generated here began in the kΩ range. However, two-point measurements are affected by contact resistance, which in STO was found to be significant.[66] With a well-optimized annealing scheme for BTO, an initially more resistive sample could be prepared and larger changes should be observed. Such a scheme could include additional steps (such as treatment in oxygen for increased resistivity) or additional gas components in the flowing mixture.

5.1.6: Conclusions

In conclusion, BTO annealed at 1200°C under a flowing humid hydrogen atmosphere exhibits PPC at room temperature upon exposure to 2.9 eV photons. This optical threshold is in agreement with the 2.9 eV ionization energy of $\mathrm{H}_{\mathrm{O}}^{+}$ predicted by Zhang and Janotti.[70] IR absorption due to electrons in the conduction band increases and persists for several days or more. Electrical resistance decreased by a factor or two, a change that was not observed to relax within the timeframe of the experiment. The observed phenomena depend strongly on hydrogen in the annealing environment, suggesting that the PPC mechanism is similar to that of STO. In the future, combining PPC with BTO's ferroelectricity and piezoelectricity could yield novel devices.

5.2: Supplementary material

5.2.1: Control experiment

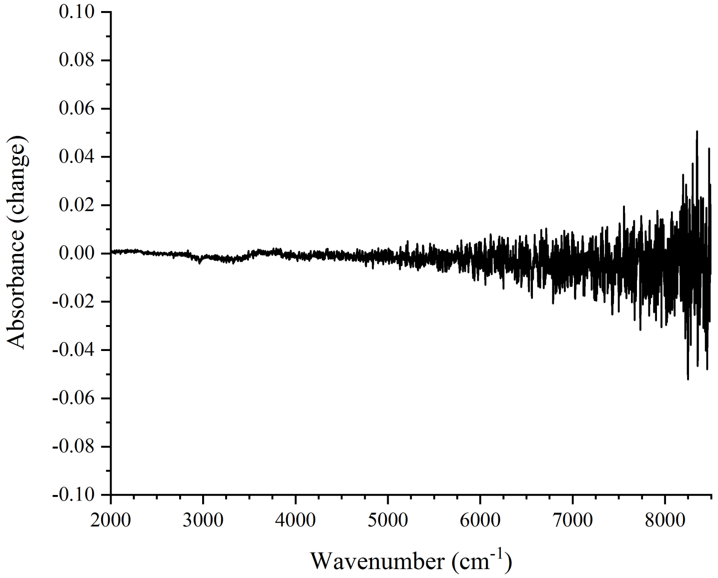

Figure 5.5. IR absorbance spectrum of a control experiment. Spectra were taken of the sample prior to any light exposure and following illumination with a 3.06 eV (405 nm) LED. No PPC was observed in the untreated sample.

A control experiment was performed using an as-received sample. IR spectra were collected of the sample before, during, and following illumination using a 3.06 eV (405 nm) LED. The spectra collected before and following the illumination were used to calculate the absorbance spectrum presented in figure 5.5 using the spectrum collected before light exposure as the reference. No indication of PPC was found.

5.2.2: Low hydrogen-argon flow rate supplement

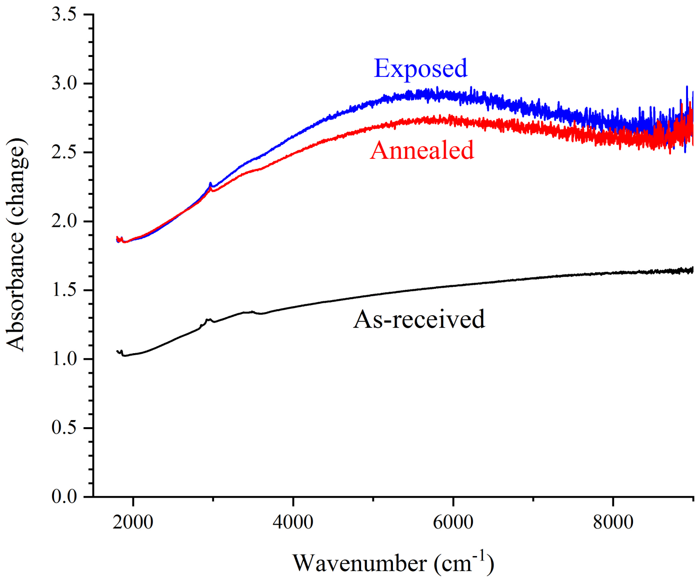

Figure 5.6. IR absorbance spectra of the sample prepared in 1 scf/h of flowing gas. The reference for the absorbance calculations was a blank. Spectra were collected of the sample as-received (black), freshly annealed (red), and annealed and light-exposed (blue). Annealing introduces a strong uniform absorbance to the sample. Light exposure causes an absorbance increase in the mid-IR.

Figure 5.7. Image of the sample prepared in 1 scf/h of flowing gas in the as-received state. The ferroelectric domains are visible as the darker stripes running vertically in the image. The sample will break along the crack at the top of the image following the anneal process.

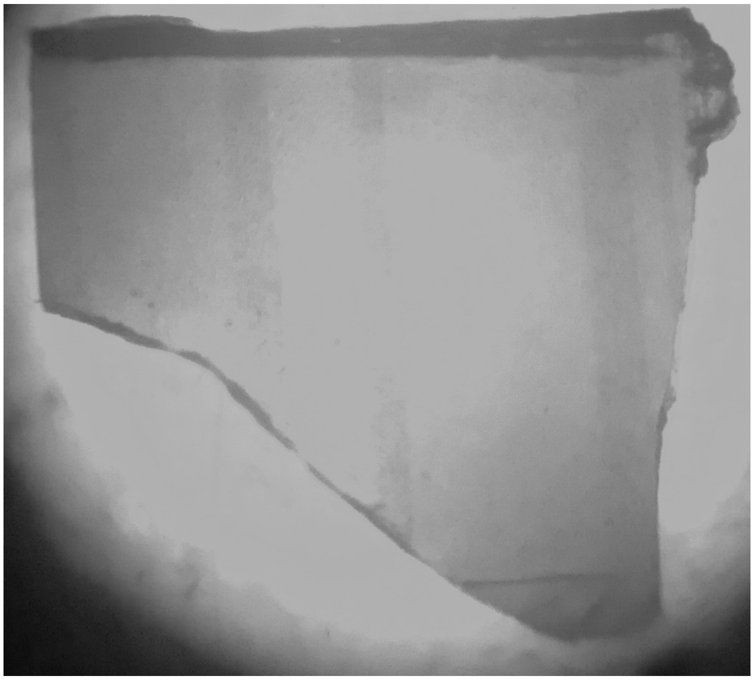

Figure 5.8. Image of the sample prepared in 1 scf/h of flowing gas in the annealed state.

Figure 5.9. Image of the sample prepared in 1 scf/h of flowing gas in the exposed state.

The domains appear to have not changed throughout the experiment.

5.2.3: High hydrogen-argon flow rate supplement

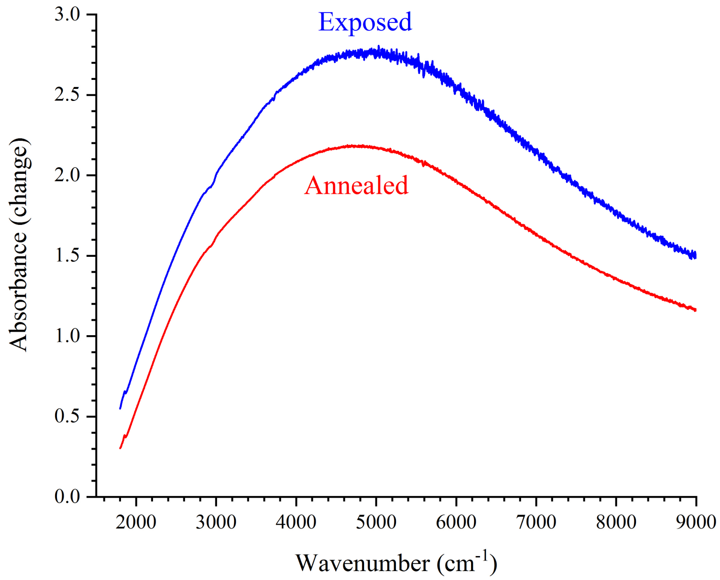

Figure 5.10. IR spectra of the sample prepared in 4 scf/h of flowing gas. The baseline used was a blank. The spectra presented are the annealed and annealed and exposed states. Light exposure adds an absorbance in the mid-IR.

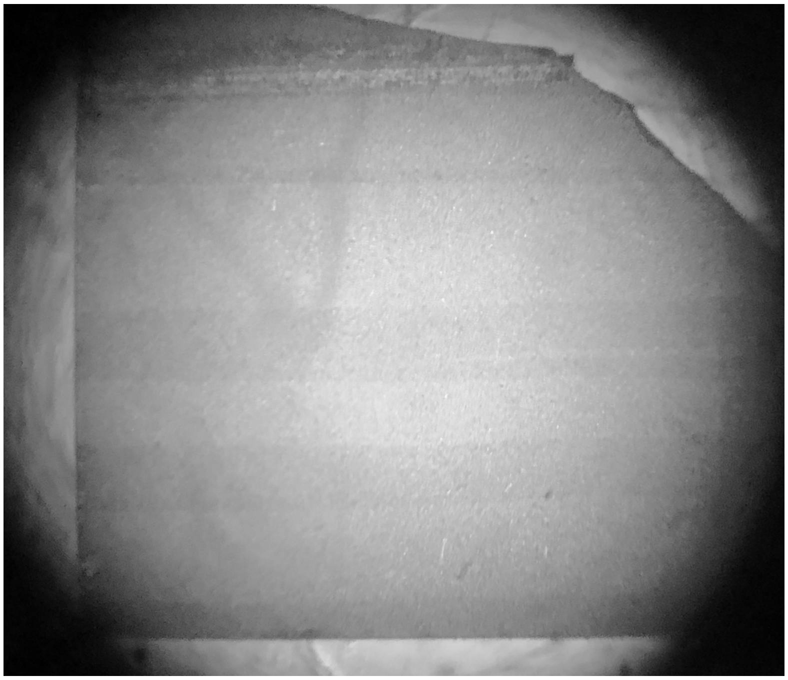

Figure 5.11. Image of the sample prepared in 4 scf/h of flowing gas, taken following the anneal. The ferroelectric domains are visible as darker horizontal stripes.

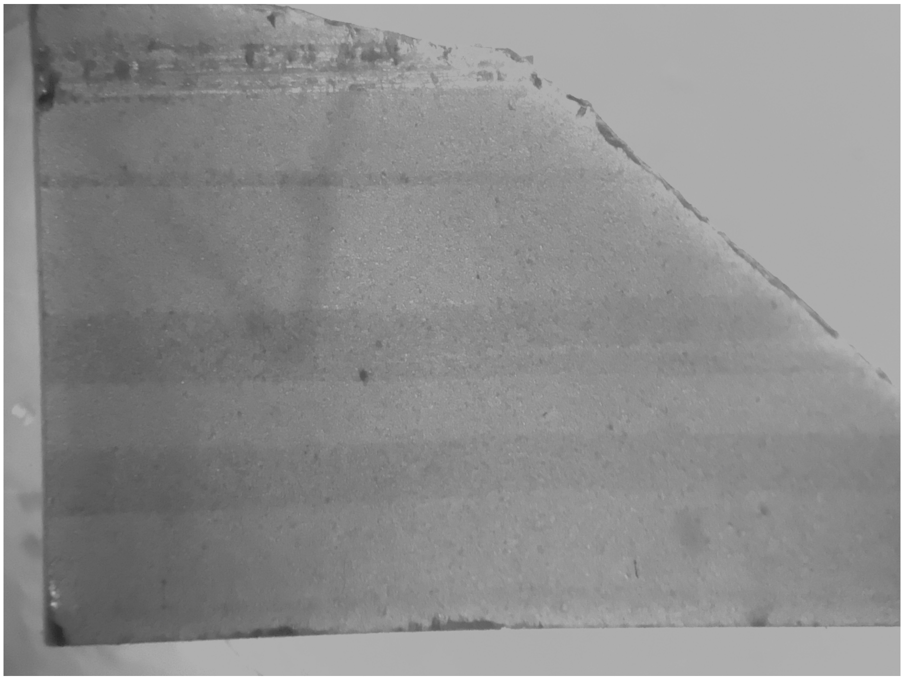

Figure 5.12. Image of the sample prepared in 4 scf/h of flowing gas, taken following exposure to light. The domains did not appear to change throughout the experiment.

CHAPTER SIX: AS-RECEIVED $SrTiO_3$ and $BaTiO_3$

Results presented in this chapter are the result of early experiments that explored the behavior of $SrTiO_3$ and $BaTiO_3$ at low temperature when exposed to light from a series of LEDs.

6.1: Low-temperature light exposure of $SrTiO_3$

Single crystal $SrTiO_3$ samples, 10×10×0.5 mm, (100) oriented with 1 side polished, were obtained from MTI. Infrared measurements were performed using a Bomem DA8 Fourier transform infrared (FTIR) spectrometer equipped with a SiC source, CaF_2 beamsplitter, and InSb detector. Infrared spectra were collected at low temperature (~10-11.5 K) using a Janis closed-cycle helium cryostat. Samples were initially mounted so that light was incident perpendicular to the (100) surface, then rotated 45° so that both the IR beam and light from an external LED could impinge on the sample surface. Spectra were taken in an alternating pattern with the external LED on and off. LEDs were used in order of increasing photon energy (red to violet).

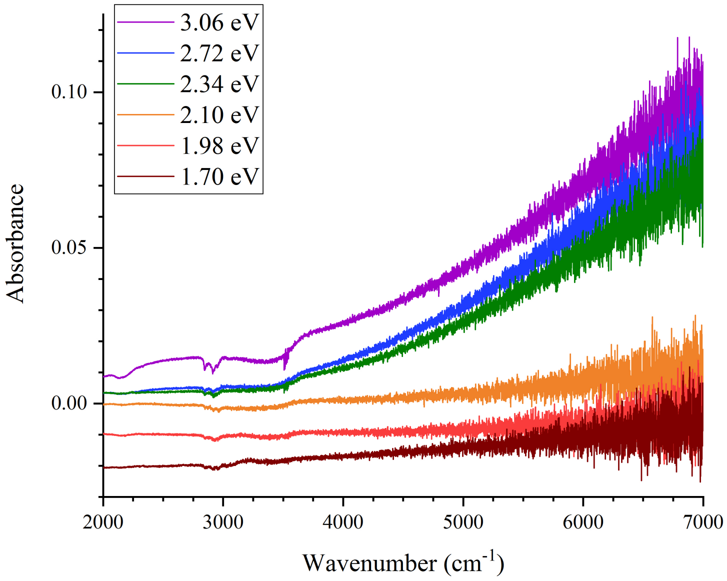

Figure 6.1. Low-temperature IR absorption spectra of $SrTiO_3$ exposed to LEDs with the listed energies. The reference for each spectrum was the preceding spectrum taken in the dark. The 1.70 and 1.98 eV spectra were shifted vertically downward for clarity.

Light with energy greater than 2.3 eV introduces a broad absorption feature extending out to the large wavenumbers (figure 6.1). Based on results in chapter 5 and section 6.2, it is conceivable this feature would turn around to form a broad peak if given sufficient measurement range. This measurement is limited by low signal starting with ~6000 cm^{-1}. Features are also visible from 2800-3000 and ~3500 cm^{-1}. The region 2800-3000 cm^{-1} is populated with complex organic molecules. This feature is systematic and not part of this experiment. The features near 3500 cm^{-1} will be examined shortly and have been attributed to O-H stretching modes by Houde *et al.*[85]

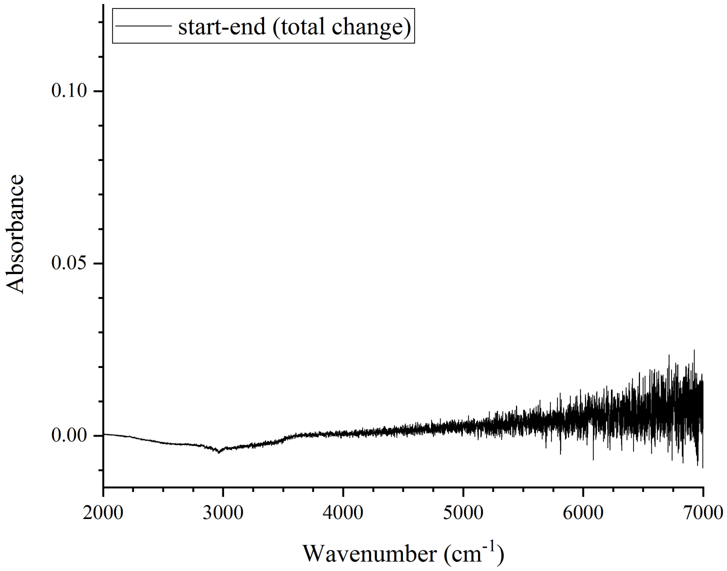

Figure 6.2. Low-temperature IR absorption spectrum of $SrTiO_3$. This spectrum was computed using the final spectrum taken in the dark (after exposure to the 3.06 eV LED) and the first spectrum (prior to any light exposure) as the reference. No indication of persistence is present.

In order to check for persistence, the first and last spectra of the series, taken with the external LED off, were compared as an absorbance using the first spectrum (prior to light exposure) as the reference (figure 6.2). No significant features are present in the spectrum, so no persistent effects can be claimed.

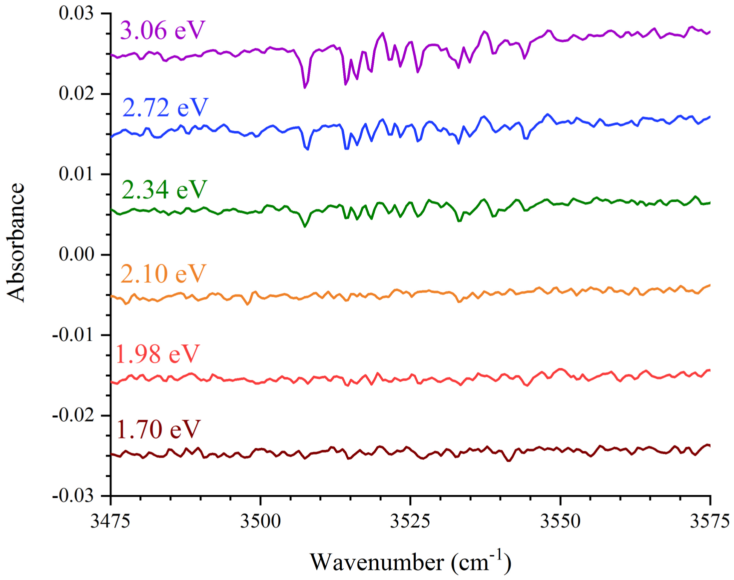

Figure 6.3. Low-temperature IR absorption spectra of $SrTiO_3$ from figure 6.1, focused on the O-H modes. The spectra have been distributed vertically for clarity.

A zoomed view of the O-H region from figure 6.1 is shown in figure 6.3. The O-H modes correspond well with those documented in Houde *et al.*[85] They begin appearing as dips in the spectrum at the same time as the broad absorption feature (upon exposure to the 2.34 eV LED). Dips in absorbance mean that these peaks are shrinking in the raw intensity spectra.

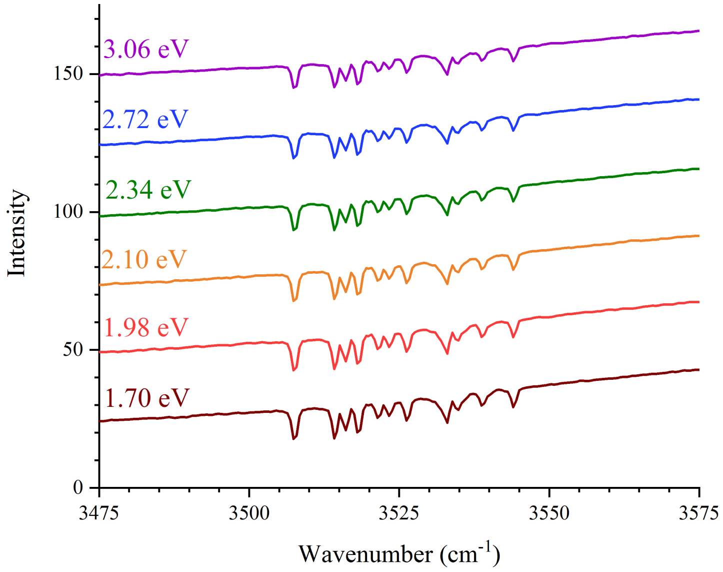

Figure 6.4. Low-temperature IR intensity spectra of $SrTiO_3$. These are the raw intensity spectra taken while the external LED was on. The changes are slight, but it can be seen that the peaks decrease in height beginning with exposure to the 2.34 eV LED.

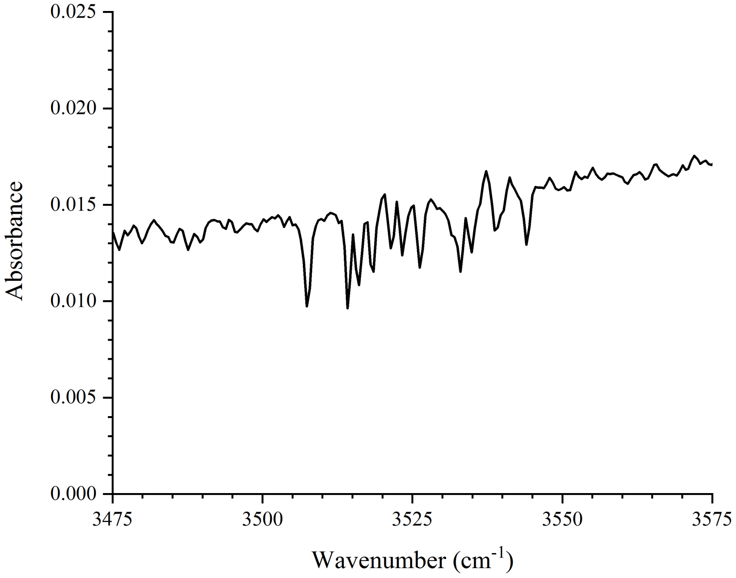

Figure 6.5. Low-temperature IR absorption spectrum of $SrTiO_3$. This spectrum was computed with 3.06 eV spectrum from figure 6.4 using the 1.70 eV spectrum as the reference.

Confirmation that the peaks shrink upon exposure to the 2.34 eV LED can be seen in the raw intensity spectra (figure 6.4) and comparing the 1.70 and 3.06 eV spectra directly (figure 6.5). In figure 6.4, the peaks beginning with the 2.34 eV LED exposure are slightly smaller than those in the spectra collected earlier. A more direct comparison can be made by computing an absorbance using the spectrum collected during 3.06 eV LED exposure with the 1.70 eV spectrum as the reference (figure 6.5). Since the O-H modes are visible as dips in this plot, that means they are reduced when exposed to light from the 3.06 eV LED.

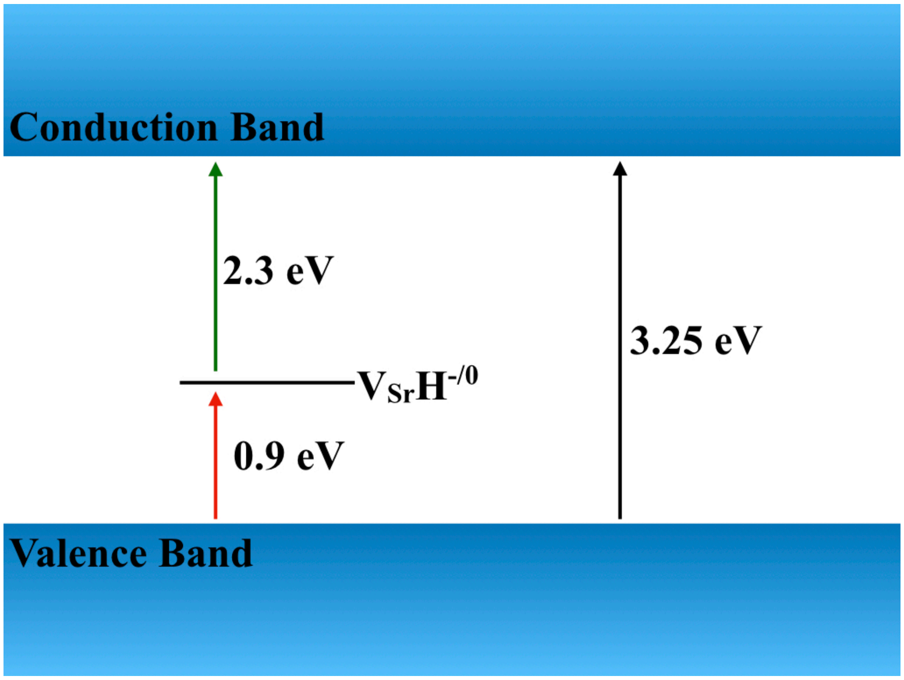

Figure 6.6. Proposed model for the process observed in figure 6.1.

In order to explain the behavior observed, the model in figure 6.6 is proposed. The $V_{Sr}H^{-/0}$ defect level is located ~2.3 eV below the conduction band minimum. When light of sufficient energy (2.3 eV and greater) impinges on the sample, an electron is excited from $V_{Sr}H^{-}$ to the conduction band, creating $V_{Sr}H^{0}$. With a free state available, infrared light with energy ~0.9 eV can excite a new electron from the valence band to form $V_{Sr}H^{-}$ again, allowing the process to repeat. When the supply of electrons eligible to occupy the $V_{Sr}H^{0}$ defect is exhausted, it ceases to become visible in the IR due to the now neutral H atom. This is consistent with the appearance of the broad absorption (corresponding to infrared light of ~0.9 eV) upon exposure to light of energy 2.3 eV and the reduction in intensity of the O-H modes. In STO, there is no barrier to the system relaxing to its ground state, so no persistence was observed once the LEDs were turned off.

6.2: Low-temperature light exposure of $BaTiO_3$

The experiment from section 6.1 was repeated using $BaTiO_3$. Single crystal samples were obtained from MTI. The samples were 10×10×0.5 mm, (100) oriented with 1 side polished, and had multiple visible ferroelectric domains. The experimental apparatus and procedure were identical, save for the addition of an LED with an above-gap photon energy (3.31 eV, 375 nm).

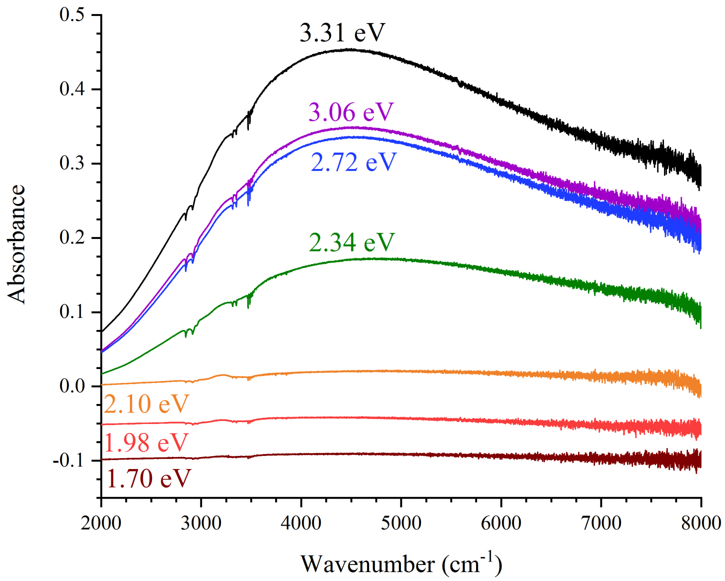

Figure 6.7. Low-temperature IR absorption spectrum of $BaTiO_3$ exposed to LEDs with the listed energies. The reference for each spectrum was the first spectrum taken in the dark, prior to any light exposure. The 1.70 and 1.98 eV spectra were shifted vertically downward for clarity.

Again, beginning with light exposure from the 2.34 eV LED, a broad absorption feature appears (figure 6.7). This time the broad absorption has a peak visible at ~4500 cm^{-1}. O-H modes, similar to those observed in section 6.1, are visible near 3500 cm^{-1} as well. The spectra in figure 6.7 were computed using the first spectrum taken in the dark, prior to any light exposure because this material shows some persistence.

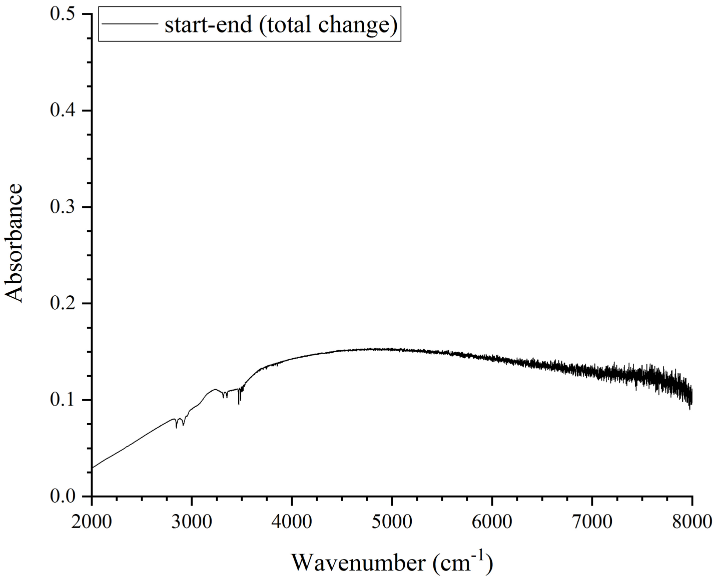

Figure 6.8. Low-temperature IR absorption spectrum of $BaTiO_3$. This spectrum was computed using the final spectrum taken in the dark (after exposure to the 3.31 eV LED) and the first spectrum (prior to any light exposure) as the reference. The broad absorption and O-H modes are still visible.

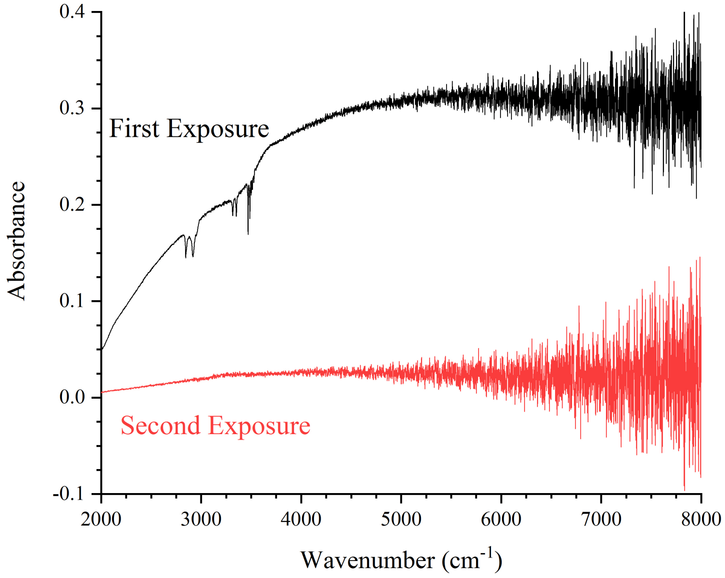

Figure 6.9. Low-temperature IR absorbance spectra of $BaTiO_3$ exposed to the 3.06 eV LED twice. Due to the persistence of the effect, the second exposure does not induce as much change as the first.

Persistence was checked using the first and last spectra collected (both with the LED off). The first spectrum, taken prior to any light exposure, was used as the reference. The result is shown in figure 6.8. The full height of the broad absorbance did not remain in this particular experiment, but it is definitely still present, along with the O-H modes visible at ~3500 cm^{-1}. In addition, an experiment was performed where the sample was exposed to the 3.06 eV LED two times sequentially. The pattern for spectrum collection was:

dark (1) – 3.06 eV LED on – dark (2) – 3.06 on – dark (3)

The spectra shown in figure 6.9 were calculated using the first and second dark spectra (black) and the second and third dark spectra (red). The changes over the course of the second exposure were less drastic than the first, indicating that the process had nearly saturated during the first exposure.

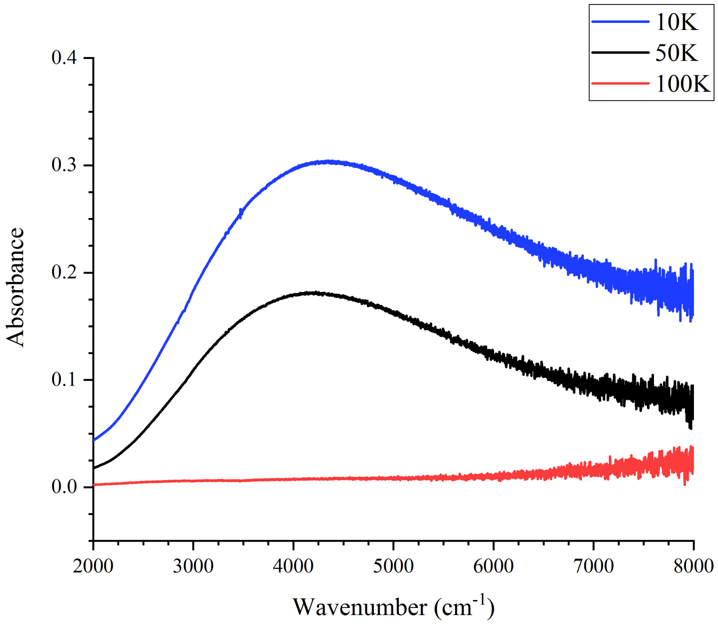

Figure 6.10. Low-temperature IR absorption spectra of $BaTiO_3$ taken as a series of increasing temperatures. The absorption spectra were computed using intensity spectra collected before and after exposure to light from the 3.31 eV LED (with the spectrum prior to light exposure as the references).

The temperature dependence of the persistence was checked by repeating an exposure experiment at 10, 50, and 100 K (figure 6.10). Spectra were taken before and after exposure to the 375 nm LED, and absorbances calculated using the spectrum collected prior to exposure as the reference. The broad absorbance peak was weakened when the measurement was performed at 50 K, and absent when performed at 100 K.

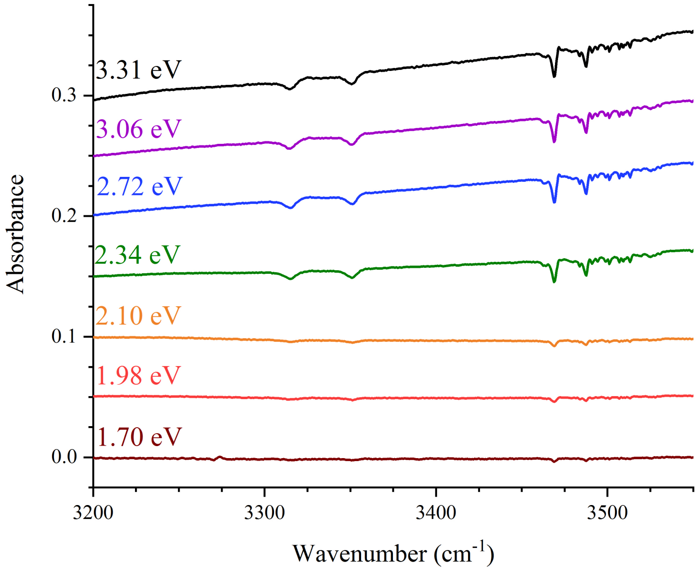

Figure 6.11. Low-temperature IR absorption spectrum of $BaTiO_3$ from figure 6.7, focused on the O-H modes. The spectra have been distributed vertically for clarity.

The behavior of the O-H modes matches that observed in STO. In the absorbance spectra, they begin appearing as dips at the same time as the broad absorption feature appears. In addition, two peaks at ~3320 and ~3350 cm^{-1} are visible. These resemble the H_{II} peaks observed in STO by Tarun and McCluskey.[86] Due to their presence alongside the persistent effects observed here indicates these peaks may correspond to the defects involved in the persistence of the broad absorption feature.

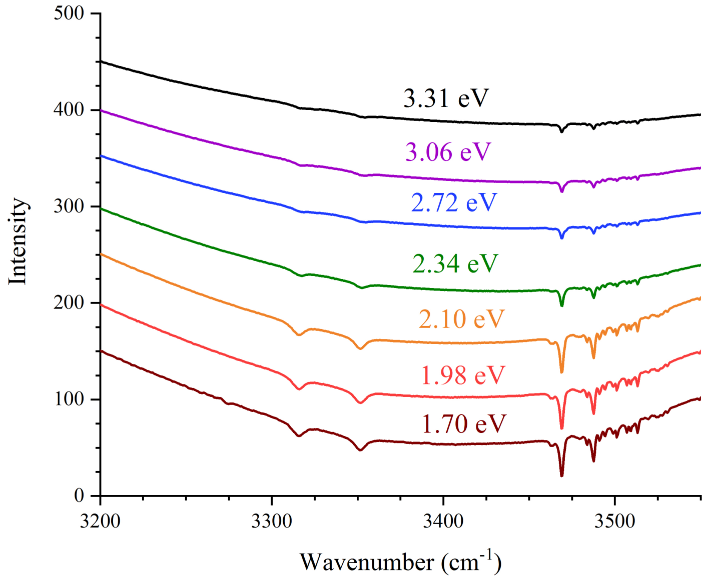

Figure 6.12. Low-temperature IR intensity spectra of $BaTiO_3$. These are the raw intensity spectra taken while the external LED was on. The changes are more noticeable than in they were in figure 6.4. The O-H modes are nearly gone when the 3.31 eV LED is used. The decrease in peak heights begins with the use of the 2.34 eV LED.

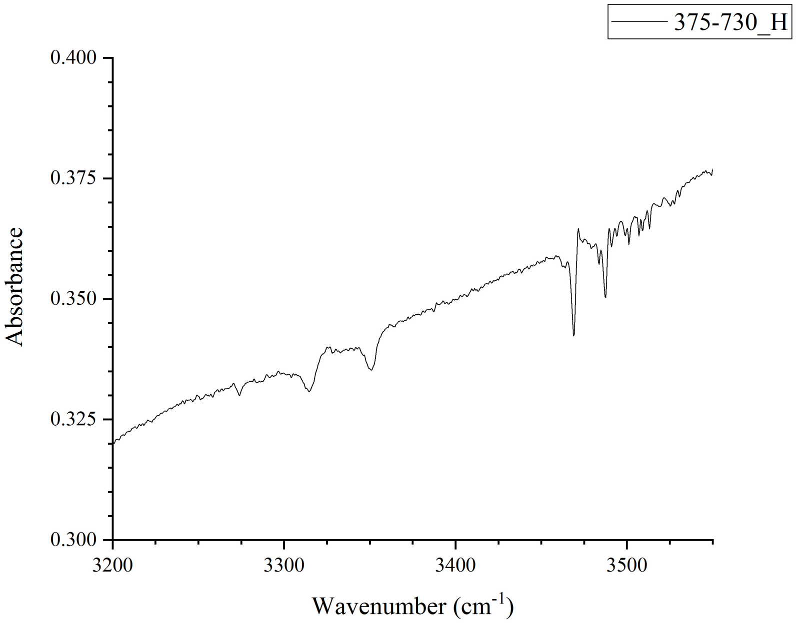

Figure 6.13. Low-temperature IR absorption spectrum of $BaTiO_3$. This spectrum was computed with the 3.31 eV spectrum from figure 6.12 using the 1.70 eV spectrum as the reference.

Behavior of the O-H modes in BTO is identical to that observed in STO, but more pronounced. The O-H modes begin decreasing in intensity upon exposure to light from the 2.34 eV LED, and are nearly gone following exposure to light from the 3.31 eV LED. The BTO sample also boasts two new peaks at ~3320 and ~3350 cm^{-1}, which correspond to the H_{II} peaks observed in Tarun and McCluskey.[86]

6.3: Conclusions

Interesting low-temperature absorptions were observed in as-received STO and BTO. Behavior of the two materials was similar, with broad absorption features appearing upon exposure to light from a 2.34 eV LED. In the case of STO, the peak of the absorption feature was not observed since the broad absorption occurred at large wavenumbers. The peak of the broad absorption in BTO was observed at ~4500 cm^{-1}. In both cases, appearance of the broad absorption corresponded with a reduction in intensity of the O-H stretching modes located near 3500 cm^{-1}. For STO, a two-photon process was proposed to model this behavior. A similar mechanism is likely at work in BTO. The presence of the H_{II} peaks alongside the persistent effects observed in BTO (and their corresponding absence in STO) indicates the two are likely related.

APPENDIX A: FLOWING GAS ANNEAL OF TiO_2

A1: Introduction

This appendix contains the results of a series of experiments performed on titanium dioxide (TiO_2) annealed under flowing gas. Prior to the work performed on barium titanate, TiO_2 was investigated to test the functionality of the flowing-gas annealing system as well as a persistent photoconductivity candidate. Some persistence in changes in the O-H modes was observed, but the dramatic PPC present in strontium and barium titanate, was not observed. The following section, written by Violet Poole, presents results collected jointly by Violet and myself as I was being trained in the use of the lab equipment.

A2: Results

An as-received TiO_2 sample from MTI Corp. was annealed with the 2-line flowing gas set up.

One gas line had nominally 1% hydrogen and 99% argon gas was flowing at a rate of 2.0 sl/m while the other line had 6 scf/h pure argon bubbling through water. The humidity sensor of the combined gas flow read 50% relative humidity at a temperature of 21°C. The system was purged for 30 minutes prior to heating.

The furnace heated up at a rate of 600°C per hour to 1000°C. Sample was annealed at 1000°C for 1 hour, at which time the tube in the furnace was shifted so sample was no longer inside. The sample turned dark during the rapid cool down (less than 5 minutes) in the flowing gas. The sample was cooled in the dark and exposed to 475 nm light, then high resolution ($0.5\ cm^{-1}$) IR spectra were taken. Pressed indium contacts show a resistance of about 100 Ω.

The LED was high powered and mounted to a printed circuit board and focused with a lens through the window of the cryostat. Note that the sample was angled to approximately 40 degrees from perpendicular to the IR beam. That way light from outside (90 degrees from IR path) could be directed on the sample during exposure. Unless otherwise noted, spectra were collected at low temperature (~10 K).

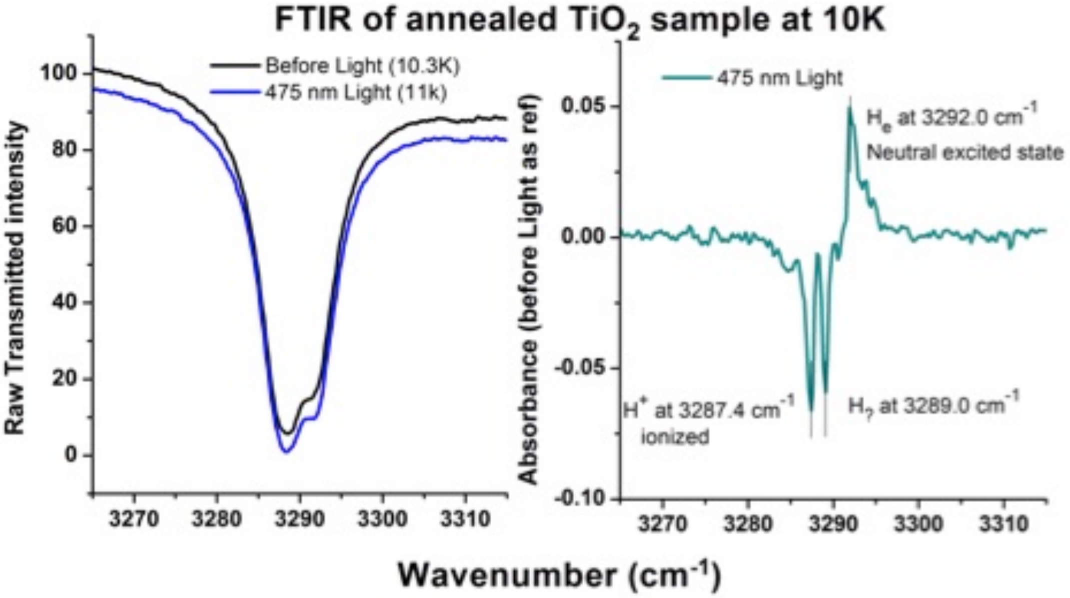

Figure A1. IR intensity (left) and absorption (right) spectra of flowing gas annealed, 475 nm light-exposed, TiO_2.

If we try to stabilize the temperature at 12 K before and during light exposure we get raw spectra that look like:

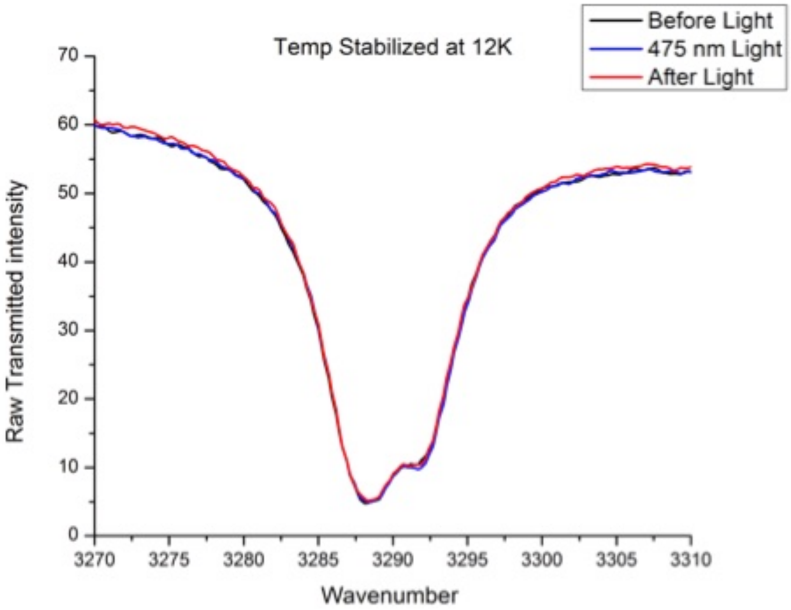

Figure A2. Temperature-stabilized IR intensity spectra of flowing gas annealed, light-exposed, TiO_2.

If we look at the absorbance of the sample with 475 nm light on, using the spectrum taken before light exposure as a reference we see:

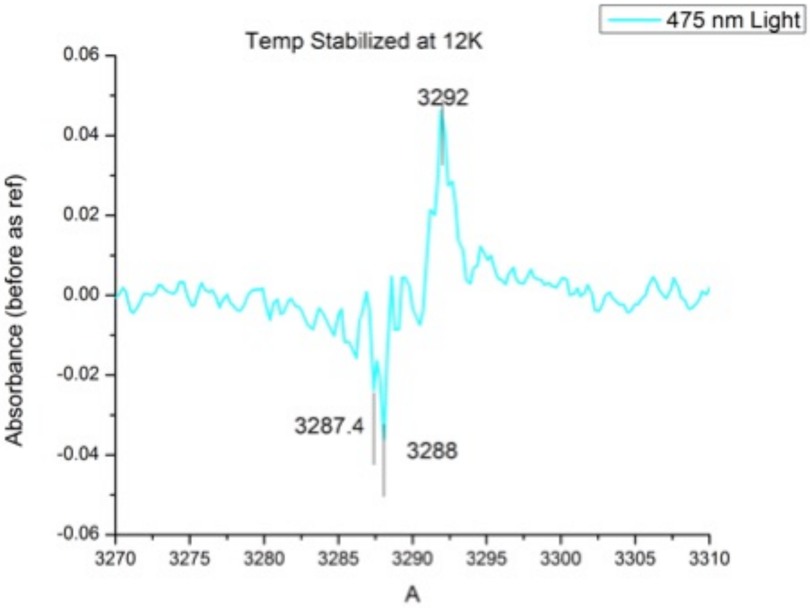

Figure A3. Temperature-stabilized IR absorption spectrum of flowing gas annealed, light-exposed, TiO_2.

The change in absorbance from after light with before light taken as a reference is noticeable. This indicates that the changes induced by light exposure have a persistent component.

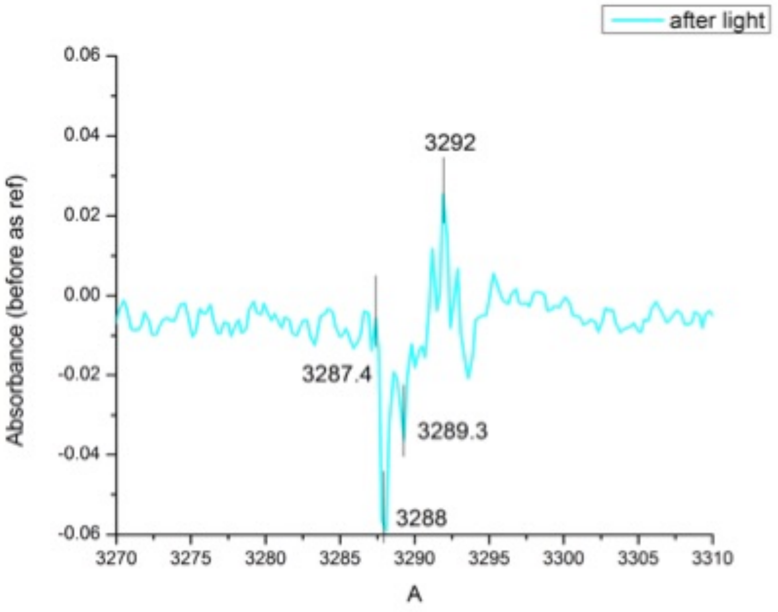

Figure A4. Temperature-stabilized IR absorption spectrum of flowing gas annealed, light-exposed, TiO_2. This absorbance was calculated using a spectrum taken after the external LED was turned off.

If we repeat the light exposure test with near band gap illumination (425 nm) we see:

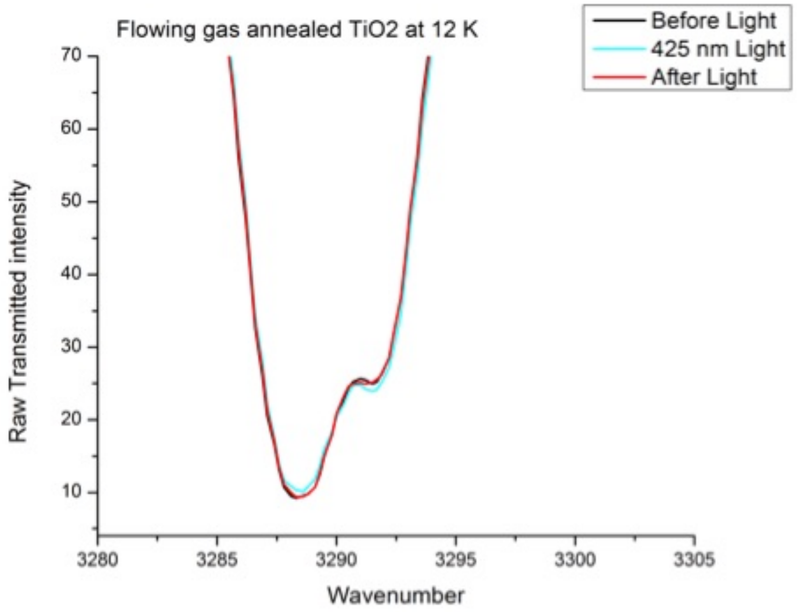

Figure A5. IR intensity spectra of flowing gas annealed, light-exposed, TiO_2. These spectra were collected using a higher-energy LED (425 nm).

The absorbance with before light as a background looks like:

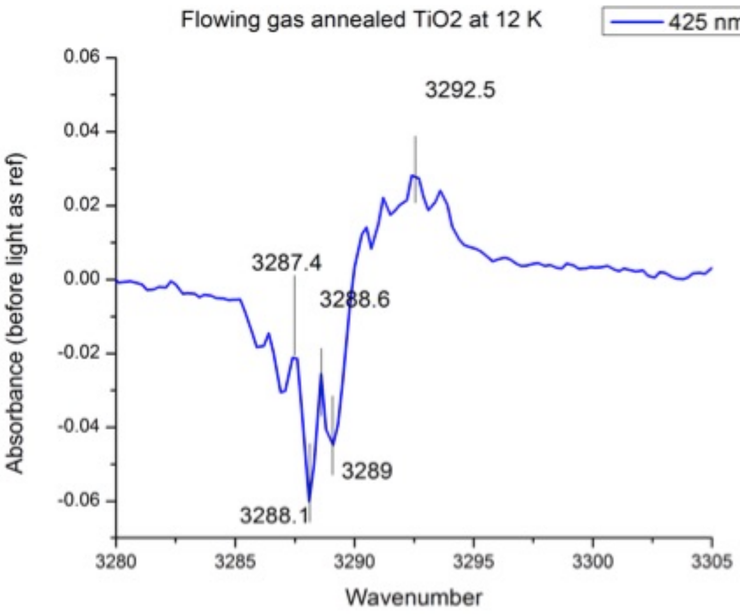

Figure A6. IR absorption spectrum calculated using the "before" and "425" spectra from figure A5.

The difference between before light exposure and after light exposure is still there:

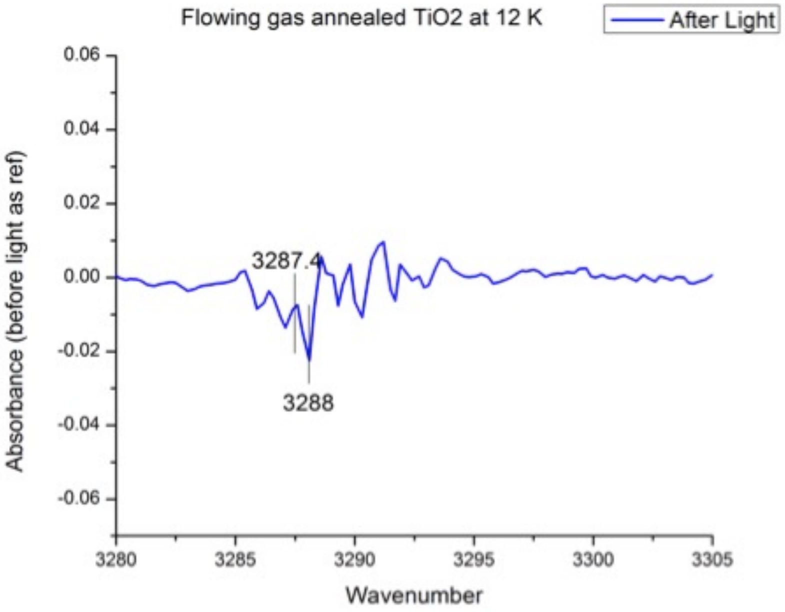

Figure A7. IR absorption spectrum calculated using the "before" and "after" spectra from figure A5. The peaks persist after the LED is turned off.

This behavior is markedly different from an as received TiO_2 (here the spectrum is taken with 1 cm^{-1} resolution):

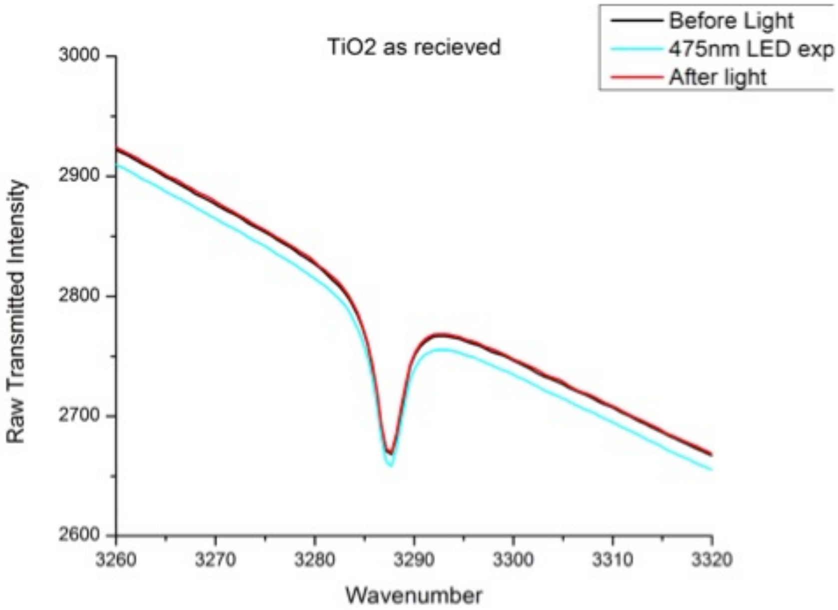

Figure A8. IR intensity spectra of as-received, light-exposed, TiO_2.

The absorbance of the as-received sample during light exposure, with before light as the reference, is very flat, indicating no change with light exposure:

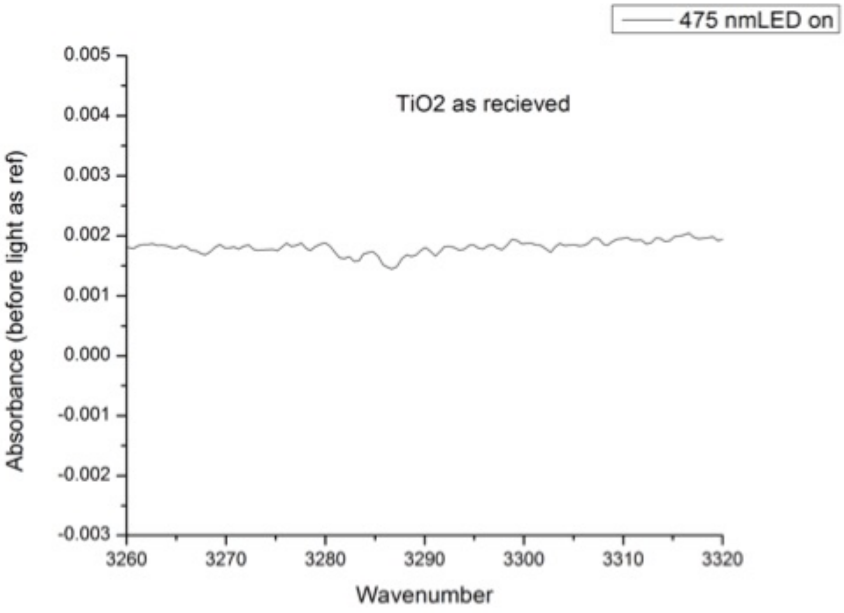

Figure A9. IR absorption spectrum calculated using the “before” and “475” spectra from figure A8.

TiO_2 annealed in a sealed evacuated ampoule with 0.5 atm of hydrogen gas at 500ºC for 2 hours has different behavior for the hydrogen peaks as well:

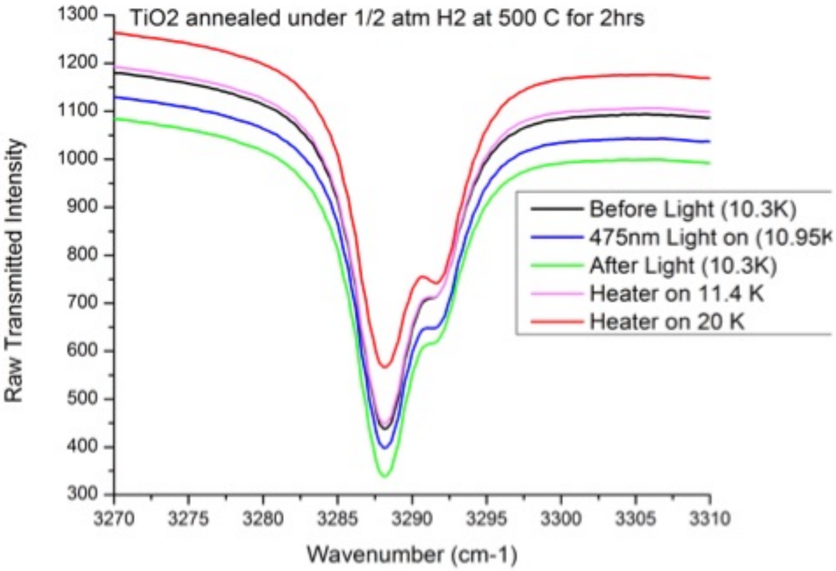

Figure A10. IR intensity spectra of TiO_2 annealed under a hydrogen environment in a sealed ampoule.

The absorbance of light exposure with before light as a reference. Note that a small amount of temperature change is occurring, which affects the populations of the various hydrogen lines:

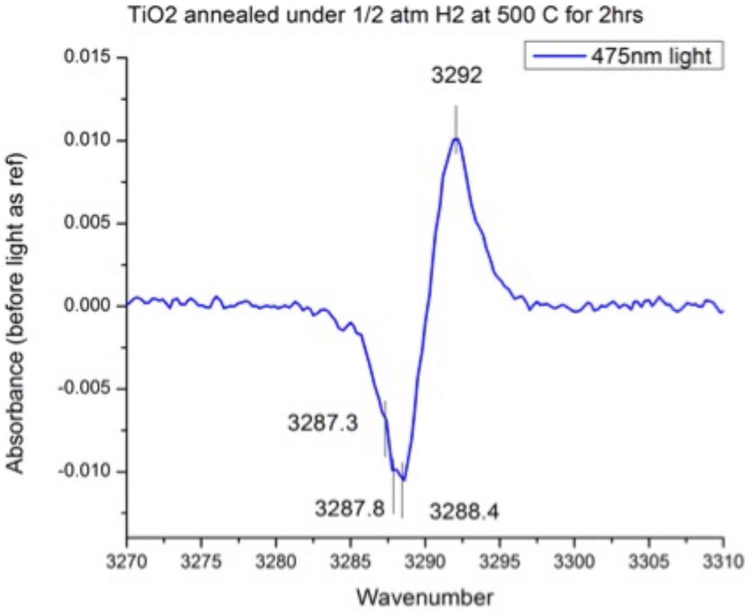

Figure A11. IR absorption spectrum calculated using the "before" and "475" spectra from figure A10.

We can remove the temperature effect on the H_2 annealed sample by looking at the absorbance of the light exposed sample using the 11 K spectra as a reference. Here the change is much less dramatic, but still present:

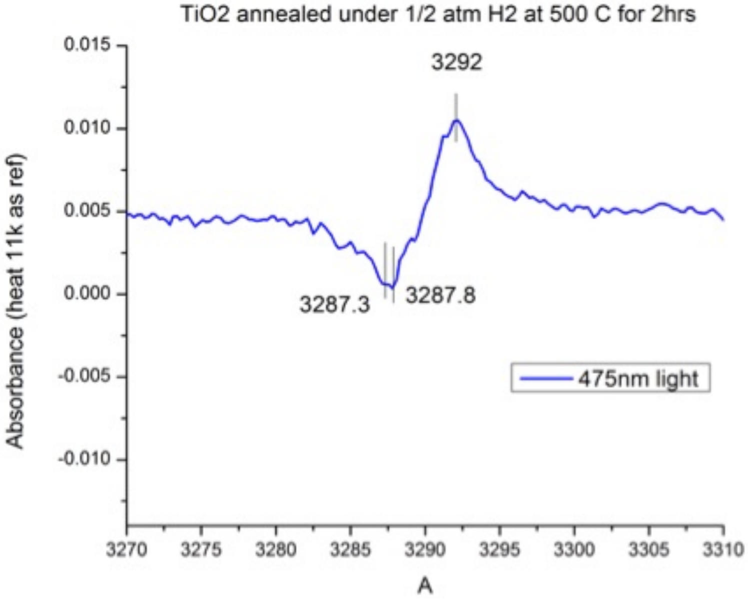

Figure A12. IR absorption spectrum calculated using the “475” and “11 K” spectra fron figure A10.

Measurements were made on the temperature dependence of the peaks. The spectrum was taken with a resolution of 1 cm^{-1}. However, settings on the IR resulted in an uncontrolled horizontal shifting of exact wavenumber placement from scan to scan. As a result, the shifting absorbances calculated from the raw spectra are not useful. Therefore only the raw spectra is shown:

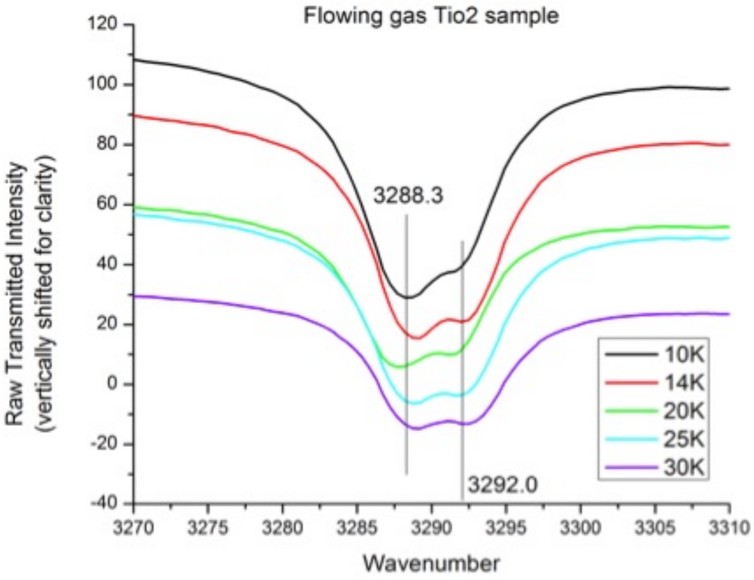

Figure A13. IR intensity spectra of TiO_2 annealed under a hydrogen environment in a sealed ampoule, taken at the listed temperatures.

APPENDIX B: HALL CHAMBER CONSTRUCTION

B1: Introduction

The Hall effect apparatus in the McCluskey lab is capable of performing measurements over a wide range of temperatures (~80-730 K) according to the manufacturer. It achieves elevated temperatures (>295 K) by simply using a heater and low temperatures (~80-295 K) by Joule-Thompson cooling. The sample stage is mounted on a "refrigerator" made of etched silica. The etchings are a series of gas capillaries that gas from a high-pressure (6000 psi) high-purity nitrogen cylinder expands into, cooling the sample state as it does, approximately according to the ideal gas law.

This type of cooling design has the advantage of being very compact and efficient. The disadvantages though, are that the refrigerators are relatively delicate, and not easy to replace. The refrigerator is also somewhat temperamental. The gas source needs to be pure and dry to prevent the capillaries from clogging. The refrigerator and the surface it adheres to need to be clean and aligned correctly, and a series of o-rings needs to be properly seated and lubricated. If left unattended for too long, the system has to be carefully purged to prevent the capillaries from clogging. If the capillaries clog, the best case is that the refrigerator ceases functioning. The worst case is that the 6000 psi gas from the cylinder makes it a small bomb (that is contained in the sample chamber and small, no one should be injured in the worst case).

In order to remove our dependence on the Joule-Thompson refrigerators, I attempted to manufacture a new sample chamber for our Hall effect instrument that used liquid nitrogen as a refrigerant, rather than high-pressure gas.

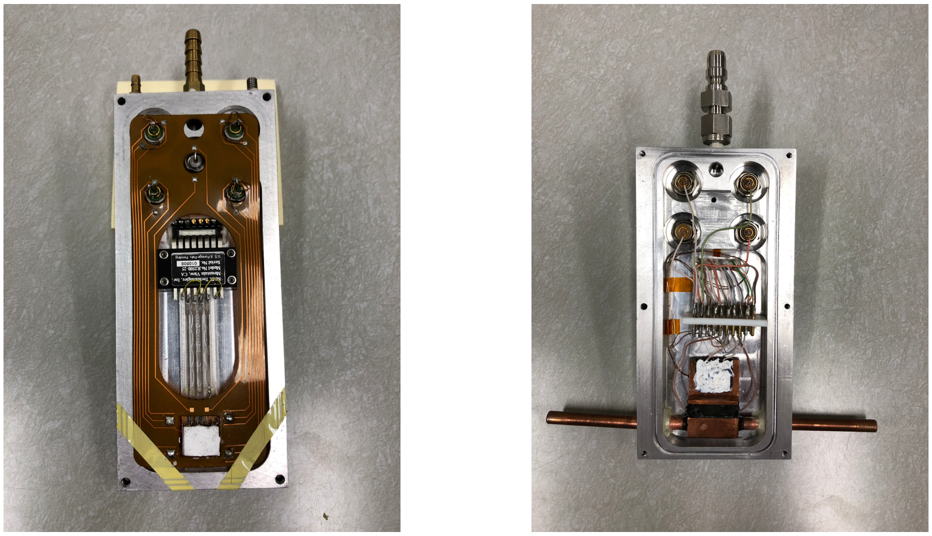

Figure B1. The Hall sample chamber provided by the manufacturer (left) and constructed by me (right).

The result of the construction is shown in the right of figure B1. I was successful insofar as the chamber is compatible with the system, and it does accept liquid nitrogen for cooling. Its cooling power was limited though, the lowest temperature achieved was ~220 K. This was done by using an INSTEC pump and attempting to draw liquid nitrogen from a dewar. Something about the way this was arranged didn't work very well, as the nitrogen boiled in the tubes under the negative pressure, losing most of its cooling power in the phase change. I had the idea of using a simple gravity-fed system instead (with the added bonus of not using electricity to pump), but was never able to formulate a way to do that effectively.

Regardless, should another student wants to try to make this chamber work, or iterate on my design in the future, a parts list for the critical components that the chamber needs to interface with the electronics system is included below as well as my notes regarding what I learned while making the body of the new chamber:

B2: Parts list

RTD:

This is a platinum resistance temperature detector, it is what the system uses to measure the temperature of the sample stage.

Omega number: F2010-100-B-100

Heraeus number: M222

Heater:

The requirement is a 100 Ω, 10 W resistor. I used an AlN thick film resistor.

AVX number: RP42010R0100GTTR

Mouser number: 581-RP42010R0100GTTR

Triax BNC feedthroughs:

Pomona number: 4388

Digikey number: 501-1871-ND

20-pin ribbon cable socket:

3M number: N2520-6002-RB

Digikey number: MHC20K-ND

O-rings for my version of the chamber are standard size 1/16”-048. In a pinch, Tech Services usually has a few made of Buna-N, but VITON is better for low temperature use.

B3: Machining notes

Final chamber size is 6”x3”. Obtain aluminum of the appropriate thickness from Tech Services, make sure to request stock at least 0.25” to 0.50” longer and wider than necessary, as the pieces will have to be faced. The larger pieces also make the first (and hardest) step of cutting the wells slightly easier, since the positioning of the wells matters less in this case.

1. Cut large wells. Plan to spend several hours on the well in the main body.
2. Cut chamber to size around the wells.
3. Cut BNC throughputs in the main body using the 3/4” and 3/8” end mills. Traditionally, it is bad practice to swap end mills and assume the readouts don’t need to be adjusted, however there is enough extra room in the 3/4” recesses that the approx. 0.010” the table drifts under the quill doesn’t impact the BNC fit.
4. After both the lid and main body have been cut to size in the x- and y-directions, place both in the mill vise (align in the x-direction with a C-clamp if necessary) and use the jacob’s chuck attachment to turn the mill into a very precise drill press. This set-up is the easiest way to place the holes for the clamping screws. The mill is much more powerful and has much less “wobble” than the student shop’s drill press. Cut slowly and use lots of fluid, it’s easy to break drill bits during this step.

5. Make sure to leave plenty (~0.100”) of extra space in the chamber thickness, Tech Services appreciates larger margins of error (step 9).

6. Tap the holes in the main body. The previous chambers used 4-40 Allen caps.

7. Cut the indents out of the exteriors of the body and lid. Countersink space for the clamping screws in the lid.

8. Cut the channel for the liquid N_2 pipe. Use a 1/4” end mill.

The above step is as far as the tools in the student shop can go. Tech Services will have to do the following finishing steps:

a. Mill the mating surfaces flat
b. Cut the O-ring channel
c. Cut the ribbon cable throughput

Finally,

Make the sample stage. 1/4” copper tube and a small copper block are needed. For the best seal between the tubes and block, thread the ends of the tube and tap the block. #1/4”-28 and similar will work. Tap the whole interior of the sample stage to increase surface area and therefore heat transfer. Due to the size of the components, the copper cannot be easily soldered together (either the curing process for embedding the components risks undoing the solder, or soldering after risks debonding the epoxy). Instead, use thermal epoxy on the threads and around the joints.

APPENDIX C: ABSORBANCE

C1: Introduction

I wanted to prepare the following brief notes regarding the behavior of absorbances for future students because some of these things were not immediately obvious to me. Remember that absorbance is defined in section 1.1.3 as:

$$Absorbance = \log_{10} \frac{I_0}{I} \tag{1.17}$$

In the following sections, the behavior of absorbance calculations will be shown using example functions. The "spectra" presented here are not real measurements. They were constructed for mathematical utility.

C2: Absorbance

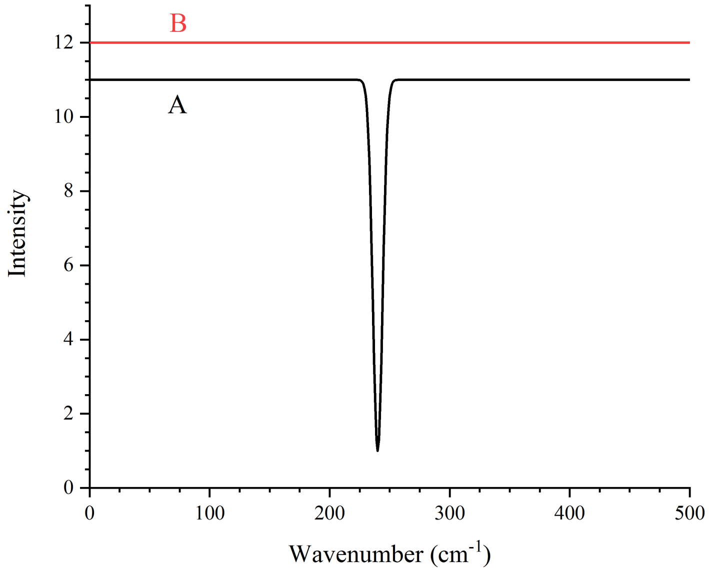

Figure C1. Example IR spectra. Spectrum A contains a Gaussian peak centered at 240 cm^{-1}. Spectrum B does not.

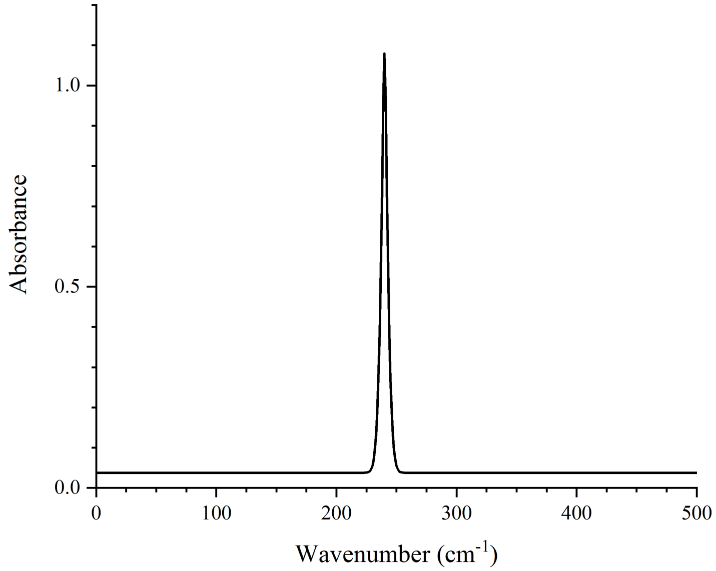

Figure C2. Absorbance spectrum calculated as $\log_{10}$(B/A) from figure C1.

Figures C1 and C2 show the simplest case of what occurs when an absorbance is calculated using a pair of spectra where one contains an IR peak and the other does not. Using I_0 = B and I = A, the absorbance result is shown in figure C2. The peak from spectrum A is still present, but has been flipped and now points upward.

Upward-pointing features indicate either the appearance of a new peak (as is the case in this example) or the strengthening of an existing peak. Downward pointing features indicate weakening (or the disappearance) of that peak.

C3: Multiplication of spectra

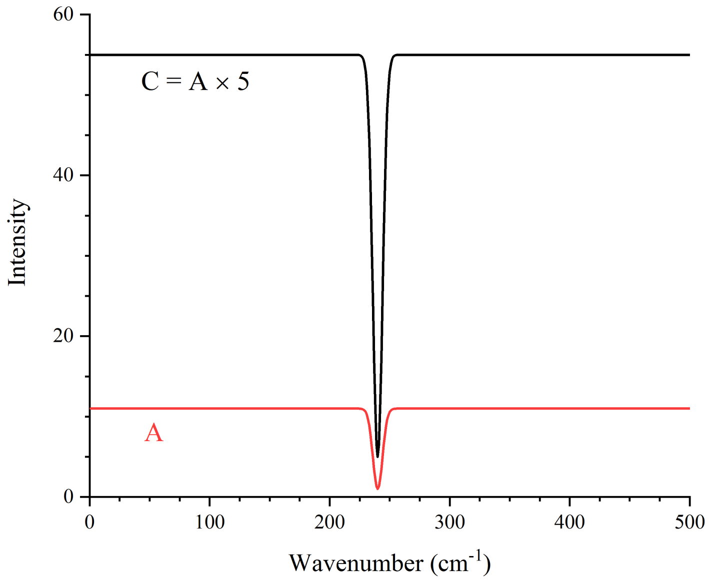

Figure C3. IR spectra with a Gaussian peak located at 240 cm^{-1}. Spectrum C is a simple multiplication of spectrum A.

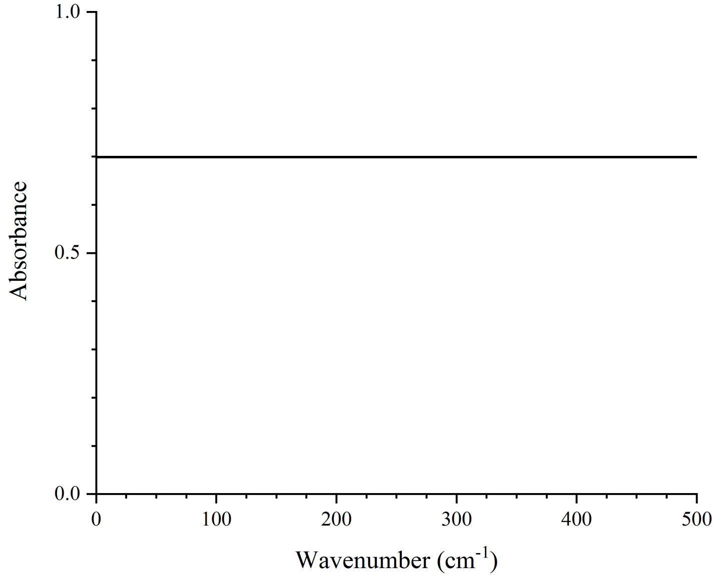

Figure C4. Absorbance spectrum calculated as $\log_{10}(C/A)$ from figure C3.

In the event that two spectra are mathematical multiples of each other, the absorbance result is a constant, as shown in figure C4.

C4: Peak shifting

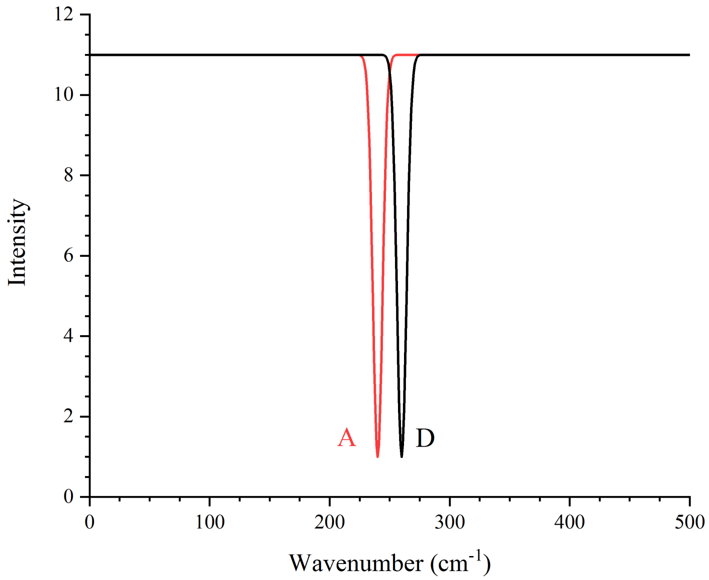

Figure C5. IR spectra with Gaussian peaks at 240 cm^{-1} (A) and 260 cm^{-1} (D).

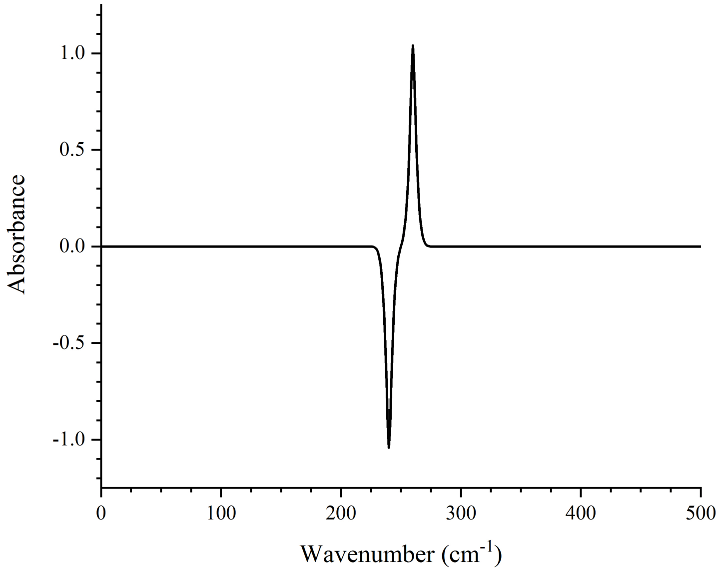

Figure C6. Absorbance spectrum calculated as $\log_{10}(A/D)$ from figure C5.

If a peak moves from one location to another, such as a situation like that shown in figure C5, the resulting absorbance calculation (figure C6) resembles the derivative of Dirac's delta function. Therefore this shape is referred to as a "derivative". This can appear if a peak moves from one place to another or if one peak grows and a near enough neighbor shrinks at the same time. The raw spectra must be examined closely to tell the difference between these two situations, but it should be obvious. A peak actively shifting is somewhat rare, whereas a pair of peaks with one growing and one shrinking will be obvious if an intermediate state where both exist simultaneously can be observed.

REFERENCES

[1] J. Bardeen and W.H. Brattain, Phys. Rev. **74**, 230 (1948).

[2] W. Shockley, PHYSICS TODAY 10 (1950).

[3] W. Schottky, Naturwissenschaften **26**, 843 (1938).

[4] Langenscheidt Editorial Staff, *Langenscheidt Pocket Dictionary German* (2011).

[5] H. Ibach and H. Lüth, *Solid-State Physics*, Fourth Edition (Springer, 2009).

[6] M.D. Popis, S.V. Popis, N. Oncel, M.R. Hoffmann, and D. Çakır, Journal of Applied Physics **123**, 074301 (2018).

[7] D. Nicholls, R.R. Li, B. Ware, C. Pansegrau, D. Çakir, M.R. Hoffmann, and N. Oncel, J. Phys. Chem. C **119**, 9845 (2015).

[8] P.E. Blöchl, Phys. Rev. B **50**, 17953 (1994).

[9] L.-W. Wang, Annu. Rev. Phys. Chem. **61**, 19 (2010).

[10] Y. Kang, H. Peelaers, K. Krishnaswamy, and C.G. Van de Walle, Appl. Phys. Lett. **112**, 062106 (2018).

[11] P.Y. Yu and M. Cardona, *Fundamentals of Semiconductors*, Fourth Edition (Springer, 2010).

[12] M.D. McCluskey and E.E. Haller, *Dopants and Defects in Semiconductors*, First Edition (CRC Press, 2012).

[13] M.D. McCluskey, Journal of Applied Physics **127**, 101101 (2020).

[14] M. Higashiwaki, K. Sasaki, A. Kuramata, T. Masui, and S. Yamakoshi, Phys. Status Solidi A **211**, 21 (2014).

[15] A.K. Saikumar, S.D. Nehate, and K.B. Sundaram, ECS J. Solid State Sci. Technol. **8**, Q3064 (2019).

[16] Y. Yao, S. Okur, L.A.M. Lyle, G.S. Tompa, T. Salagaj, N. Sbrockey, R.F. Davis, and L.M. Porter, Materials Research Letters **6**, 268 (2018).

[17] K. Sasaki, A. Kuramata, T. Masui, E.G. Víllora, K. Shimamura, and S. Yamakoshi, Appl. Phys. Express **5**, 035502 (2012).

[18] E.G. Víllora, K. Shimamura, K. Kitamura, and K. Aoki, Appl. Phys. Lett. **88**, 031105 (2006).

[19] Z. Galazka, K. Irmscher, R. Uecker, R. Bertram, M. Pietsch, A. Kwasniewski, M. Naumann, T. Schulz, R. Schewski, D. Klimm, and M. Bickermann, Journal of Crystal Growth **404**, 184 (2014).

[20] Z. Galazka, R. Uecker, D. Klimm, K. Irmscher, M. Naumann, M. Pietsch, A. Kwasniewski, R. Bertram, S. Ganschow, and M. Bickermann, ECS J. Solid State Sci. Technol. **6**, Q3007 (2017).

[21] H. Aida, K. Nishiguchi, H. Takeda, N. Aota, K. Sunakawa, and Y. Yaguchi, Jpn. J. Appl. Phys. **47**, 8506 (2008).

[22] E.G. Víllora, K. Shimamura, Y. Yoshikawa, K. Aoki, and N. Ichinose, Journal of Crystal Growth **270**, 420 (2004).

[23] J. Jesenovec, S.E. Karcher, J.B. Varley, and J.S. McCloy, In Press (2021).

[24] K. Irmscher, Z. Galazka, M. Pietsch, R. Uecker, and R. Fornari, Journal of Applied Physics **110**, 063720 (2011).

[25] A. Kyrtsos, M. Matsubara, and E. Bellotti, Appl. Phys. Lett. **112**, 032108 (2018).

[26] J.B. Varley, A. Janotti, C. Franchini, and C.G. Van de Walle, Phys. Rev. B **85**, 081109 (2012).

[27] Y.K. Frodason, K.M. Johansen, L. Vines, and J.B. Varley, Journal of Applied Physics **127**, 075701 (2020).

[28] M.E. Ingebrigtsen, J.B. Varley, A.Yu. Kuznetsov, B.G. Svensson, G. Alfieri, A. Mihaila, U. Badstübner, and L. Vines, Appl. Phys. Lett. **112**, 042104 (2018).

[29] J.R. Ritter, J. Huso, P.T. Dickens, J.B. Varley, K.G. Lynn, and M.D. McCluskey, Appl. Phys. Lett. **113**, 052101 (2018).

[30] C. Pansegrau, J. Jesenovec, J.S. McCloy, and M.D. McCluskey, Appl. Phys. Lett. **119**, 102104 (2021).

[31] J.R. Ritter, K.G. Lynn, and M.D. McCluskey, Journal of Applied Physics **126**, 225705 (2019).

[32] M. Saleh, Semiconductor Science and Technology **35**, (2020).

[33] M. Saleh, A. Bhattacharyya, J.B. Varley, S. Swain, J. Jesenovec, S. Krishnamoorthy, and K. Lynn, Appl. Phys. Express **12**, 085502 (2019).

[34] A. Kuramata, K. Koshi, S. Watanabe, Y. Yamaoka, T. Masui, and S. Yamakoshi, Jpn. J. Appl. Phys. **55**, 1202A2 (2016).

[35] M.M. Vijatovic, J.D. Bobic, and B.D. Stojanovic, Sci Sintering **40**, 155 (2008).

[36] K. Suzuki and K. Kijima, Jpn. J. Appl. Phys. **44**, 2081 (2005).

[37] M.H. Garrett and I. Mnushkina, Journal of Crystal Growth **166**, 550 (1996).

[38] P. Duran, D. Gutierrez, J. Tartaj, and C. Moure, Ceramics International **28**, 283 (2002).

[39] T. Kolodiazhnyi, A. Petric, M. Niewczas, C. Bridges, A. Safa-Sefat, and J.E. Greedan, Phys. Rev. B **68**, 085205 (2003).

[40] M.C. Tarun, F.A. Selim, and M.D. McCluskey, Phys. Rev. Lett. **111**, 187403 (2013).

[41] E.D. Jeong, S.M. Yu, J.H. Yoon, J.S. Bae, C.R. Cho, K.T. Lim, P.H. Borse, and H.G. Kim, 6 (n.d.).

[42] A. Spinelli, M.A. Torija, C. Liu, C. Jan, and C. Leighton, Phys. Rev. B **81**, 155110 (2010).

[43] K.A. Müller and H. Burkard, Phys. Rev. B **19**, 3593 (1979).

[44] D.V. Lang and R.A. Logan, Phys. Rev. Lett. **39**, 635 (1977).

[45] V.M. Poole, J. Huso, and M.D. McCluskey, Journal of Applied Physics **123**, 161545 (2018).

[46] Y. Tomm, J.M. Ko, A. Yoshikawa, and T. Fukuda, Solar Energy Materials & Solar Cells **66**, 369 (2001).

[47] J. Jesenovec, M.H. Weber, C. Pansegrau, M.D. McCluskey, K.G. Lynn, and J.S. McCloy, Journal of Applied Physics **129**, 245701 (2021).

[48] J. Jesenovec, C. Pansegrau, M.D. McCluskey, J.S. McCloy, T.D. Gustafson, L.E. Halliburton, and J.B. Varley, Phys. Rev. Lett. **128**, 077402 (2022).

[49] J. Jesenovec, J. Varley, and S.E. Karcher, Journal of Applied Physics **129**, (2021).

[50] J. Jesenovec, C. Remple, J. Huso, B. Dutton, P. Toews, M.D. McCluskey, and J.S. McCloy, Journal of Crystal Growth **578**, (2022).

[51] P. Weiser, M. Stavola, W.B. Fowler, Y. Qin, and S. Pearton, Appl. Phys. Lett. **112**, 232104 (2018).

[52] M.D. McCluskey, S.J. Jokela, K.K. Zhuravlev, P.J. Simpson, and K.G. Lynn, Applied Physics Letters **81**, 3807 (2002).

[53] P. Deák, Q. Duy Ho, F. Seemann, B. Aradi, M. Lorke, and T. Frauenheim, Phys. Rev. B **95**, 075208 (2017).

[54] H. Peelaers, J.L. Lyons, J.B. Varley, and C.G. Van de Walle, APL Materials **7**, 022519 (2019).

[55] B. Pajot and C. Song, Phys. Rev. B **45**, 6484 (1992).

[56] O.F. Schirmer, A. Forster, H. Hesse, M. Wohlecke, and S. Kapphan, J. Phys. C: Solid State Phys. **17**, 1321 (1984).

[57] B. Andlauer, J. Schneider, and W. Tolksdorf, Phys. Status Solidi B **73**, 533 (1976).

[58] C.A. Lenyk, N.C. Giles, E.M. Scherrer, B.E. Kananen, L.E. Halliburton, K.T. Stevens, G.K. Foundos, J.D. Blevins, D.L. Dorsey, and S. Mou, Journal of Applied Physics **125**, 045703 (2019).

[59] B.E. Kananen, L.E. Halliburton, E.M. Scherrer, K.T. Stevens, G.K. Foundos, K.B. Chang, and N.C. Giles, Appl. Phys. Lett. **111**, 072102 (2017).

[60] T.D. Gustafson, J. Jesenovec, C.A. Lenyk, N.C. Giles, J.S. McCloy, M.D. McCluskey, and L.E. Halliburton, Journal of Applied Physics **129**, 155701 (2021).

[61] W. Ulrici, M. Czupalla, and M. Seifert, Physica Status Solidi (b) **210**, 551 (1998).

[62] Y. Qin, M. Stavola, W.B. Fowler, P. Weiser, and S.J. Pearton, ECS J. Solid State Sci. Technol. **8**, Q3103 (2019).

[63] T. Onuma, S. Fujioka, T. Yamaguchi, M. Higashiwaki, K. Sasaki, T. Masui, and T. Honda, Appl. Phys. Lett. **103**, 041910 (2013).

[64] T.D. Gustafson, N.C. Giles, and B.C. Holloway, Journal of Applied Physics 15 (2022).

[65] V.M. Poole, J. Dashdorj, M.E. Zvanut, and M.D. McCluskey, MRS Online Proc. Libr. **1792**, 706 (2015).

[66] V.M. Poole, S.J. Jokela, and M.D. McCluskey, Sci Rep **7**, 6659 (2017).

[67] L. Hesselink, S.S. Orlov, and M.C. Bashaw, Proc. IEEE **92**, 1231 (2004).

[68] J.H. Hong, Opt. Eng **34**, 2193 (1995).

[69] V.M. Poole, J. Huso, and M.D. McCluskey, Journal of Applied Physics **123**, 161545 (2018).

[70] Z. Zhang and A. Janotti, Phys. Rev. Lett. **125**, 126404 (2020).

[71] C. Linderalv, A. Lindman, and P. Erhart, 11 (n.d.).

[72] M.V. Raymond and D.M. Smyth, Journal of Physics and Chemistry of Solids **57**, 1507 (1996).

[73] J.T. Last, Phys. Rev. **105**, 1740 (1957).

[74] C.N. Berglund and H.J. Braun, Phys. Rev. **164**, 790 (1967).

[75] C.N. Berglund and W.S. Baer, Phys. Rev. **157**, 358 (1967).

[76] H. Ikushima and S. Hayakawa, Japanese Journal of Applied Physics **6**, 454 (1967).

[77] H. Ihrig, J. Phys. C: Solid State Phys. **9**, 3469 (1976).

[78] H. Ihrig and D. Hennings, Phys. Rev. B **17**, 4593 (1978).

[79] J.P. Boyeaux and F.M. Michel-Calendini, J. Phys. C: Solid State Phys. **12**, 545 (1979).

[80] J.F. Scott, S.A.T. Redfern, M. Zhang, and M. Dawber, Journal of the European Ceramic Society 4 (2001).

[81] Y. Iwazaki, K. Morito, T. Suzuki, H. Kishi, and S. Tsuneyuki, Ferroelectrics **355**, 108 (2007).

[82] Y. Iwazaki, S. Toshimasa, and S. Tsuneyuki, Journal of Applied Physics **108**, 083705 (2010).

[83] S. Kapphan, Ferroelectrics **37**, 673 (1981).

[84] V.M. Poole, C.D. Corolewski, and M.D. McCluskey, AIP Advances **5**, 127217 (2015).

[85] D. Houde, Y. Lépine, C. Pépin, S. Jandl, and J.L. Brebner, Phys. Rev. B **35**, 4948 (1987).

[86] M.C. Tarun and M.D. McCluskey, Journal of Applied Physics **109**, 063706 (2011).